

DEPENDENCE OF VIRIAL FACTORS ON OPTICAL SPECTRAL PROPERTIES OF ACTIVE GALACTIC NUCLEI

SEN YANG,^{1,2} PU DU,¹ AND JIAN-MIN WANG^{1,3,4}

¹Key Laboratory for Particle Astrophysics, Institute of High Energy Physics, Chinese Academy of Sciences, 19B Yuquan Road, Beijing 100049, People's Republic of China

²School of Physical Science, University of Chinese Academy of Sciences, 19A Yuquan Road, Beijing 100049, People's Republic of China

³National Astronomical Observatories of China, Chinese Academy of Sciences, 20A Datun Road, Beijing 100020, People's Republic of China

⁴School of Astronomy and Space Science, University of Chinese Academy of Sciences, 19A Yuquan Road, Beijing 100049, People's Republic of China

ABSTRACT

Reverberation mapping (RM) has long been a powerful tool for measuring the masses of supermassive black holes (SMBHs) at the centers of active galactic nuclei (AGNs), but the precision of these mass measurements depends on the so-called virial factors. It has been demonstrated that the virial factors exhibit significant diversity, spanning approximately 1-2 orders of magnitude across different AGNs. However, the underlying physical drivers for the diversity have not yet been finalized. Here, adopting the SMBH mass – spheroid luminosity relations of inactive galaxies with different bulge classifications, we calibrate the virial factors corresponding to the AGNs with pseudobulges (PB) and classical bulges (or elliptical hosts, CB) using the latest nearby RM sample. We investigate the correlations between virial factors and the AGN spectral properties, and find that for both PB and CB samples, the FWHM-based virial factors exhibit significant anti-correlations with the emission-line widths and profiles, while the σ_{line} -based virial factors only show moderate anti-correlations with line widths for PB. We attribute these correlations mainly to the inclination angle or opening angle of the broad-line regions. Moreover, we establish new relations to give more precise virial factors and, in combination with the latest iron-corrected radius-luminosity relation, develop tentatively new single-epoch estimators of SMBH masses, which enable more accurate measurements of SMBH masses in large AGN samples.

Keywords: Galaxies: Active Galactic Nuclei - Galaxies: nuclei - Galaxies: 2-d decomposition - Quasars: emission lines - Quasars: supermassive black holes

1. INTRODUCTION

Reverberation mapping (RM, e.g., Bahcall et al. 1972; Blandford & McKee 1982; Peterson 1993) is widely recognized as a powerful method for directly measuring the masses of supermassive black holes (SMBHs) located in the centers of active galactic nuclei (AGNs). Over the past 30 years, RM has been applied to over 200 AGNs, successfully determining the masses of their SMBHs (e.g., Kaspi et al. 2000; Bentz et al. 2009; Du et al. 2014; Hu et al. 2021; Bao et al. 2022; Yu et al. 2023; Shen et al. 2023). In RM campaigns, the sizes of broad-line regions (BLRs) in AGNs can be determined by measuring the variations of the continuum fluxes and the delayed responses of the broad emission lines (BELs) through long-term spectroscopic monitor-

ing. Combining with the velocity width (V) quantified by the FWHM or the dispersion (σ_{line}) of the emission-line profile, the BH mass can be obtained by

$$M_{\bullet} = f_{\text{BLR}} \frac{V^2 R_{\text{BLR}}}{G} \quad (1)$$

where $R_{\text{BLR}} = c\tau$ is the size of BLR, τ is the time delay of the emission line with respect to the varying continuum, c is the speed of light, G is the gravitational constant, and f_{BLR} is called “virial factor”. The factor f_{BLR} represents the unknown geometry and kinematics of the BLR, and directly determines the accuracy of mass measurements of SMBHs. The virial factor is different if using different velocity-width measurement (FWHM or σ_{line}) of the emission line. In addition, the velocity width of the emission line can be measured both from the mean and root-mean-square (rms) spectra in RM observations. Therefore, there are virial factors for four velocity combinations – f_{MF} , f_{MS} , f_{RF} , and f_{RS}

(corresponding to the cases of FWHM or σ_{line} from the mean or rms spectra). Here, “M” and “R” represent the mean and rms spectra, while “F” and “S” denote the FWHM and σ_{line} .

In addition to the mass measurements obtained from the RM observations, the values of virial factors have important implications for the single-epoch mass estimates of SMBHs in AGNs, particularly for those in the high-redshift universe during the era of the James Webb Space Telescope (JWST). Recently, many SMBHs in the high-redshift universe have been found to exhibit disproportionately large masses (relative to the dynamical masses of their host galaxies) compared to their local counterparts (e.g., Farina et al. 2022; Goulding et al. 2023; Harikane et al. 2023; Pacucci et al. 2023; Maiolino et al. 2024). However, there are also reports of SMBH masses to host galaxy mass ratios that are consistent with the local cases (e.g., Izumi et al. 2019, 2021; Ding et al. 2023). These discoveries are all based on single-epoch mass estimates, highlighting the importance of a better understanding of the virial factors.

From an observational perspective, there are currently two approaches to determine the values of virial factors. The first approach is to calibrate the virial factor using the masses measured by methods independent from RM. Commonly used are the relations between the masses of the central SMBHs and the properties (e.g., the stellar velocity dispersion σ_* , the luminosity L_{bul} , and the mass $M_{*,\text{bulge}}$) of the spheroids (bulges or ellipticals) of inactive galaxies (e.g., Onken et al. 2004; Park et al. 2012; Grier et al. 2013; Ho & Kim 2014; Woo et al. 2015; Yu et al. 2019). The underlying principle is based on the assumption that active galaxies and inactive galaxies have the same $M_{\bullet} - \sigma_*$, $M_{\bullet} - L_{\text{bul}}$, or $M_{\bullet} - M_{*,\text{bul}}$ relations. The average virial factor of an RM sample can be determined by comparing with the masses obtained by these relations. Although, due to the different RM samples used in the f_{BLR} calibrations and the evolving understanding on the M_{\bullet} -spheroid relations over time, the value of virial factor varies slightly across different studies. Specifically, the virial factors based on FWHM (from mean and rms spectra) are consistently around $1 \sim 1.5$, while those based on σ_{line} (from mean and rms spectra) are generally in the range of 4 to 5. The second approach is to obtain the virial factors by the dynamical modeling of BLRs, which yields the best model-dependent description of the BLR through fitting the RM data and gives the SMBH mass without assuming a virial factor (e.g., Pancoast et al. 2011, 2014; Grier et al. 2017; Li et al. 2018; Villafaña et al. 2023). Therefore, it can derive the virial factors for individual AGNs. Additionally, the BLR dynamical modeling based on single-epoch spectra can also constrain the virial factors by fitting emission-line profiles (Kuhn et al. 2024). Recently, the high-resolution interferometry provide a new approach to perform BLR dynamical modeling (e.g., Gravity Collaboration et al. 2018;

GRAVITY Collaboration et al. 2020, 2021; Abuter et al. 2024). The joint analysis of RM and interferometry can give even stronger constraint to the virial factors (e.g., Wang et al. 2020; Li et al. 2022). The average values of virial factors obtained from dynamical modeling are generally consistent with those derived from the former approach (e.g., Grier et al. 2017; Villafaña et al. 2023). However, the virial factors from both approaches exhibit wide range of values (see, e.g., Woo et al. 2015; Villafaña et al. 2023), implying that the virial factors of individual objects may be highly diverse because of their different BLR geometry and kinematics.

Exploring the relationship between the virial factors and the AGN/BLR properties is an approach to understanding the physical origins of the diversity and to establish methods for improving the accuracy of SMBH mass measurements. Collin et al. (2006) separated the sample from Onken et al. (2004) into two populations based on the $\text{FWHM}/\sigma_{\text{line}}$ of their $\text{H}\beta$ emission lines, and found that the virial factors are slightly smaller in the population with larger $\text{FWHM}/\sigma_{\text{line}}$ (see Figures 9 and 10 in Collin et al. 2006). They speculated that the strength of a disk-wind component of BLRs contributes to the difference of the two populations, and the inclination effects play some roles in the population with smaller $\text{FWHM}/\sigma_{\text{line}}$. When dividing the sample into barred and non-barred galaxies, Graham et al. (2011) found that the virial factors of barred galaxies are smaller than those of the non-barred galaxies based on the $M_{\bullet} - \sigma_*$ at that time. Pseudobulges (PB) are a category of bulges characterized by disk-like density profiles and kinematics, believed to arise from the secular evolution of galaxies, in contrast to the formation processes of classical bulges (CB). Considering that the $M_{\bullet} - \sigma_*$ relation of PB is different from that of CB and ellipticals, Ho & Kim (2014) evaluated the f_{BLR} factor by taking into account their bulge classifications, and found that the virial factors of PB are smaller by a factor of ~ 2 compared with the CB and ellipticals.

Recently, Mejía-Restrepo et al. (2018) derived SMBH masses by fitting the accretion disk spectra in 37 AGNs at $z \sim 1.5$ and obtained their virial factors. They claimed that the virial factors of $\text{H}\alpha$, $\text{H}\beta$, Mg II , and C IV lines show strong anti-correlations their FWHM. However, as their sample lacked RM observations, they estimated the BLR sizes of their sample by adopting the radius-luminosity ($R_{\text{H}\beta}$ - L_{5100}) relation (e.g., Kaspi et al. 2000; Bentz et al. 2013). Based on almost the same sample as Ho & Kim (2014), Yu et al. (2019) investigated the virial factors and found that f_{MF} and f_{RF} show anti-correlations with FWHM, σ_{line} , and $\text{FWHM}/\sigma_{\text{line}}$, whereas f_{MS} and f_{RS} display much weaker or no correlations. From dynamical modeling, Pancoast et al. (2014) found that the virial factors are correlated with inclination angles, but not with M_{\bullet} , L_{5100} , or $\text{FWHM}/\sigma_{\text{line}}$ of the emission-line profiles, where L_{5100} is the monochromatic luminosity at 5100\AA . However, Grier et al. (2017)

discovered that the virial factor is likely correlated with M_{\bullet} , inclination and opening angles of the BLR, but shows no correlation with L_{5100} . The latest compilation of dynamical modeling works (Villafaña et al. 2023) found evidence (marginal evidence) for a correlation between f_{MS} (f_{RS}) and M_{\bullet} , marginal evidence for an anti-correlation of BLR thickness (inclination angle) with f_{MF} and f_{RF} (f_{MF} , f_{RF} , and f_{RS}), and marginal evidence for a correlation between f_{RS} and $\text{FWHM}/\sigma_{\text{line}}$ from rms spectrum.

It is obvious that the dependency of virial factors on the BLR/AGN properties still remain controversial. Specifically, Collin et al. (2006), Mejía-Restrepo et al. (2018), and Yu et al. (2019) found that the virial factors show anti-correlations with FWHM , σ_{line} , or $\text{FWHM}/\sigma_{\text{line}}$, indicating that the AGNs with narrower BELs have larger virial factors. On the other hand, Graham et al. (2011) and Ho & Kim (2014) suggested that the virial factors of AGNs with bars and PB are relatively smaller. It has been known that narrow-line type 1 AGNs (narrow-line Seyfert 1 galaxies, NLS1s) are more likely hosted in barred and in PB galaxies, compared to broad-line counterparts (e.g., Orban de Xivry et al. 2011; Kim et al. 2017). Therefore, on the contrary, it implies that the AGNs with narrower BELs have smaller virial factors. In addition, Villafaña et al. (2023) discovered marginal evidence for a correlation between f_{RS} and $\text{FWHM}/\sigma_{\text{line}}$, further supporting this point. Therefore, it is crucial to clarify this “paradox” through the use of larger samples and more detailed analysis, as this will also advance our understanding of BLRs.

In the present paper, we compile the latest RM sample with high-resolution observations from *Hubble Space Telescope* (*HST*), calibrate the virial factors based on $M_{\bullet} - L_{\text{bul}}$ relation, and investigate the correlation between the virial factors with the BLR/AGN properties. In Section 2, we present the sample used in this paper and describe how we measure the host luminosities and the BLR/AGN properties. The calibrating procedure of the virial factors and their correlations with the BLR/AGN properties are provided in Section 3. We provide some discussion in Section 4 and summarize our main conclusions in Section 5. We adopt the standard Λ CDM cosmology with the parameter of $H_0 = 67 \text{ km s}^{-1} \text{ Mpc}^{-1}$, $\Omega_{\Lambda} = 0.68$, and $\Omega_{\text{m}} = 0.32$ (Planck Collaboration et al. 2014, 2020) in this paper.

2. DATA AND MEASUREMENT

2.1. Sample

Our sample is mainly based on the compilation in Du & Wang (2019), which includes mostly low-redshift AGNs with $z \lesssim 0.2$. Additionally, we have incorporated some of the latest RM samples from Bao et al. (2022) and Hu et al. (2021), as well as individual objects such as PG 2130+099 (Hu et al. 2020), PG 0026+129 (Hu et al. 2020), PG 0923+201 (Li et al. 2021), IC 4329A

(Bentz et al. 2023), Mrk 50 (Barth et al. 2011, 2015), Zw 229 (Barth et al. 2011), Mrk 704 (De Rosa et al. 2018), I Zw I (Huang et al. 2019). In order to measure the luminosity of their host galaxies, we conducted a systematic search of this sample in the *HST* archive and identified 72 objects with high-quality images suitable for host and AGN decomposition. Our goal is to calibrate the virial factor as accurately as possible based on the luminosity of the host galaxies. Therefore, we focus on low-redshift AGNs and do not include the samples with higher redshifts from the Sloan Digital Sky Survey RM (SDSS-RM) project (Shen et al. 2023) and the Australian Dark Energy Survey (OzDES) RM Program (Malik et al. 2023; Yu et al. 2023). The names, coordinates, redshifts, and Galactic extinctions are listed in Table 1.

2.2. Decomposition of AGNs and host galaxies

In order to extract the luminosities of the spheroids in the host galaxies of the RM AGNs, it is necessary to decompose the contribution of the bright point spread function (PSF) from the AGNs and the components (e.g., disks, bulges, and bars) of the host galaxies. The host decomposition of some objects has been presented in, e.g., Bentz et al. (2009), Bentz et al. (2013), Du et al. (2014), and Kim et al. (2017). However, we perform the host composition for all of the objects in the sample using a same procedure in the present paper to ensure the consistency of the decomposition.

2.2.1. *HST* images

The *HST* images of the objects were obtained using the instruments Advanced Camera for Surveys (ACS, Lucas & Ryon 2022), Wide Field Planetary Camera 2 (WFPC2, Gonzaga et al. 2010), and Wide Field Camera 3 (WFC3, Gennaro 2018). ACS, WFPC2, and WFC3 have different channels and cameras. The detailed informations of the *HST* observations are provided in Table 1.

To calibrate the virial factors using the $M_{\bullet} - L_{\text{bul}}$ relation in V band ($M_{\bullet} - L_{\text{V,bul}}$), we opted to utilize the *HST* images taken with the filters close to the V band (e.g., F547M, F550M, F555W and F606W). If suitable images were not available, we chose to use the images taken with the filters at shorter or longer wavelengths (F438W, F675W, F791W etc.). Observations with higher signal-to-noise ratios (S/N) are consistently favored. The high contrast between the AGN (the central point source) and its host galaxy poses a challenge: a single exposure cannot ensure both a sufficient S/N ratio for the host galaxy and prevent saturation of the AGN. Fortunately, most observations have both short and long exposures (e.g., Bentz et al. 2009, 2013), which enables us to extract the host information even with very high contrast between the AGN and host components.

We utilized the calibrated science images generated from the data processing pipeline of *HST* archive¹. As the sharp peak (PSF) of science images generated by the pipeline is sometimes mis-classified and marked as cosmic rays, we used L.A.Cosmic package (van Dokkum 2001)² to identify and remove the cosmic rays. The removal of cosmic rays was performed for each individual science image. We then conducted a visual inspection of all processed images to ensure the preservation of the PSF. Subsequently, we aligned and combined the cosmic-ray-cleaned images, and corrected the distortion using DrizzlePac package (Gonzaga et al. 2012). It should be noted that we did not perform sky subtraction and cosmic-ray removal in the DrizzlePac operation.

2.2.2. Generation of PSF

Generating an accurate PSF is crucial in the host decomposition. The PSF varies slightly in different positions of the CCD, and the movements of the secondary mirror (SM) at different times also modulate the PSF profiles (Kim et al. 2008; Makidon et al. 2006). Additionally, the sampling of PSF and its sub-pixel displacement in the corresponding position of the AGN introduce uncertainties to some extent. Therefore, we follow these steps to generate the PSF model as accurately as possible.

We first followed the standard PSF simulation procedure by TinyTim (Krist et al. 2011). The SM movements were derived from the *HST* focus model³. During this step, an oversampling of 10 times is used when generating the PSF models by TinyTim. Secondly, we placed the PSF in the same position as the original AGN peak for each science frame, then undersampled the PSF to match the pixel size of the science frame. We then convolved the PSF with the charge diffusion kernel (Krist et al. 2011), and combined these PSF frames using DrizzlePac with the same parameters as the science frames. Finally, the final PSF model was extracted from the combined PSF image. We have checked that the generated PSF works well in the subsequent host decomposition.

2.2.3. GALFIT fitting

We use GALFIT version 3.0 (Peng et al. 2010) to model the surface brightness of the AGNs and their host galaxies. The following components are utilized in the image fitting: (1) a PSF (see Section 2.2.2) to model the AGN component, (2) several Sérsic profiles to model the bulge (pseudobulge), disk and bar (if needed) components (only one Sérsic for elliptical galaxy), and (3)

a constant to model the sky background. The Sérsic profile is expressed as

$$\Sigma(r) = \Sigma_e \exp \left\{ -\kappa \left[\left(\frac{r}{r_e} \right)^{1/n} - 1 \right] \right\} \quad (2)$$

where Σ_e is the surface brightness at the effective radius r_e (also known as half-light radius), n is the Sérsic index, and κ is a variable coupled with n (ensuring that half of the flux is within r_e). The special case of the Sérsic profile with $n = 4$ corresponds to the de Vaucouleurs profile, and the case with $n = 1$ is equivalent to an exponential disk. These two cases are widely adopted in the modeling of bulge (elliptical) and disk components of galaxies, respectively (Bentz et al. 2009; Du et al. 2014; Kim et al. 2017). Fourier mode, coordinate rotation and truncation functions are also employed if the host galaxies show distortion or asymmetry.

The precision of the sky subtraction is crucial for accurate measurement of the host components. Following the method in Kim et al. (2017), we initially determine the sky level using the `sky` task in IRAF and utilize it as the initial input for the GALFIT fitting. We include as large a region as possible in the fitting to encompass more sky area. After obtaining the best parameters in the fitting, we verify the sky background using the method provided in Kim et al. (2017) by checking if the cumulative flux reaches a constant at large radii.

After the fitting, the magnitudes of the host spheroids are converted to the V-band luminosities using the host template spectrum of the bulge from Kinney et al. (1996). For the images taken with red filters (e.g., F702W, F791W), their pass bands exceed the wavelength range of the bulge template (Kinney et al. 1996). In such cases, we switch to using the template of S0 galaxies (Kinney et al. 1996) instead, which looks very similar to the bulge template at overlapping wavelengths. During the conversion, the template is redshifted and reddened by Galactic extinction of Schlegel et al. (1998) (listed in Table 1).

The uncertainties of the magnitudes of the host components decomposed by GALFIT are generally dominated by systematic errors (Kim et al. 2008, 2017). These systematic errors arise from (1) the uncertainties in the PSF model and (2) over- or under-estimation of the sky background. To evaluate the uncertainties caused by the PSF model, we collect the images of several (5-10) bright and unsaturated stars at similar positions of the CCD and taken with the same instruments and filters as each object. We generate a series of PSF models using these stars, and use these PSF models to perform the GALFIT fitting. The differences of the parameters obtained by these PSF models are regarded as the uncertainties caused by the PSF model. The uncertainties of the sky background determination may contribute to the uncertainties of the bulge magnitudes, we simply adopted 0.1 mag as extra uncertainties and added

¹ <http://mast.stsci.edu>

² Which is provided in the ASTROPY image reduction package - CCDPROC

³ <https://www.stsci.edu/hst/instrumentation/focus-and-pointing/focus/hst-focus-model>

them to the error bars of the bulge magnitudes from the GALFIT fitting by quadratic summation in the following analysis (Bentz et al. 2009, 2013). For some objects (21 out of the 72 objects), the Sérsic indexes of their bulge components cannot be well constrained due to their relatively poor S/N. In such cases, we fix their Sérsic indexes as 4 and add additional uncertainties of 0.3 mag to their magnitudes (Kim et al. 2008). For the luminosity distance uncertainties, we follow Bentz et al. (2013) and include an error of 500 km/s in recession velocity. Furthermore, the template utilized in the k-correction (to V band) introduces additional uncertainties. In accordance with Kim et al. (2017), we assess these uncertainties by examining various templates for the bulge spectra and consider the corresponding scatter as the errors. The final uncertainties of the magnitudes are derived by adding these uncertainties in quadrature. The best parameters of the GALFIT fitting are provided in Table 2. The best fitting of the *HST* images and their residuals are provided in Figures 1.

2.3. Classification of pseudo and classical bulges

The principle behind calibrating the virial factors using the M_{\bullet} – spheroid relations ($M_{\bullet} - \sigma_{*}$, $M_{\bullet} - L_{\text{bul}}$, or $M_{\bullet} - M_{*,\text{bul}}$) is based on the assumption that both the active and inactive galaxies adhere to the same relations. Galaxies with PB are claimed to significantly displaced from the M_{\bullet} – spheroid relations of CB and ellipticals (e.g., Kormendy & Ho 2013). Consequently, Ho & Kim (2014) calibrated the virial factors of the AGNs with classical bulges (ellipticals) and pseudobulges separately, based on the $M_{\bullet} - \sigma_{*}$ relation. In the present paper, we follow Ho & Kim (2014) but use the $M_{\bullet} - L_{V,\text{bul}}$ to calibrate the virial factors of AGNs by separating their bulge classification. To classify the bulge type of the RM AGNs, we adopt the criterion used in Ho & Kim (2014) and Kim et al. (2017), where PB are defined as the objects with a Sérsic index $n_b < 2$, and also take into consideration that PB generally favor low bulge-to-total luminosity ratio of B/T < 0.2 (e.g., Fisher & Drory 2008; Gadotti 2009; Ho & Kim 2014). Our bulge classifications are generally in agreement with previous studies (Guyon et al. 2006; Ho & Kim 2014; Kim et al. 2017). We found a PB percentage of 44% (32/72), which is slightly higher than the 38.3% reported by Ho & Kim (2014) and Guyon et al. (2006), but lower than the result of Fisher & Drory (2008) (67%). The elliptical and CB galaxies have the same $M_{\bullet} - \sigma_{*}$ relation (Kormendy & Ho 2013), thus we do not distinguish between them sometimes in the latter text. Our bulge classifications are given in Table 2. Some notes on individual objects are provided in Appendix A.

2.4. Spectral properties

To investigate how the single-epoch spectral properties control the virial factors, we collect the spectral properties: (1) the flux ratio between Fe II and H β

($\mathcal{R}_{\text{Fe}} = F_{\text{FeII}}/F_{\text{H}\beta}$), where the F_{FeII} represents the Fe II flux between 4434 and 4684Å and $F_{\text{H}\beta}$ is the flux of broad H β , (2-3) the ratios between FWHM and σ_{line} of broad H β line ($\mathcal{D}_{\text{H}\beta}$) from mean and rms spectra, which are considered as an indicator of the line profile, (4) the FWHM ratio between Fe II and H β , (5) the asymmetry (\mathcal{A}) of broad H β , defined as $\mathcal{A} = [\lambda_c(3/4) - \lambda_c(1/4)]/\Delta\lambda(1/2)$ (De Robertis 1985), where $\lambda_c(3/4)$ and $\lambda_c(1/4)$ are the central wavelengths at the 3/4 and 1/4 of the peak height, $\Delta\lambda(1/2)$ is FWHM, and positive (negative) \mathcal{A} indicates stronger blue (red) wings of the line profile, (6-8) the equivalent width of H β ($\text{EW}_{\text{H}\beta}$), [O III] ($\text{EW}_{[\text{O III}]}$), and He II (EW_{HeII}), (9-12) the FWHM and σ_{line} of broad H β emission lines from the mean and rms spectra. These spectral properties are the observables of BLRs (also referred to as “BLR properties”). The majority of these spectral properties can be obtained from literatures, such as Du & Wang (2019). For the properties that cannot be found in such way, we conduct fitting of the spectra found in the public archive and measure these properties ourselves. When possible, we prioritize measuring them from the mean spectrum if corresponding RM data is available, as the mean spectra can effectively represent the properties over the corresponding period of time as RM. However, in the cases where RM data is not accessible, we resort to measuring these properties from single-epoch spectra found in literature or databases. In cases where multiple RM observations are available for a target, we average the values from the multiple measurements.

We perform spectral fitting using DASpec⁴, a multi-component spectral fitting code with a graphical user interface. The core algorithm employed in DASpec is the Levenberg–Marquardt method (Press et al. 1992). We use the following components in the spectral fitting: (1) a power law to model the AGN continuum, (2) a spectral template of bulge provided in Kinney et al. (1996) to model the host galaxy, (3) a Fe II emission template constructed by Boroson & Green (1992), (4) one or two Gaussians to model each of the broad emission lines (e.g., H β , He II $\lambda 4686$, and He I $\lambda 4471$), (5) one or two Gaussians to model each of the narrow emission lines (e.g., [O III] $\lambda\lambda 4959, 5007$, H β , and He II $\lambda 4686$, etc.). The fitting is performed in the windows 4170 - 4260Å and 4430 - 5550Å in the rest frame. All of the narrow emission lines are fixed to have the same line profile and velocity shift. The flux ratio between [O III] $\lambda 4959$ and [O III] $\lambda 5007$ is fixed to 1/3 (Osterbrock & Ferland 2006). In NLS1s, the narrow H β lines are very weak and difficult to be deblended from the broad H β . In such cases, we fix the flux of narrow H β as one tenth of the [O III] $\lambda 5007$ (Du et al. 2014; Du & Wang 2019). In

⁴ The living code for DASpec is available at <https://github.com/PuDu-Astro/DASpec>, while the version used in the present paper is available at <https://doi.org/10.5281/zenodo.12578529>.

the spectral fitting, the host is fixed to have the flux extracted from the GALFIT fitting (see Section 2.2.3). The flux of the host components decomposed by GALFIT in the aperture of the corresponding spectroscopic observation is adopted here. We examine the components of the host galaxies in the spectral fitting and they appear to be reasonable. We also test the Fe II template from Park et al. (2022), the fitting results are consistent. The line spread functions caused by the instrumental broadening are removed from the measurements of the line widths. The spectral properties (as well as the RM time lags and luminosities) are provided in Tables 3 and 4.

3. ANALYSIS

3.1. Calibration of virial factors

To calibrate the virial factors, we perform a joint fitting for the combined sample of RM AGNs and inactive galaxies following the method as described in Woo et al. (2013) and Woo et al. (2015). If we assume AGNs and inactive galaxies share the same importance in composing the $M_{\bullet} - L_{V,\text{bul}}$ relation, we can obtain the slopes, intercepts, and the virial factors by minimizing (called Approach I)

$$\chi^2 = \sum_i^M \frac{(\log M_{\bullet,i} - \alpha \log L_{\text{bul},i} - \beta)^2}{\sigma_{\text{int}}^2 + (\alpha \sigma_{L_{\text{bul},i}})^2 + \sigma_{M_{\bullet,i}}^2} + \sum_j^N \frac{(\log f + \log \text{VP}_{\bullet,j} - \alpha \log L_{\text{bul},j} - \beta)^2}{\sigma_{\text{int}}^2 + (\alpha \sigma_{L_{\text{bul},j}})^2 + \sigma_{\text{VP}_{\bullet,j}}^2} \quad (3)$$

by Levenberg-Marquardt algorithm (Press et al. 1992), where the first summation represents the term of inactive galaxies, the second one is the term of RM AGNs, M, N are their numbers, $\text{VP}_{\bullet} = V^2 R_{\text{BLR}}/G$ is the virial product, σ_{int} is the intrinsic scatter of the relation, and $\sigma_{L_{\text{bul}}}$, $\sigma_{M_{\bullet}}$, and $\sigma_{\text{VP}_{\bullet}}$ are the uncertainties of the bulge luminosity, SMBH mass, and virial product, respectively. We adopt the sample of inactive galaxies in Kormendy & Ho (2013). However, the uncertainties of their V-band magnitudes are not provided in Kormendy & Ho (2013). For simplicity, we utilize a typical uncertainty of 0.2 dex in our analysis. As mentioned in previous sections, there are 4 combinations of velocity-width tracers (so thus 4 different VPs). We carry out the fitting separately for the four combinations. We perform the joint fitting for (1) the sample of the AGNs and inactive galaxies with PB (PB sample) and (2) the sample with classical bulges and ellipticals (CB sample), by using the FITEXY estimator (Tremaine et al. 2002; Woo et al. 2013, 2015). The calibrated virial factors in this case are called “separate-sample” virial factors. For comparison, we also perform the fitting using the total sample (PB + CB), and the calibrated virial factors are called “total-sample” virial factors. The best parameters of the slope, intercepts, virial factors, and intrinsic scatters are provided in Table 5. Because the dynamical range of the bulge lumi-

nosities is limited for the PB sample (see Figure 2), we fix the slope of the PB sample as that of the CB sample.

For comparison, we also calibrate the virial factors using two additional approaches (called Approach II and Approach III). Approach II is similar to Approach I, but without including the intrinsic scatters. This approach can be expressed as

$$\chi^2 = \sum_i^M \frac{(\log M_{\bullet,i} - \alpha \log L_{\text{bul},i} - \beta)^2}{(\alpha \sigma_{L_{\text{bul},i}})^2 + \sigma_{M_{\bullet,i}}^2} + \sum_j^N \frac{(\log f_{\text{BLR}} + \log \text{VP}_{\bullet,j} - \alpha \log L_{\text{bul},j} - \beta)^2}{(\alpha \sigma_{L_{\text{bul},j}})^2 + \sigma_{\text{VP}_{\bullet,j}}^2}. \quad (4)$$

Approach III involves fixing the slope (α_0) and intercept (β_0) to those of the $M_{\bullet} - L_{V,\text{bul}}$ relation of inactive galaxies (Kormendy & Ho 2013) and only solving for the virial factors, which can be obtained by minimizing

$$\chi^2 = \sum_j^N \frac{(\log f_{\text{BLR}} + \log \text{VP}_{\bullet,j} - \alpha_0 \log L_{\text{bul},j} - \beta_0)^2}{(\alpha_0 \sigma_{L_{\text{bul},j}})^2 + \sigma_{\text{VP}_{\bullet,j}}^2}. \quad (5)$$

The virial factors obtained by Approach I are regarded as the primary results. The results from Approaches II and III are provided in Table 5 for comparison.

Figure 2 shows the $M_{\bullet} - L_{V,\text{bul}}$ relation from Approach I, the blue and red points represent the PB and CB samples, respectively. It is evident that the correlations of σ_{line} -based results are slightly tighter than the FWHM-based ones, both for total or PB/CB samples (see also the intrinsic error listed in Table 5), indicating that σ_{line} is likely a better tracer for BLR velocities and for estimating M_{\bullet} (support the claims in Peterson et al. 2004). Because inactive galaxies with PB exhibit smaller M_{\bullet} compared to those with CB, our joint fitting results for the PB sample also deviate from those of the CB. The joint fitting of PB show significantly smaller intercepts than CB (see Table 5). The offset of intercept between the PB and CB is about 1.0 dex for all of the cases (MF, MS, RF, and RS). As a result, the joint fitting (Approach I) of the total sample (PB + CB) show steeper $M_{\bullet} - L_{V,\text{bul}}$ relations. The virial factors calibrated by the PB sample in the present paper are $f_{\text{MF}} = 0.67 \pm 0.28$, $f_{\text{RF}} = 0.91 \pm 0.4$, $f_{\text{MS}} = 2.22 \pm 0.86$ and $f_{\text{RS}} = 2.4 \pm 0.93$, which are consistent with the values of $f_{\text{MF}} = 0.9 \pm 1.9$, $f_{\text{RF}} = 1.3 \pm 0.6$, $f_{\text{MS}} = 3.2 \pm 1.6$, and $f_{\text{RS}} = 4.8 \pm 2.0$ in Ho & Kim (2014) within uncertainties. However, because of the larger sample, the uncertainties of our measurements are significantly smaller. In comparison, our virial factors calibrated by the CB sample are larger than the values in Ho & Kim (2014) by factors of 2 ~ 3 (see Table 5). Additionally, when compared with the virial factors calibrated in Woo et al. (2015) without separating bulge types, our results calibrated using the total sample are also larger by factors of ~ 2. The rationale behind the larger CB virial factors is discussed in Section 4.2.

3.2. Correlations between virial factors and spectral properties

The virial factors calibrated by the $M_{\bullet} - L_{V,\text{bul}}$ relations exhibit large scatters. The intrinsic scatters of the 4 cases (MF, MS, RF, and RS) are all around $0.5 \sim 0.6$ dex (see Table 5). If we use the ‘‘average’’ virial factors from Table 5 and Eqn (1) to calculate the masses of SMBHs, the intrinsic scatters in the virial factors would contribute typical uncertainties of $0.5 \sim 0.6$ dex to the mass estimates. To investigate the correlations between the scatters of virial factors and the spectral properties obtained in Sections 2.4, we define the deviation from the joint fitting (regarded as the virial factor of individual objects) as

$$\log f = \alpha \times L_{V,\text{bul}} + \beta - \log \text{VP}_{\bullet}, \quad (6)$$

where α and β are the slope and intercept obtained by Approach I in Section 3.1. Here, f is f_{MF} , f_{MS} , f_{RF} , or f_{RS} , respectively. For objects that fall below the $M_{\bullet} - L_{V,\text{bul}}$ relations, their $\log f$ values exceed the ‘‘average’’ virial factors of the sample obtained in Section 3.1. Essentially, the $\log f$ here can be considered as the individual virial factors if we assume that the masses predicted from the $M_{\bullet} - L_{V,\text{bul}}$ relations are inherently accurate.

We plot the correlations between the deviations of the separate-sample virial factors and the spectral properties in Figures 3-6 (for MF, MS, RF, and RS, respectively). The case of the total-sample virial factors is provided in Appendix C. In addition, we also plot the correlations of the virial factors with the SMBH masses and dimensionless accretion rates ($\dot{\mathcal{M}}_{\bullet}$) in Figures 3-6. We adopt the definition of accretion rate in (e.g., Du et al. 2014, 2016) as

$$\dot{\mathcal{M}}_{\bullet} = 20.1 \left(\frac{\ell_{44}}{\cos i} \right)^{3/2} m_7^{-2}, \quad (7)$$

where $m_7 = M_{\bullet}/10^7 M_{\odot}$ is the SMBH mass, $\ell_{44} = L_{5100}/10^{44}$ erg s $^{-1}$ is the continuum luminosity at 5100Å, and i is the inclination angle of the accretion disk to the line of sight (LOS). For simplicity, an average of $\cos i = 0.75$ is adopted in this paper. To avoid the self-correlation, we calculate the M_{\bullet} (and then $\dot{\mathcal{M}}_{\bullet}$) using their bulge luminosities (and the best parameters in Table 5) rather than the virial products and the calibrated virial factors. The Spearman’s rank correlation ρ and the corresponding null probabilities p are marked in Figures 3-6.

Here we adopt $p < 0.001$ as a criterion of the significant correlations, and provide the linear regressions for those significant correlations in Figures 3-6. We use the linear regression defined as

$$\log f_{\text{BLR}} = \alpha' * \mathcal{X} + \beta', \quad (8)$$

where \mathcal{X} is one of the BLR/AGN properties in Section 2.4. In Figures 3-6, the dashed lines and the regions

in blue and red show the regressions and the confidence bands (1σ) for the PB and CB samples, respectively. The dashed lines and the regions in grey are those for the total samples. The slopes α' , intercepts β' , and the intrinsic scatters (ϵ') of the linear regressions are listed in Table 6.

Overall, for the PB sample, we find the following correlations:

- f_{MF} shows anti-correlations with $\text{FWHM}_{\text{H}\beta,\text{mean}}$, $\sigma_{\text{H}\beta,\text{mean}}$, and $\mathcal{D}_{\text{H}\beta,\text{mean}}$.
- f_{MF} shows a positive correlation with \mathcal{R}_{Fe} .
- f_{MS} shows anti-correlations with $\sigma_{\text{H}\beta,\text{mean}}$.
- f_{RF} shows anti-correlations with $\text{FWHM}_{\text{H}\beta,\text{rms}}$ and $\sigma_{\text{H}\beta,\text{rms}}$.

For the CB sample, we find the following correlations:

- f_{MF} shows significant anti-correlations with $\text{FWHM}_{\text{H}\beta,\text{mean}}$ and $\mathcal{D}_{\text{H}\beta,\text{mean}}$.
- f_{RF} shows significant anti-correlations with $\text{FWHM}_{\text{H}\beta,\text{mean}}$, $\text{FWHM}_{\text{H}\beta,\text{rms}}$, $\sigma_{\text{H}\beta,\text{rms}}$, $\mathcal{D}_{\text{H}\beta,\text{mean}}$ and $\mathcal{D}_{\text{H}\beta,\text{rms}}$.

For the total sample, we find:

- f_{MF} shows anti-correlations with $\mathcal{D}_{\text{H}\beta,\text{mean}}$.
- f_{MF} , f_{MS} , f_{RF} , and f_{RS} all show positive correlations with M_{\bullet} and anti-correlations with $\dot{\mathcal{M}}$ (not listed in Table 6).

After establishing these correlations between the virial factors and the BLR properties, we can inversely utilize them to provide a better estimate of the virial factor in an AGN if the spectral properties can be measured from its spectrum. Finally, the correlations/anti-correlations between f_{MF} , f_{MS} , f_{RF} , and f_{RS} with M_{\bullet} and $\dot{\mathcal{M}}$ can not be simply used if we do not know the SMBH mass and accretion rate beforehand. However, these correlations do indicate that the virial factors are smaller in the AGNs with smaller SMBH masses and higher accretion rates.

4. DISCUSSION

4.1. Physical driver of the correlations

The calibrated virial factors based on the FWHM (f_{MF} and f_{RF}) tend to show significant anti-correlations with the line widths (FWHM or σ_{line}), for either (or both) of the PB or CB samples. Additionally, the relationships between f_{MF} and $\mathcal{D}_{\text{H}\beta,\text{mean}}$ (for PB and CB), and between f_{RF} , $\mathcal{D}_{\text{H}\beta,\text{mean}}$, and $\mathcal{D}_{\text{H}\beta,\text{rms}}$ (only for CB) are also significant. From the perspective of eigenvector 1 sequence (e.g., Marziani et al. 2001; Shen & Ho 2014), it has been demonstrated that accretion rate drives \mathcal{R}_{Fe} , while the orientation dominates the dispersion of

FWHM at fixed \mathcal{R}_{Fe} . Some works about the line profiles (e.g., Kollatschny & Zetzl 2011) also suggest that the objects with narrower line widths (smaller $\mathcal{D}_{\text{H}\beta}$) have thicker BLRs (can be considered to have larger opening angles). Furthermore, f_{MF} shows a positive correlation with \mathcal{R}_{Fe} for the PB sample. This correlation may stem from the tendency that the high- \mathcal{R}_{Fe} AGNs typically have smaller FWHM and $\mathcal{D}_{\text{H}\beta}$ (see also the next paragraph). Considering that most of the correlations are between the virial factors and the line widths and profiles, the correlation between f_{MF} and \mathcal{R}_{Fe} could possibly be a secondary correlation induced by the correlations between the virial factors and the line widths/profiles. As a small test, we find that there is no residual correlation between $(f_{\text{MF}} - f_{\text{MF}}^{\text{fit}})$ and \mathcal{R}_{Fe} , where $f_{\text{MF}}^{\text{fit}}$ is the linear regression of f_{MF} vs. $\text{FWHM}_{\text{H}\beta, \text{mean}}$ (or $\mathcal{D}_{\text{H}\beta, \text{mean}}$) obtained by Eqn (8). Therefore, the inclination and opening angles are probably the primary physical driver of the strong anti-correlations between the virial factors and line widths and profiles.

The $\text{FWHM}_{\text{H}\beta, \text{mean}}$, $\mathcal{D}_{\text{H}\beta, \text{mean}}$, and \mathcal{R}_{Fe} are mutually correlated (e.g., Marziani et al. 2001; Shen & Ho 2014; Du et al. 2016; Kollatschny & Zetzl 2011). In Figure 7, we also plot the correlations between each pair of these three parameters, color-coded by the virial factors f_{MF} and f_{RF} as detailed in Section 3.2. The tendencies of virial factors are more complicated than the cases in Figures 3-6. In the correlations between $\text{FWHM}_{\text{H}\beta, \text{mean}}$ and $\mathcal{D}_{\text{H}\beta, \text{mean}}$, the smallest virial factors are located at larger $\mathcal{D}_{\text{H}\beta, \text{mean}}$ at fixed $\text{FWHM}_{\text{H}\beta, \text{mean}}$. However, the virial smallest factors only appear at largest $\mathcal{D}_{\text{H}\beta, \text{mean}}$ with lower $\text{FWHM}_{\text{H}\beta, \text{mean}}$, while the largest virial factors are only located at the smallest $\mathcal{D}_{\text{H}\beta, \text{mean}}$ and $\text{FWHM}_{\text{H}\beta, \text{mean}}$, different from the simple anti-correlations between the virial factors and $\mathcal{D}_{\text{H}\beta, \text{mean}}$ and $\text{FWHM}_{\text{H}\beta, \text{mean}}$ in Figures 3-6. Such complicated correlations may probably originate from the coordination of BLR thickness and (opening angle) and the inclination.

The σ_{line} -based virial factors show less correlations with the spectral properties. The only relationships are the correlations between f_{MS} and $\sigma_{\text{H}\beta, \text{mean}}$. This is likely due to the dominance of turbulent motion rather than Keplerian rotation in σ_{line} (e.g. Kollatschny & Zetzl 2011, and its reduced susceptibility to the influence of the inclination angle.)

The total-sample correlations between the virial factors and M_{\bullet} are also significant. These correlations are evidently due to the deviation of the $M_{\bullet} - L_{\text{V, bul}}$ relation of PB from that of CB. The galaxies with PB systematically exhibit smaller SMBH masses. Consequently, in Figures 3-6, the PB (the blue points) are all situated in the lower left corners in the correlations of virial factors and M_{\bullet} . The situation is similar to the anti-correlations between the virial factors and the accretion rates. The smaller virial factors in AGNs with high accretion rates, coupled with their smaller BLR radii (e.g., Du et al.

2015, 2016, 2018), may help alleviate the conundrum of disproportionately over-massive SMBHs in AGNs in the high-redshift universe (e.g., Farina et al. 2022; Goulding et al. 2023; Harikane et al. 2023; Pacucci et al. 2023; Maiolino et al. 2024).

4.2. Comparison with previous results

As mentioned in Section 3, the average virial factors of the PB sample calibrated in this paper are consistent with the factors obtained in Ho & Kim (2014). However, the average virial factors of the CB sample calibrated here are larger than the values in Ho & Kim (2014). The large virial factors of the CB sample also cause the average virial factors calibrated from the total sample to be larger than those in the previous works (e.g., Onken et al. 2004; Park et al. 2012; Grier et al. 2013; Woo et al. 2015). Actually, the virial factors calibrated by the $M_{\bullet} - \text{spheroid}$ relation or obtained in dynamical modeling of BLRs have very large scatters. The intrinsic scatters of the virial factors obtained in the present paper are roughly 0.5 ~ 0.6 dex and the largest deviation of the virial factor of an individual object from the best fitting is ~ 1.4 dex. Such large scatter means that the different samples used in different analysis may result in different virial factors. In Figures 3-6, we have denoted the same objects as in Ho & Kim (2014) and Woo et al. (2015) with stars and squares, respectively. It is evident that the CB sample in the present paper contains several more objects with very large virial factors, which cause the average virial factors calibrated by the CB sample (and the total sample) larger than those in the previous works. As a test, we select the same objects as Woo et al. (2015) and get the average virial factors (RF and RS) of 1.8 and 7.7 which are still larger than the results (1.12 and 4.47) in Woo et al. (2015).

Considering that the virial factors reported by Woo et al. (2015) and Ho & Kim (2014) were based on the $M_{\bullet} - \sigma_{*}$ relationship, we present the correlation between stellar velocity dispersion (σ_{*}) and bulge magnitude (i.e. Faber-Jackson relationship) in Figure 8. The large circles represent the RM AGNs whose σ_{*} can be found in the literature (Ho & Kim 2014), and the open triangles represent the inactive galaxies. We found that the inactive galaxies with both PB and CB satisfy the same Faber-Jackson relationship; however, the CB AGNs seem biased towards smaller σ_{*} and brighter bulge luminosity. Statistically, when we don't classify the bulge type, total AGN sample deviate from the Faber-Jackson relationship of inactive galaxies by about 0.04 dex. This offset propagates to a virial factor of about 0.2 dex, exactly the same deviation between our results and those of Woo et al. (2015). For separate PB and CB samples, we found that AGN PB sample lie on the same line as their inactive counterparts, while the AGN CB sample have an offset of about 0.067 dex, equivalent to 0.3 dex for the virial factor. Both of them

are consistent with the differences between our results and those of Ho & Kim (2014).

The deviation of AGNs from the Faber-Jackson relationship of inactive galaxies could be attributed to three possible explanations: (a) the incompleteness of the AGN sample, (b) the intrinsic differences between AGNs and inactive galaxies, although this is contrary to the fundamental hypothesis of the calibration in the present paper (and all previous works), and (c) possible observational effects on the velocity dispersion measurements in AGNs, as they tend to reside at higher redshifts than the nearby quiescent galaxies used for the Faber-Jackson relationship, which could cause the apertures of spectra to cover larger areas of the host galaxies. Determining the main reason for this deviation is still an open question. If we consider the first explanation to be correct, we can make a correction to the virial factors calibrated in the present paper by systematically reducing the CB virial factors by 0.3 dex and the total-sample virial factors by 0.2 dex.

In Yu et al. (2019), the correlations between the virial factors and several BLR/AGN properties (e.g., FWHM, σ_{line} , \mathcal{R}_{Fe} , and L_{5100}) were investigated. Their study found correlations between f_{MF} and $\text{FWHM}_{\text{H}\beta, \text{mean}}$, and between f_{MF} and $\mathcal{D}_{\text{H}\beta, \text{mean}}$ in the CB galaxies. Our results for the PB and CB samples also show similar correlations, but with higher significance. Although they did not show the calibrated virial factors of the PB, they did present the calibrations of the total sample (with PB scaled by 1/3.80). Their calibrated virial factors (f_{MS} and f_{RS}) from the total sample only show significant anti-correlations with Eddington ratios, which are similar to our finding in terms of \mathcal{M} in the total sample.

The significant anti-correlations between the virial factors and the line widths found in Collin et al. (2006), Mejía-Restrepo et al. (2018), and Yu et al. (2019) appear contradictory to the results that AGNs with the bars and PB have relatively smaller virial factors in Graham et al. (2011) and Ho & Kim (2014), since NLS1s are more likely hosted in the barred and PB galaxies as compared to their broad-line counterparts (Orban de Xivry et al. 2011; Kim et al. 2017). Our results provide clarity on this matter: the virial factors of the PB and CB samples both show anti-correlations with the line widths (FWHM or σ_{line}) and with the line profiles ($\mathcal{D}_{\text{H}\beta}$), however, the average virial factors of the AGNs with PB are systematically smaller than those of the CB AGNs. In conclusion, accounting for the bulge type is crucial when investigating trends between the virial factor and spectral properties to avoid conflating the impact of galaxy morphology and that of structural BLR effects.

4.3. Line-width- and line-profile-corrected virial factors

In Section 3.2, we present the correlations between the virial factors and the spectral properties. The correlations of the PB and CB samples, respectively, are more significant than the correlations of the total sample (do

not distinguish PB and CB). The significant separate-sample correlations are the relationship between the virial factors and FWHM, $\sigma_{\text{H}\beta}$, and $\mathcal{D}_{\text{H}\beta}$ (representing the line profile) from the mean or rms spectra. Therefore, utilizing these correlations, we can provide more accurate estimates of the SMBH masses, which are superior to the SMBH masses based on the average virial factors. If we know the bulge types of the objects in advance, we can use the line-width-corrected or line-profile-corrected separate-sample FWHM-based virial factors from Eqn (8) and the parameters in Table 6 (or also considering the offset caused by the difference between the $M_{\bullet} - \sigma_{\star}$ and $M_{\bullet} - L_{\text{bul}}$ relations in Section 4.2). We show the comparisons between the M_{\bullet} calculated from the luminosities of the host spheroids ($M_{\bullet, M_{\bullet} - L_{\text{V, bul}}}$) and those obtained from the average and the corrected virial factors ($M_{\bullet, \text{RM}}$) in Figure 9. As examples, we only provide here the $M_{\bullet, \text{RM}}$ calculated by using the $\text{FWHM}_{\text{H}\beta, \text{mean}}$ - and $\mathcal{D}_{\text{H}\beta, \text{mean}}$ -corrected f_{MF} . For clarity, we do not plot the error bars in order to show clearly the differences between the SMBH masses using the average virial factors and the line-width- and line-profile-corrected virial factors. We use the standard deviation of $M_{\bullet, \text{RM}}/M_{\bullet, M_{\bullet} - L_{\text{V, bul}}}$ to evaluate the scatters. It is obvious that the M_{\bullet} from the line-width- and line-profile-corrected virial factors shows significantly smaller scatters than the cases with the average virial factors. This suggests that the line-width and line-profile-corrected virial factors indeed provide better estimates of the SMBH masses in RM AGNs. If we do not know the bulge types of the AGNs in advance, we can use the $\mathcal{D}_{\text{H}\beta, \text{mean}}$ -corrected f_{MF} or f_{RF} for the total sample to get improved estimates of the SMBH masses.

4.4. New single-epoch SMBH mass estimators

The RM campaign of super-Eddington accreting massive black holes (SEAMBHs) discovered that the SEAMBHs deviate significantly from the traditional $R_{\text{H}\beta} - L_{5100}$ relation (e.g., Du et al. 2015, 2016, 2018). Recently, Du & Wang (2019) introduced a new scaling relation ($R_{\text{H}\beta} - L_{5100} - \mathcal{R}_{\text{Fe}}$) that provides more accurate estimates of the BLR sizes for the AGNs with both of low and high accretion rates. Their $R_{\text{H}\beta} - L_{5100} - \mathcal{R}_{\text{Fe}}$ relation is given by $\log(R_{\text{H}\beta}/\text{lt} - \text{days}) = (1.65 \pm 0.06) + (0.45 \pm 0.03) \log \ell_{44} - (0.35 \pm 0.08) \mathcal{R}_{\text{Fe}}$. Therefore, by combining this with the line-width- and line-profile-corrected virial factors provided in Section 3.2, we can tentatively establish new single-epoch estimators of the SMBH masses, based on the current very limited sample in the present paper.

From the line-width- and line-profile-corrected f_{MF} and the $R_{\text{H}\beta} - L_{5100} - \mathcal{R}_{\text{Fe}}$ relation, the new estima-

tors for the SMBH masses of the PB AGNs are

$$\begin{aligned} \log(M_{\bullet}/M_{\odot}) &= (0.45 \pm 0.03) \log \ell_{44} - (0.35 \pm 0.08) \mathcal{R}_{\text{Fe}} \\ &+ 2 \log(\text{FWHM}_{\text{H}\beta}/\text{km s}^{-1}) - (0.82 \pm 0.19) \mathcal{D}_{\text{H}\beta, \text{mean}} \\ &+ (2.25 \pm 0.35), \end{aligned} \quad (9)$$

$$\begin{aligned} \log(M_{\bullet}/M_{\odot}) &= (0.45 \pm 0.03) \log \ell_{44} + (0.82 \pm 0.29) \mathcal{R}_{\text{Fe}} \\ &+ 2 \log(\text{FWHM}_{\text{H}\beta}/\text{km s}^{-1}) - (0.17 \pm 0.24), \end{aligned} \quad (10)$$

$$\begin{aligned} \log(M_{\bullet}/M_{\odot}) &= (0.45 \pm 0.03) \log \ell_{44} - (0.35 \pm 0.08) \mathcal{R}_{\text{Fe}} \\ &+ (0.18 \pm 0.33) \log(\text{FWHM}_{\text{H}\beta}/\text{km s}^{-1}) \\ &+ (6.89 \pm 1.12), \end{aligned} \quad (11)$$

$$\begin{aligned} \log(M_{\bullet}/M_{\odot}) &= (0.45 \pm 0.03) \log \ell_{44} - (0.35 \pm 0.08) \mathcal{R}_{\text{Fe}} \\ &+ 2 \log(\text{FWHM}_{\text{H}\beta}/\text{km s}^{-1}) \\ &- (1.96 \pm 0.51) \log(\sigma_{\text{H}\beta}/\text{km s}^{-1}) \\ &+ (6.88 \pm 1.59), \end{aligned} \quad (12)$$

and the new estimators for the CB AGNs are

$$\begin{aligned} \log(M_{\bullet}/M_{\odot}) &= (0.45 \pm 0.03) \log \ell_{44} - (0.35 \pm 0.08) \mathcal{R}_{\text{Fe}} \\ &+ (0.58 \pm 0.26) \log(\text{FWHM}_{\text{H}\beta}/\text{km s}^{-1}) + (6.6 \pm 0.94), \end{aligned} \quad (13)$$

and

$$\begin{aligned} \log(M_{\bullet}/M_{\odot}) &= (0.45 \pm 0.03) \log \ell_{44} - (0.35 \pm 0.08) \mathcal{R}_{\text{Fe}} \\ &+ 2 \log(\text{FWHM}_{\text{H}\beta}/\text{km s}^{-1}) - (0.61 \pm 0.11) \mathcal{D}_{\text{H}\beta, \text{mean}} \\ &+ (2.7 \pm 0.24). \end{aligned} \quad (14)$$

It is worth pointing out that Eqn (10) employs the \mathcal{R}_{Fe} -correct f_{MF} and Eqn (11) employs the $\text{FWHM}_{\text{H}\beta}$ -corrected f_{MF} . If the bulge types are not known in advance, the new estimator is

$$\begin{aligned} \log(M_{\bullet}/M_{\odot}) &= (0.45 \pm 0.03) \log \ell_{44} - (0.35 \pm 0.08) \mathcal{R}_{\text{Fe}} \\ &+ 2 \log(\text{FWHM}_{\text{H}\beta}/\text{km s}^{-1}) - (0.53 \pm 0.13) \mathcal{D}_{\text{H}\beta, \text{mean}} \\ &+ (2.19 \pm 0.28), \end{aligned} \quad (15)$$

From the line-width-corrected f_{MS} and the $R_{\text{H}\beta} - L_{5100} - \mathcal{R}_{\text{Fe}}$ relation, the new estimator for the SMBH masses of the PB AGNs is

$$\begin{aligned} \log(M_{\bullet}/M_{\odot}) &= (0.45 \pm 0.03) \log \ell_{44} - (0.35 \pm 0.08) \mathcal{R}_{\text{Fe}} \\ &+ (0.35 \pm 0.48) \log(\sigma_{\text{H}\beta}/\text{km s}^{-1}) + (6.42 \pm 1.51), \end{aligned} \quad (16)$$

As examples, we present the comparisons of the SMBH masses from the $M_{\bullet} - L_{\text{V, bul}}$ relation, and the single-epoch SMBH masses ($M_{\bullet, \text{SE}}$) from the $\mathcal{D}_{\text{H}\beta, \text{mean}}$ -corrected and the $\text{FWHM}_{\text{H}\beta, \text{mean}}$ -corrected estimators and from the traditional estimator (the $R_{\text{H}\beta} - L_{5100}$ from [Bentz et al. 2013](#) with the average total-sample virial factor) in Figure 10. It is obvious that the new SMBH mass estimators can all yield SMBH masses with significantly smaller scatters than those from the traditional method. Moreover, it is surprising to note that the Eqn (11) exhibits weak dependence on $\text{FWHM}_{\text{H}\beta, \text{mean}}$. It should be noted that these new single-epoch estimators are derived under the assumption of the existence of an intrinsic scatter-free $M_{\bullet} - L_{\text{V, bul}}$ relation, and the premise that all AGNs adhere to this relationship. On the one hand, the validity of this assumption requires further investigation. On the other hand, these estimators will propagate the scatter of the $M_{\bullet} - L_{\text{V, bul}}$ relationship to the measurement errors of SMBH masses of the AGNs. This is also the reason why the scatters in Figures 9 and 10 are larger than those in Figure 6 of [Du & Wang \(2019\)](#). Furthermore, it is important to emphasize that these estimators are only based on very limited sample in the present paper. It could be possibly necessary to apply the correction to the average virial factors (0.3 dex for CB and 0.2 dex for total) as discussed in Section 4.2. A more detailed BLR model is also required to fully comprehend these correlations in the future.

5. SUMMARY

We employed the latest nearby RM sample and the $M_{\bullet} - L_{\text{V, bul}}$ relations of inactive galaxies in [Kormendy & Ho \(2013\)](#) to calibrate the virial factors. We classified the RM objects into the PB and CB samples based on their high-resolution *HST* images, and calibrated the virial factors for the two individual samples and for the total PB+CB sample of the RM AGNs. We found that the virial factors have large intrinsic scatters (0.5 ~ 0.6 dex). Then we systematically investigated the scatters of the virial factors and found strong anti-correlations between the virial factors and the line widths or line profiles from the mean or rms spectra for both of the PB and CB samples. The physical driver of these relationships is probably the inclination or opening angle of BLR. Based on the correlations between the virial factors and the spectral properties, we established relationships to get the corrected virial factors which can provide more accurate RM masses. At the end, we tentatively established new single-epoch mass estimators for large AGN samples by taking into account the dependencies of the virial factors on the line widths and line profiles.

1 We thank C. Hu, D.-W. Bao, and S.-S. Li for their
2 assistance in organizing the mean and rms spectra used
3 for measuring the spectral properties, and all the mem-
4 bers of the IHEP AGN Group for their helpful dis-
5 cussions. We acknowledge the support by National
6 Key R&D Program of China (grants 2021YFA1600404,
7 2023YFA1607903), by the National Science Foundation
8 of China through grants NSFC-12333003, -12022301, -
9 11991051, -11991054, -11873048, -11833008, by Grant
10 No. QYZDJ-SSW-SLH007 from the Key Research Pro-
11 gram of Frontier Sciences, Chinese Academy of Sciences
12 (CAS), and by the China Manned Space Project CMS-
13 CSST-2021-A06.

14 Some of the data presented in this article were ob-
15 tained from the Mikulski Archive for Space Telescopes
16 (MAST) at the Space Telescope Science Institute. The
17 specific observations analyzed can be accessed via [doi:](https://doi.org/10.17909/bf5m-v928)
18 [10.17909/bf5m-v928](https://doi.org/10.17909/bf5m-v928)

Software: `GALFIT` (Peng et al. 2010), `TinyTim` (Krist et al. 2011), `DrizzlePac` (Gonzaga et al. 2012), `DASpec` (Du 2024)

APPENDIX

A. NOTES FOR INDIVIDUAL OBJECTS

Here, we give some comments on the host decomposition and bulge classification of each individual object.

Mrk 335. We obtained a B/T of 0.26, which falls between the values reported by [Kim et al. \(2017\)](#) (0.21) and [Bentz et al. \(2009\)](#) (0.39).

PG 0007+106. We can see spiral arms (or tidal structures) in the UVIS1/F547M image. We fitted the host galaxy with hybrid of spiral arms and a disk, and obtained B/T = 0.29 and $n = 1.8$. [Bentz & Manne-Nicholas \(2018\)](#) reported B/T of $\sim 0.16, 0.28, 0.49$ (for their inner bulge, bulge, bulge+inner bulge, respectively) and $n = 1.1$. Considering the relatively high B/T, we classified this target as a CB galaxy.

I Zw1. Compared with the F105W images, its F438M images contain less signal from the host galaxy. If we released the Sérsic index as a free parameter in the fitting, the GALFIT model tended towards a nonphysical model. To address this, we fixed $n = 1.73$ as provided by [Huang et al. \(2019\)](#). This results in a B/T of 0.31, which is smaller than the value reported by [Huang et al. \(2019\)](#) (B/T = 0.52). In addition, the F105W and F814W images revealed clear spiral structures that are barely visible in F438W images. As a result, both B/T values (0.31 or 0.52) should be considered as upper limits. Finally, we classified this galaxy as a PB one.

PG 0052+251. The HRC/F550M image reveals a faint disk component, while WFPC2/F675W image shows a flat disk and a ring-like structure. [Kim et al. \(2017\)](#) fitted this target with a fixed $n = 4$ bulge and a flat disk ($n \sim 0.2$). We obtained $n \sim 2.1$, however our B/T ~ 0.75 is consistent with [Kim et al. \(2017\)](#). Following [Ho & Kim \(2014\)](#), we classified this object as a CB galaxy.

Fairall 9. There is a circumnuclear ring in the central region of this object ([Bentz et al. 2009](#); [Kim et al. 2017](#)). We found it is necessary to add an extra component with a radius of $\sim 0.1''$ (3 pixels) to compensate the mismatch of the PSF. We calculated the PSF magnitude from its 5100Å flux in the spectroscopic observation, and obtained a consistent value (~ 15) as the PSF magnitude from our GALFIT fitting (~ 14.8). The parameters of our bulge and disk components are similar to those of [Bentz et al. \(2009\)](#).

Mrk 590. We obtained B/T = 0.34 and $n = 1.33$. B/T falls within the range between [Kim et al. \(2017\)](#) (0.26) and [Vika et al. \(2012\)](#) (0.48), and is consistent with the result in [Bennert et al. \(2010\)](#). Additionally, we note that the size of galaxy exceeds the FoV, thus B/T should be thought as an upper limit. Therefore, we classified this target as a PB galaxy.

Mrk 1044. It is an S-type galaxy ([HyperLeda](#) and [Orban de Xivry et al. 2011](#)). We can see faint spiral structures from its *HST* image and an obvious ring in the GALFIT residuals. We obtained a PB (B/T = 0.24 and $n = 1$) similar to the result in [Kim et al. \(2017\)](#)

3C 120. It is an S0 galaxy with a tidal arm ([HyperLeda](#) and [de Vaucouleurs et al. 1991](#)). We adopted a bulge + disk model in our fitting, and obtained B/T = 0.16 and $n = 0.7$, which are consistent with the results in [Bentz et al. \(2009\)](#) (B/T = 0.2 and $n = 0.67$) and [Kim et al. \(2017\)](#) (B/T = 0.2). As mentioned in [Ho & Kim \(2014\)](#), a model with a single host component can not be excluded. In accordance with them, we masked the tidal arm, adopted the single-component model, and classified this target as an elliptical.

Ark 120. The HRC image only covers the central region of the host galaxy. Its host galaxy can extends over $\sim 1'$ (the HRC FoV is only $\sim 25''$). The inner ring/spiral is masked during the fitting. We obtained a B/T of 0.35, falling between the results reported by [Bentz et al. \(2009\)](#) (B/T = 0.49) and [Kim et al. \(2017\)](#) (B/T = 0.25). Despite its Sérsic index ($n = 1.73$) slightly smaller than the criteria, considering the large B/T, we still classified this target as a CB galaxy ([Ho & Kim 2014](#)).

UGC 3374. This target is a bar-dominated spiral galaxy with relatively faint spiral arm and disk ([HyperLeda](#), [de Vaucouleurs et al. 1991](#), and [Véron-Cetty & Véron 2006](#)). We classified this target as a CB galaxy since the steep gradient of the surface brightness of the bulge component.

Mrk 6. We masked the dust lane in the core region during the fitting.

Mrk 374. It is identified as a barred spiral galaxy according to [Contini et al. \(1998\)](#) and [Robinson et al. \(2019\)](#). The bar component appears to be more compact with a higher Sérsic parameter ($n \sim 1$) compared to the regular bar structures ($n \sim 0.5$).

Mrk79. The host galaxy exceeds the FoV of the HRC image, and only the central region is covered. By fixing the bar/disk Sérsic index to 0.5, we obtained B/T = 0.27 and $n = 3$. Our B/T is smaller than that reported in [Kim et al. \(2017\)](#) (0.37) and [Bennert et al. \(2010\)](#) (0.41), but larger than the result in [Bentz et al. \(2009\)](#) (B/T = 0.19).

Mrk 382. It is classified as a barred spiral galaxy. Its nuclear region in the *HST* image is saturated. Though we masked out the saturated pixels, GALFIT still tends to fit the central region with a bright and compact Sérsic

component. Therefore, we fixed the PSF magnitude to 16.3, a value simply calculated from 5100\AA flux. The small FoV also suggests that the $B/T = 0.18$ obtained here may be an upper limit. Consistent with Kim et al. (2017), we classified this target as a PB galaxy.

PG 0804+761. Bentz et al. (2009), Kim et al. (2017), and Bennert et al. (2010) reported an exponential bulge profile. We obtained a slightly steeper profile ($n = 1.2$). Guyon et al. (2006) reported this target as bulge-dominated, and the high contrast between the AGN and the host made it difficult to add an additional disk profile in the fitting. Thus, we also classified this target as an elliptical (Ho & Kim 2014).

NGC 2617. HyperLeda⁵ suggests that this is a barred galaxy. However, in contrast, Naim et al. (1995) classified its morphology as a type of Sc, indicating no bar exists. After visually inspecting the data, we prefer to conclude that there is no obvious bar structure. We also tested the fitting with a bar-added model, and the roundness ($b/a = 0.75$) of the bar component suggests that it is more likely a bulge. Finally, we employed a bulge+disk model and obtained $B/T = 0.25$ and $n = 6.67$.

PG 0844+349. Due to the low SN ratio of the ACS/HRC/F550M image, we utilized ACS/WFC1/F625W image instead. The host galaxy exhibits complex spiral structures. Kim et al. (2017) obtained $B/T = 0.64$. We fixed the bulge Sérsic index as 4, and obtained a B/T (0.64) very close to that reported by Kim et al. (2017).

Mrk 704 is more likely to be a barred spiral galaxy according to Malkan et al. (1998). The presence of the bar is necessary in the GALFIT fitting in the present paper. Orban de Xivry et al. (2011) reports $B/T = 0.43$ and $n = 2.88$, while our result gives a flat bulge component with $B/T = 0.35$ and $n = 1.6$. This difference may be primarily due to different *HST* data used in the two analyses. The WFC3/UVIS/F547M image used in our analysis isn't saturated. Taking the presence of the bar into consideration, we classified the bulge as a PB.

Mrk 110. The low S/N ratio makes it difficult to discern any visible host structure at the outer region of the HRC image. Moreover, the descent gradient indicates that the host galaxy exceeds the field of view (FoV) of the HRC image. We obtained $B/T = 0.28$ and $n = 2$, which is a much brighter and steeper result compared to that of Kim et al. (2017) ($B/T = 0.2$ and $n = 1.64$). For consistency, we classified this target as a CB galaxy.

PG 0923+201. This target appears compact in the image, and Hamilton et al. (2008) reports it as an elliptical galaxy. Kim et al. (2017) also fitted an elliptical model to its host image by fixing $n = 4$. Following them, we fixed $n = 4$ in our fitting process.

PG 0923+129. HyperLeda reports it as an S0 galaxy with a clear circumnuclear ring. We obtained a B/T of 0.3 and $n = 0.83$. Although the B/T does not meet the PB criteria (Fisher & Drory 2008), the exponential-like profile led us to classify this object as a PB galaxy.

SDSS J093302.68+385228.0. HyperLeda classifies this target as an elliptical, however, we can see clear structure in the WFC1/F615W image - a spiral arm extending to the central region and forming a circumnuclear ring, which is different from the traditional elliptical characteristic (Fisher & Drory 2008). The central region of the image is saturated, and we masked this region in fitting process. Our fitting reports $B/T = 0.14$ and $n = 0.92$, leading us to classify the bulge as a PB.

PG 0953+414. The host galaxy is faint and compact (Guyon et al. 2006). As discussed in Ho & Kim (2014), it is challenging to robustly constrain the Sérsic index for this object. Therefore, following Bentz et al. (2009) and Kim et al. (2017), we fixed the Sérsic index as 1.5 during the GALFIT fitting.

NGC 3227. Kormendy & Ho (2013) reported this target as a PB galaxy with $B/T = 0.1$. The central region is heavily affected by dust lanes. We masked the dust lanes in the central region and obtained $B/T = 0.34$ and $n = 1.42$. Except for the Sérsic index, our bulge model is in good agreement with Kim et al. (2017). Our B/T should also be considered as an upper limit due to the small FoV of the HRC.

Mrk 142. Bentz et al. (2013) suggested this object does not have a detectable bulge, however the existence of a bar is clear. On the other hand, Du et al. (2014) suggested that there is a bulge component in the host. When employing three components in the fitting (bulge, bar, and disk), we found evidence of a PB ($B/T = 0.2$ and $n = 0.85$) in this object. Additionally, the CCF time lag of the RM campaign in Bentz et al. (2009) is reported to be 2.87 days with respect to the V-band continuum, which deviates significantly from the re-analysis in Li et al. (2013) based on a Bayesian approach ($\tau_{H\beta} = 15.3 \pm 2.7$ days). We employed the result from Li et al. (2013) in the present paper.

PG 1100+772. The central region of the F814W image is saturated.

NGC 3516. Consistent with Kim et al. (2017), we also found a PB component in the fitting ($n = 1.7$). However, we obtained a large B/T of 0.6, which falls within the B/T range (0.52-0.86) reported by Bentz et al. (2009). Due to the small FoV of the HRC image, the B/T here should be an upper limit.

SBS 1116+583A. Our fitting reports $B/T = 0.14$ and $n = 1.6$, leading us to classify this target as a PB (Ho & Kim 2014). The features of secular evolution in the image also supports our classification.

⁵ <http://atlas.obs-hp.fr/hyperleda/>

Arp 151. Also known as Mrk 40. It is an S0 galaxy (HyperLeda and de Vaucouleurs et al. 1991) with no obvious spiral-like structures, and is located in an interacting system. Kim et al. (2017) obtained $B/T = 0.25$ and $n = 4.5$ for this object. Our analysis yielded a similar $n = 4.4$, but a notably larger $B/T = 0.5$. The discrepancy may be attributed to the PSF saturation in the WFPC2 image used in Kim et al. (2017).

NGC 3783. It is a barred spiral galaxy with a ring-like structure surrounding the bulge. Our result indicates the presence of a PB ($n = 1.6$), which is consistent with Kim et al. (2017) ($n = 1.87$).

MCG+06-26-012. This is a barred spiral galaxy. Schade et al. (2000) decomposed the host components and reported a R-band $B/T = 0.27$, consistent with the results of Kim et al. (2017). However, their fitting region cannot cover the entire disk, so their B/T should be considered as an upper limit. We obtained a flatter and fainter bulge component ($n = 1.03$ and $B/T = 0.074$). Considering the existence of a bar, we classified the bulge as a PB.

UGC 06728. This is a barred lenticular galaxy (Bentz 2021), and our fitting gives a result similar to that of Bentz (2021). We obtained a slightly larger bulge ($R_e = 2.96''$ and $B/T = 0.16$) than their result ($R_e = 2.11''$ and $B/T = 0.11$).

Mrk 1310. HyperLeda and the SDSS-GZ2 catalogue (Willett et al. 2013) classify this target as an elliptical, however, a stellar ring is evident in its GALFIT residual from our fitting. Bentz et al. (2013) suggested this target as a ringed spiral galaxy. After masking the stellar ring, we obtained a $B/T = 0.11$, consistent with that in Kim et al. (2017) and smaller than the result in Schade et al. (2000) ($B/T = 0.23$). The bulge can be modeled by a standard de Vaucouleurs profile ($n = 4$). Following Ho & Kim (2014), we classified this objects as a CB galaxy.

NGC 4051. We obtained $n = 1.2$ and $B/T = 0.38$. Considering the small FoV, the B/T is likely overestimated. Our result is also in good agreement with that of Kim et al. (2017).

NGC 4151. The host galaxy extends beyond the FoV of the HRC. Following Kim et al. (2017), we employed the standard bulge/disk model ($n = 4/1$). The residual image shows a faint ring, which may result from the small mismatch between model and the image. We obtained a B/T of 0.53, which falls within the range between Kim et al. (2017) (0.32) and Bentz et al. (2009) (0.72).

PG 1211+143. Due to the low SN ratio of the host galaxy in the HRC/F550M image, we employed WFC1/F625W image instead. We found a bar-like structure near the PSF, which was masked during the fitting. We obtained a B/T of 0.37, similar to the results of Bentz et al. (2009) and Bennert et al. (2010), and less than the result in Kim et al. (2017). The bulge parameter still falls within the CB region (Ho & Kim 2014).

Mrk 202. The central region of the host galaxy has a circumnuclear ring, which we masked out during the GALFIT fitting. We obtained $B/T = 0.44$ and $n = 3.6$, indicating the presence of a CB in the host galaxy. Bentz et al. (2013) employed an extra component to fit the bulge (+ ring) in their fitting. Additionally, Ho & Kim (2014) classified this target as PB galaxy mainly due to the existence of the circumnuclear ring. Despite our fitting parameter falling within the CB range, we still classified this target as a PB galaxy.

NGC 4253. Different from Kim et al. (2017), we employed an unsaturated WFC3/UVIS image in the GALFIT fitting. We found that an extra component is necessary to compensate the inaccuracy of the PSF model (Bentz et al. 2013). Our result is similar to those reported in Bentz et al. (2013), Kim et al. (2017), and Orban de Xivry et al. (2011).

Mrk 50 has been classified as an S0 galaxy by Malkan et al. (1998) and Véron-Cetty & Véron (2006), which differs from the classification by Kim et al. (2017). In our analysis, an unsaturated WFC3/UVIS/F547M image was employed in the GALFIT fitting. We found no obvious features related to secular evolution in the GALFIT residual, and a CB component worked well ($n = 4$ and $B/T = 0.26$). Therefore, classifying this object as a CB galaxy is reasonable. Single epoch properties were measured from the scanned figures in Barth et al. (2011).

PG 1226+023. There are some ring-like structures in the residuals in both our result and that of Kim et al. (2017).

PG 1229+204. In comparison with Kim et al. (2017), we included an additional bar component in the fitting (Hamilton et al. 2008; Ho & Kim 2014). We obtained $B/T = 0.21$ and $n = 1.16$, consistent with the previous works in Bentz et al. (2009) and Bennert et al. (2010).

NGC 4593. There is an apparent circular dust lane around the nucleus, and we masked it in the GALFIT fitting. The object is a barred spiral galaxy, and the WFC3/UVIS FoV can covers most regions of this target. Our fitting result gives that the bulge is flat and faint ($B/T = 0.16$ and $n = 0.96$), which is consistent with Kormendy et al. (2006); Kim et al. (2017); Ho & Kim (2014). We also classified it as a PB galaxy.

IRAS F12397+3333. The central region of its *HST* image is saturated (around the central ~ 5 pixels), and is excluded during the fitting. Although HyperLeda reports that this object has an S-type morphology, its spiral structures (or other features related to secular evolution) are not obvious. Our bulge parameters ($B/T = 0.65$ and $n = 4.1$) are consistent with those of Mathur et al. (2012) ($B/T = 0.59$ and $n = 3.45$). Therefore, we classified it as a CB galaxy.

NGC 4748. An S0 galaxy (2MASX J12521292-1324388) overlays on its host, with a distance between them of ~ 0.7 Mpc. However, no interaction signature can be seen on the host morphology. Similar to Orban de Xivry et al. (2011), we obtained $B/T = 0.14$ and $n = 1.6$. Considering the existence of a bar and stellar ring, we also classified this target as a PB, which is consistent with Ho & Kim (2014).

PG 1307+085. The central region of the image suffers from saturation. HyperLeda and Ho & Kim (2014) classified it as an elliptical galaxy.

PG 1310-108. The central region of the image is saturated, and we masked this area during the fitting. To minimize the systematic error, we fixed the PSF at 15.78 mag (derived by converting the continuum flux from Bao et al. 2022). Subsequently, we obtained $B/T = 0.2$ and $n = 2.6$. Considering the steep surface brightness gradient around the nucleus, we classified this target as a CB.

MCG -6-30-15. The UVIS image reveals a central dust lane, which could potentially influence the fitting results. We employed a mask for the dust lane following the strategy of Hu et al. (2016) and obtained similar bulge properties: $n = 0.83$ and $B/T = 0.04$ (Hu et al. 2016 provided $B/T = 0.06$ and $n = 1.29$). Hu et al. (2016) and our fitting both classified this galaxy as a PB.

NGC 5273. The WFC2 FoV is insufficient to fully cover this target. Our fitting result indicates the presence of a CB ($B/T \sim 0.34$ and $n \sim 4.3$).

IC 4329A. It is an edge-on S0-a galaxy (see HyperLeda, de Vaucouleurs et al. 1991, and Khorunzhev et al. 2012). Its host galaxy is heavily affected by the dust lanes, thus we masked out those dust lanes in our fitting. We obtained a flatter and fainter bulge component ($B/T = 0.19$ and $n = 0.49$) than that in Kim et al. (2017) ($B/T = 0.28$ and $n = 1$). Considering the flat morphology, we classified this object as a PB galaxy. It should be noted that the dust lanes heavily influence the measurements of the bulge morphology and luminosity, thus we didn't employ this target for the analysis in Section 3.

PG 1351+695. This is an S0 galaxy (HyperLeda, de Vaucouleurs et al. 1991, and Bentz et al. 2009). Some dust lanes overlay the central region (Kim et al. 2017). We masked out the dust lanes in the GALFIT fitting and obtained a similar bulge component ($B/T = 0.21$ and $n = 1$) to Kim et al. (2017) ($B/T = 0.21$, $n = 1.3$).

PG 1351+640. In contrast to the bulge + disk models used in Kim et al. (2017), we fitted this target with a single $n = 2.7$ Sérsic profile. Kim et al. (2017) reported $B/T \sim 0.92$, which is also bulge-dominated.

NGC 5548. The bulge Sérsic index is found to be $n = 3.9$, with a corresponding B/T ratio of 0.36. These results are in good agreement with the results reported by Kim et al. (2017) ($B/T = 0.39$ and $n = 4.13$). Moreover, our measured B/T ratio is significantly smaller than the ground-based R-band results obtained by Virani et al. (2000) ($B/T = 0.57$).

PG 1426+015. Kim et al. (2017) and Guyon et al. (2006) classified this target as an elliptical. Our fitting employed bulge and disk components and yielded $B/T \sim 0.7$, slightly larger than the value reported in Schade et al. (2000) ($B/T \sim 0.54$).

Mrk 817. There are clear bar and spiral components in the image (Ho & Kim 2014; Deo et al. 2006). Kim et al. (2017) employed a bar component in their fitting, however, Bentz et al. (2009) and Bennert et al. (2010) did not. We found that the bar component did not significantly affect the bulge profile, and thus still included it in our fitting. Additionally, the host galaxy exceeded the FoV of the HRC image.

PG 1440+356. Kim et al. (2017) suggested that this object is a PB galaxy. Using the UVIS/F547M image, we obtained a slightly smaller and flatter PB ($B/T = 0.15$ and $n = 0.31$) compared to the result in Kim et al. (2017) ($B/T = 0.3$ and $n = 0.64$). The UVIS/F547M image in our fitting shows a more significant disk component than the HRC/F625W image used by Kim et al. (2017). Both Kim et al. (2017) and our fittings indicate the bulge is a PB.

PG 1448+273. It is a spiral galaxy (HyperLeda and Petrosian et al. 2008). Our fitting gives $n = 4$ and $B/T = 0.35$. Therefore, we classified this object as a CB galaxy.

Mrk 1511. It is classified as a barred spiral galaxy according to HyperLeda and Orban de Xivry et al. (2011). The WFC3/UVIS/F547M image is not saturated, allowing for a more accurate fitting of the central region compared to Kim et al. (2017). Our result suggests a small PB with $B/T = 0.02$ and $n = 1.75$.

PG 1534+580. Although HyperLeda and de Vaucouleurs et al. (1991) both report that this object is an elliptical, the UVIS1/F547M image shows clear faint spiral/disk structures. Kim et al. (2017); Bentz et al. (2009); Orban de Xivry et al. (2011) also suggest that using two host components in the fitting is better. We obtained $B/T = 0.34$, which is consistent with the result in Kim et al. (2017) ($B/T \sim 0.42$).

PG 1535+547. This object has a barred spiral galaxy, however the spiral structures are not bright. By modeling the bar/disk component with a $n = 1$ Sérsic profile, we obtained $B/T = 0.2$ and $n = 0.6$. Therefore, we classified this object as PB galaxy.

Mrk 493. The nuclear region is saturated, and we obtained similar results compared to Kim et al. (2017) and Wang et al. (2014), confirming the presence of a PB in this object.

PG 1613+658. This target is an elliptical galaxy according to HyperLeda and the previous studies (Bentz et al. 2009; Guyon et al. 2006). Following Kim et al. (2017), we fitted the spheroid with the Fourier modes in GALFIT.

PG 1617+175. It is an elliptical galaxy (Guyon et al. 2006). We employed the WFC1/F625W image which has higher SN ratio than that of the PC/F547M image. There is some ring-like structure in the residual image.

PG 1626+554. We used the UVIS1/F475M image in our GALFIT fitting because of its optical central wavelength. The WFC3/F105W image suggests that two components are needed for a good fitting to its host galaxy. We fixed

the structure parameters (e.g., n , R_e) as those derived from the WFC3/F105W image. The resulting $B/T = 0.25$ and $n = 4$ lead us to classify the bulge as a CB.

PG 1700+518. In contrast to Kim et al. (2017), we set the Sérsic index of the bulge as a free parameter, and obtained a single and flat component for the host galaxy. Some structure located at the north side of the nucleus seems weird. We masked this structure in our fitting. Similar to Ho & Kim (2014); Guyon et al. (2006); Bentz et al. (2009), we classified this target as an elliptical galaxy.

3C 382. It is a compact object, and was classified as an elliptical in HyperLeda. Kim et al. (2017) also classified this object as an elliptical galaxy.

3C 390.3. Its compact galaxy makes it challenging to decompose the host components. Our 1D and 2D results suggest that it is an elliptical, which is in agreement with the conclusions in Kim et al. (2017) and Bennert et al. (2010). The F550M total magnitude from our fitting is 15.2, almost the same as the V-band magnitude of 15.3 reported in Smith & Heckman (1989) and Véron-Cetty & Véron (2010).

Zw 229-015. Also known as Z 229-15. HyperLeda reports this target as a barred spiral galaxy. Bentz & Manne-Nicholas (2018) reported $B/T = 0.143$ and $n = 1.1$. We obtained a slightly flatter and fainter bulge ($B/T = 0.09$, $n = 0.77$). Both Bentz & Manne-Nicholas (2018) and our fitting result classified this object as a PB galaxy.

NGC 6814. It is a barred spiral galaxy (HyperLeda and de Vaucouleurs et al. 1991). Our fitting reports a PB with $n = 1.5$ and $B/T = 0.03$.

Mrk 509. As discussed in Kim et al. (2017), the presence of non-elliptical features suggests that Mrk 509 may not be an elliptical galaxy. Our fitting with two host components resulted in a B/T of 0.58 and n of 4, indicating that the bulge is dominated (consistent with the ground-based observation in Ho & Kim 2014).

PG 2130+099. This is a spiral galaxy (Guyon et al. 2006; de Vaucouleurs et al. 1991). We employed the WF2/F555W image which has a much higher SN ratio than the HRC/F550M image, though the PSF is saturated. We fixed the PSF flux as 14.5 mag derived from the HRC/F550M (unsaturated), since F555W and F550M image have the similar central wavelengths. We obtained $B/T = 0.31$ and $n = 0.43$, which are consistent with the results in Kim et al. (2017) and Bentz et al. (2009). Therefore, we classified this object as a PB galaxy.

NGC 7469. The inner spiral/ring structures were masked out during the fitting, resulting in a lower $B/T = 0.18$ and larger n of approximately 1.7 for the bulge component, in comparison with the results in Bentz et al. (2009) ($B/T \sim 0.7$, $n \sim 1.3$). Both the parameters and structures suggest the presence of a PB in this object.

B. COMPARISON OF GALFIT RESULTS WITH PREVIOUS WORKS

Here we show some comparisons between our GALFIT results and those from the previous works in Bentz et al. (2009) and Kim et al. (2017). The comparisons of the magnitudes of the PSF and bulge components are provided in Figure 11. In general, our fitting results are consistent with those from Bentz et al. (2009) and Kim et al. (2017). Most of the points are located around the diagonal lines, indicating the reliability of our GALFIT fitting and the host decomposition. Some outliers are due to the PSF saturation or different images used in the fitting.

C. CORRELATIONS ANALYSIS OF THE VIRIAL FACTORS BASED ON TOTAL SAMPLE

For comparison, we plot the correlations between the deviations of the total-sample virial factors and the spectral properties of in Figures 12-15.

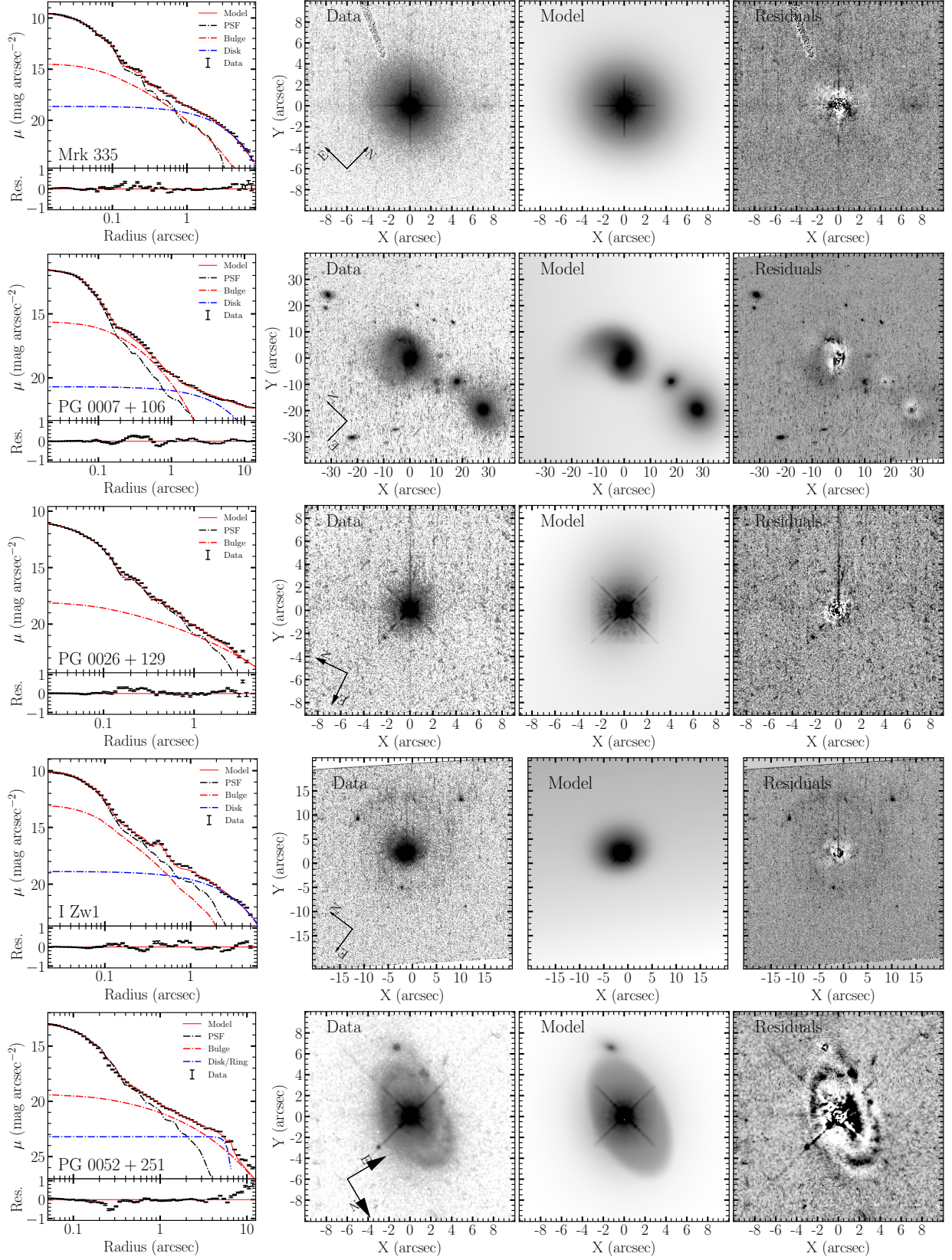


Figure 1. GALFIT fitting results. From left to right, the first columns are the one-dimensional surface brightness of their host components. The points with error bars are the *HST* data, the red solid lines are the best-fit models, the dash-dotted lines with different colors are the surface-brightness profiles of the PSFs, bulges, bars, and etc. The gray regions are masked out in the fitting. The second columns show the *HST* images. The third columns are the best-fit models. The last columns are the residual images. The names of the objects are marked in the first columns.

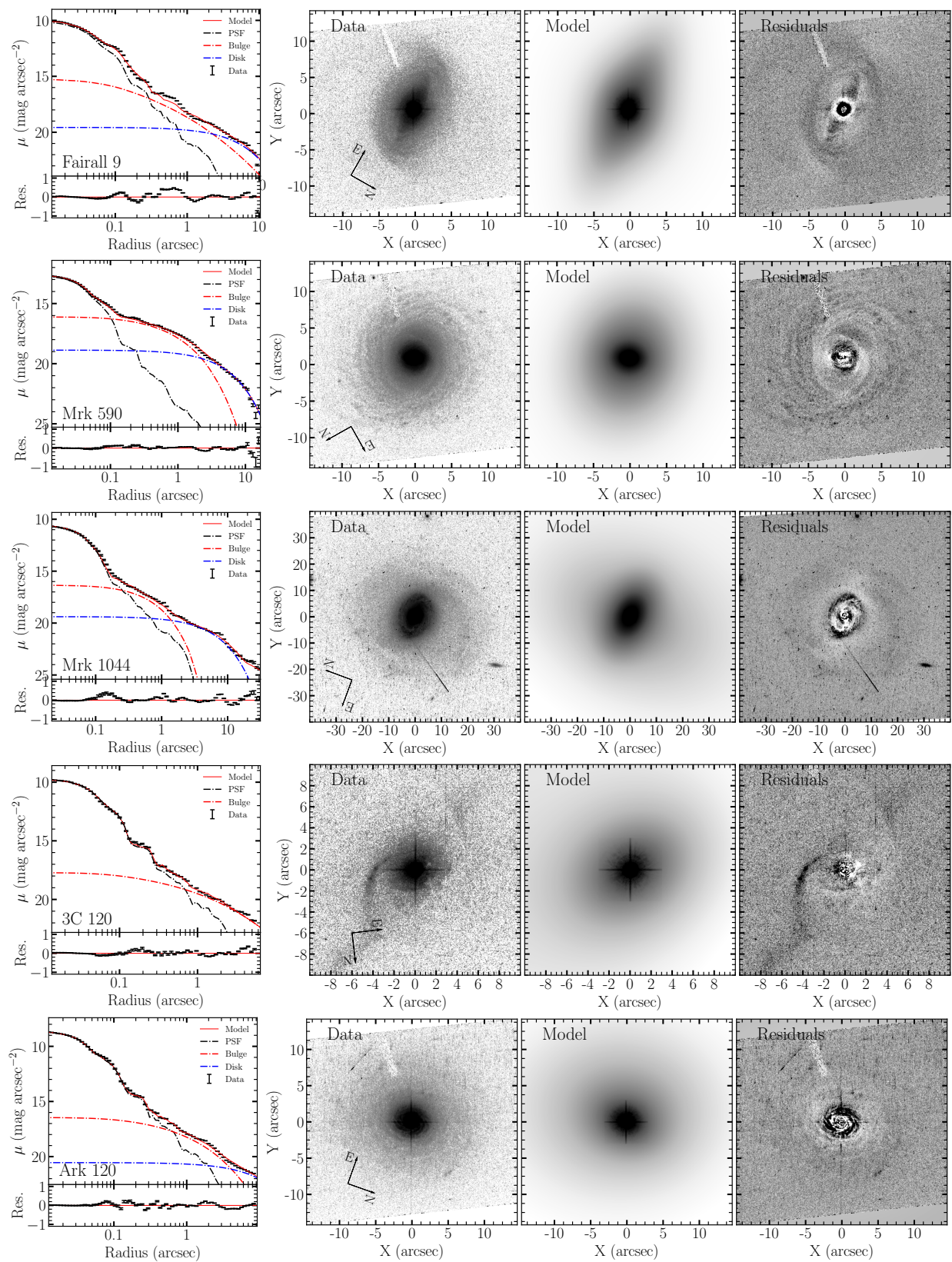


Figure 1. (Continued.)

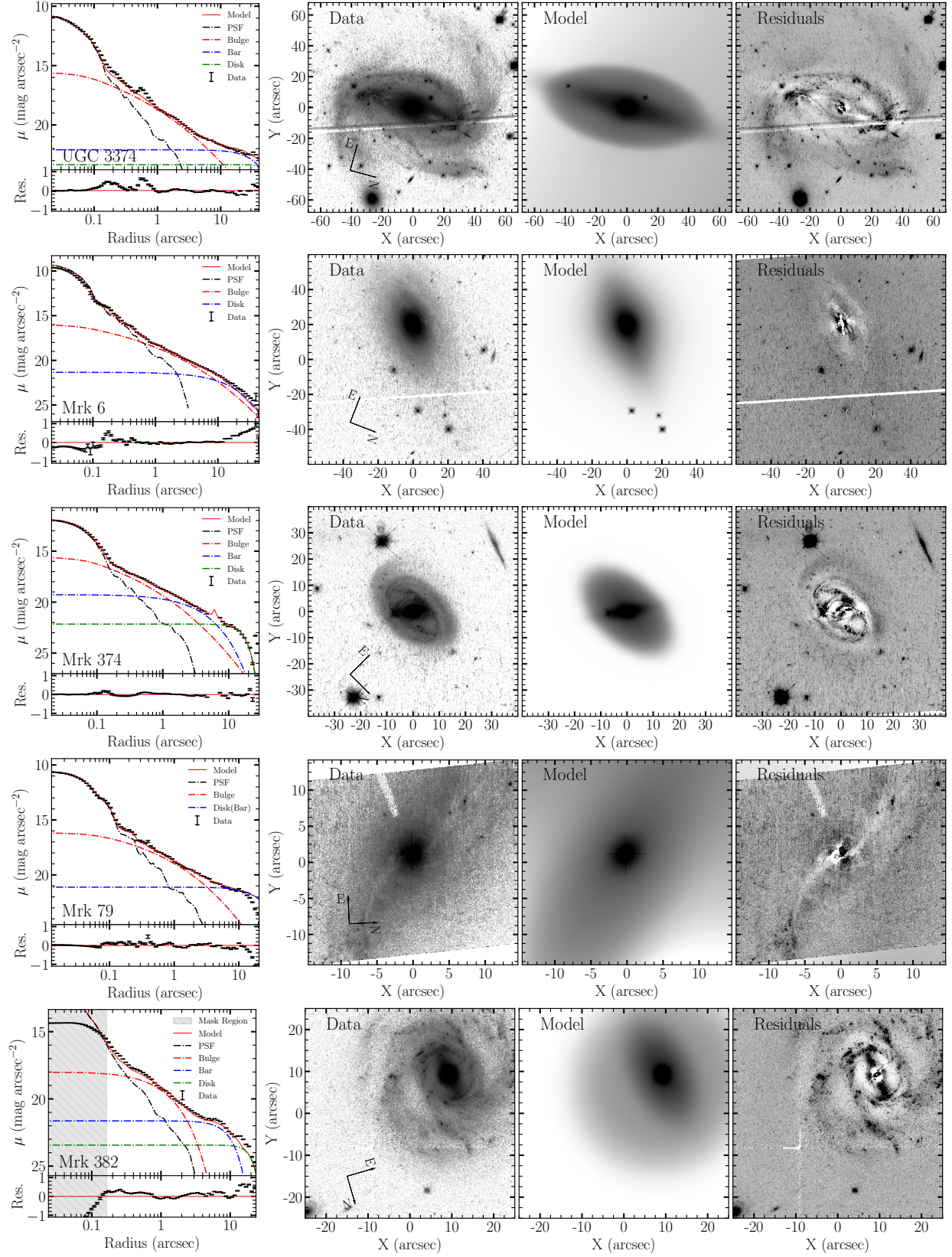


Figure 1. (Continued.)

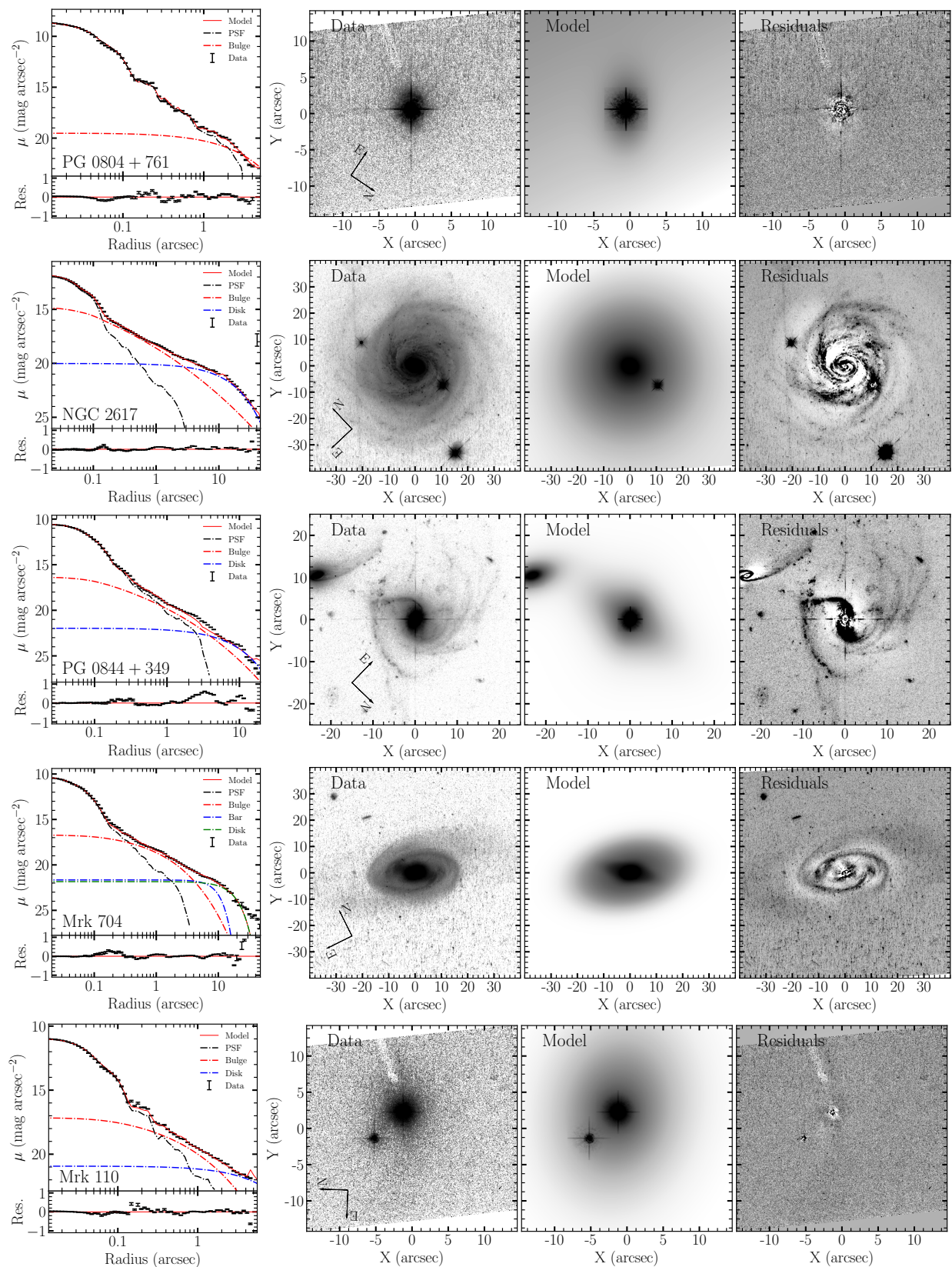


Figure 1. (Continued.)

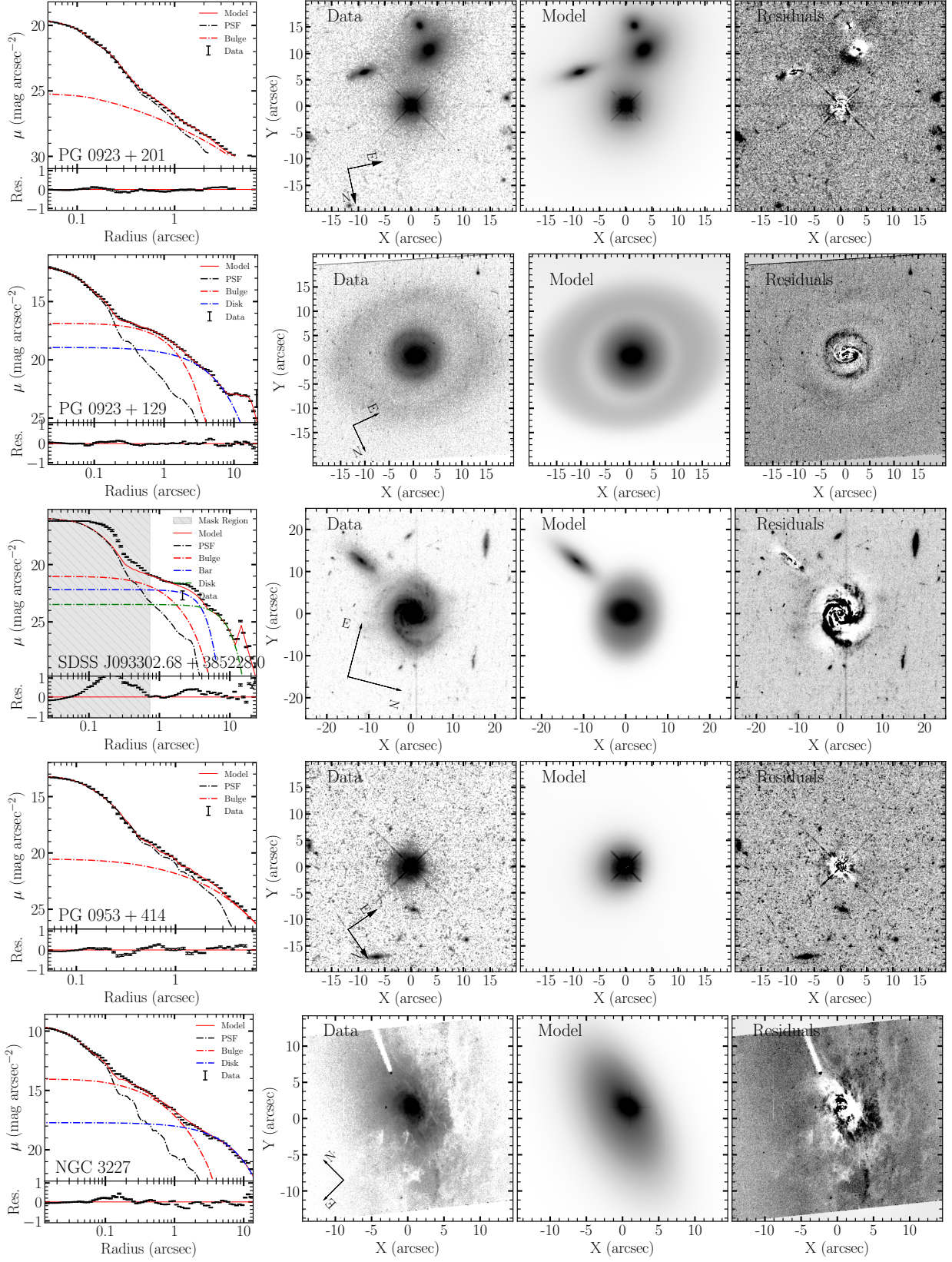


Figure 1. (Continued.)

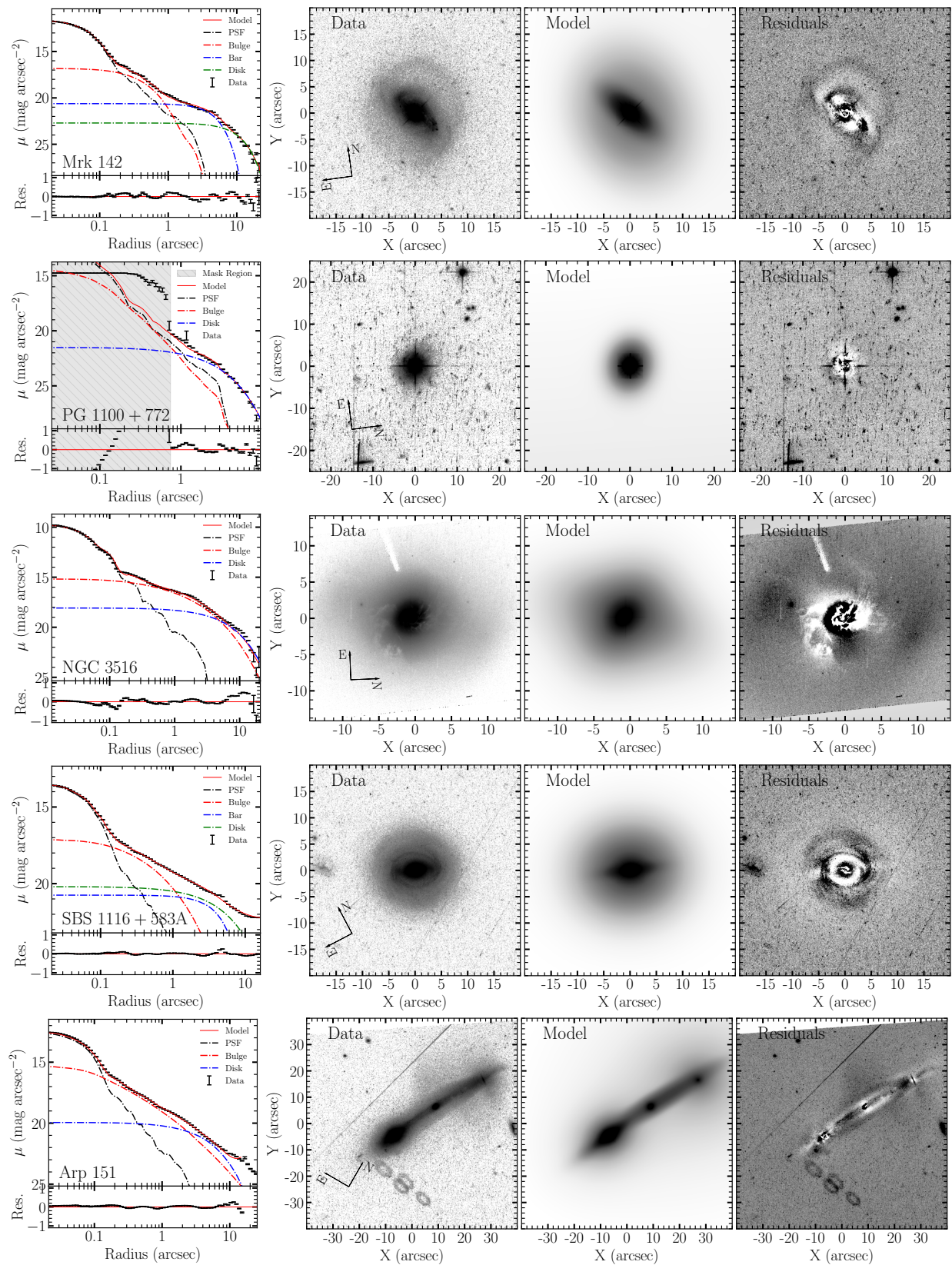


Figure 1. (Continued.)

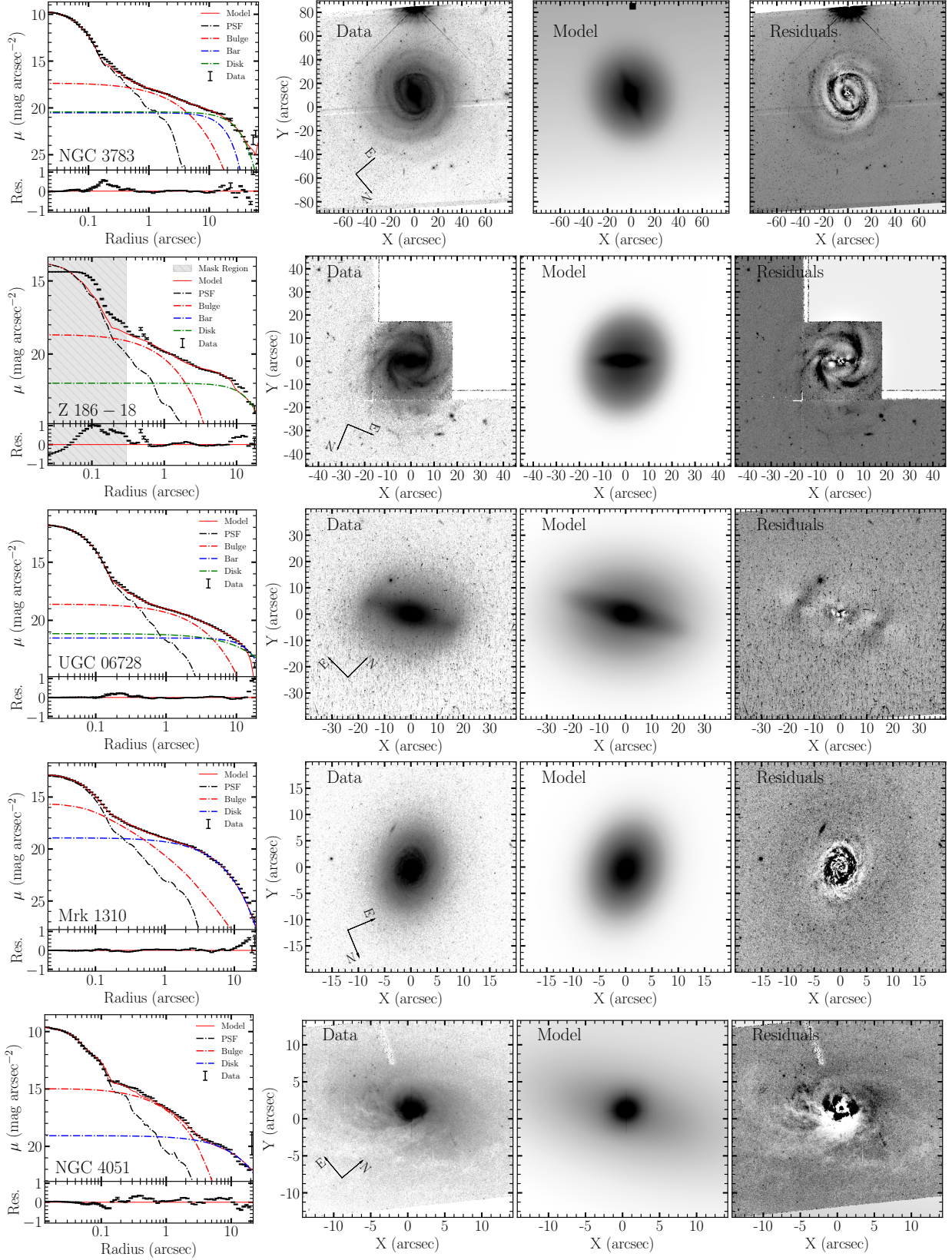


Figure 1. (Continued.)

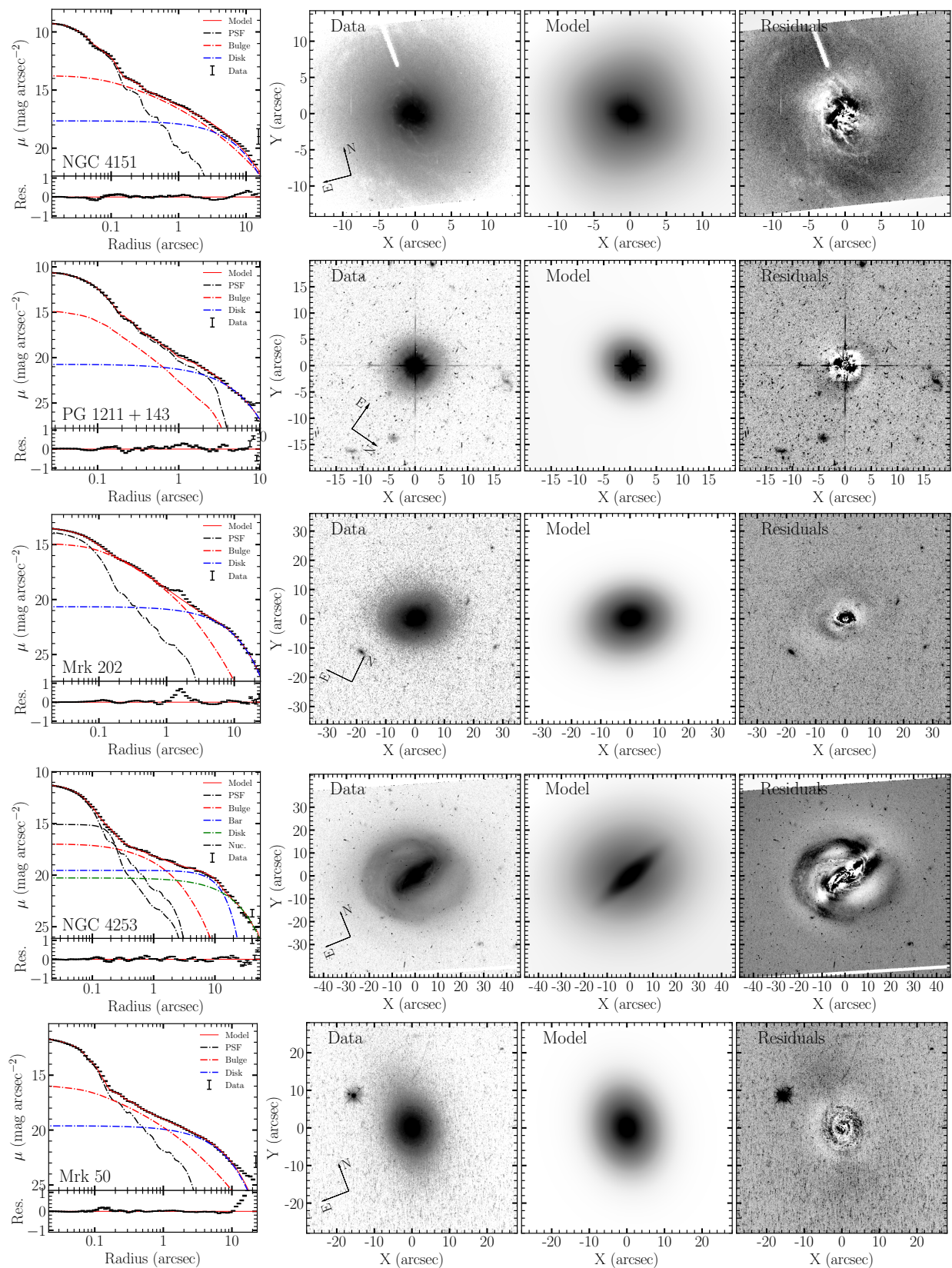


Figure 1. (Continued.)

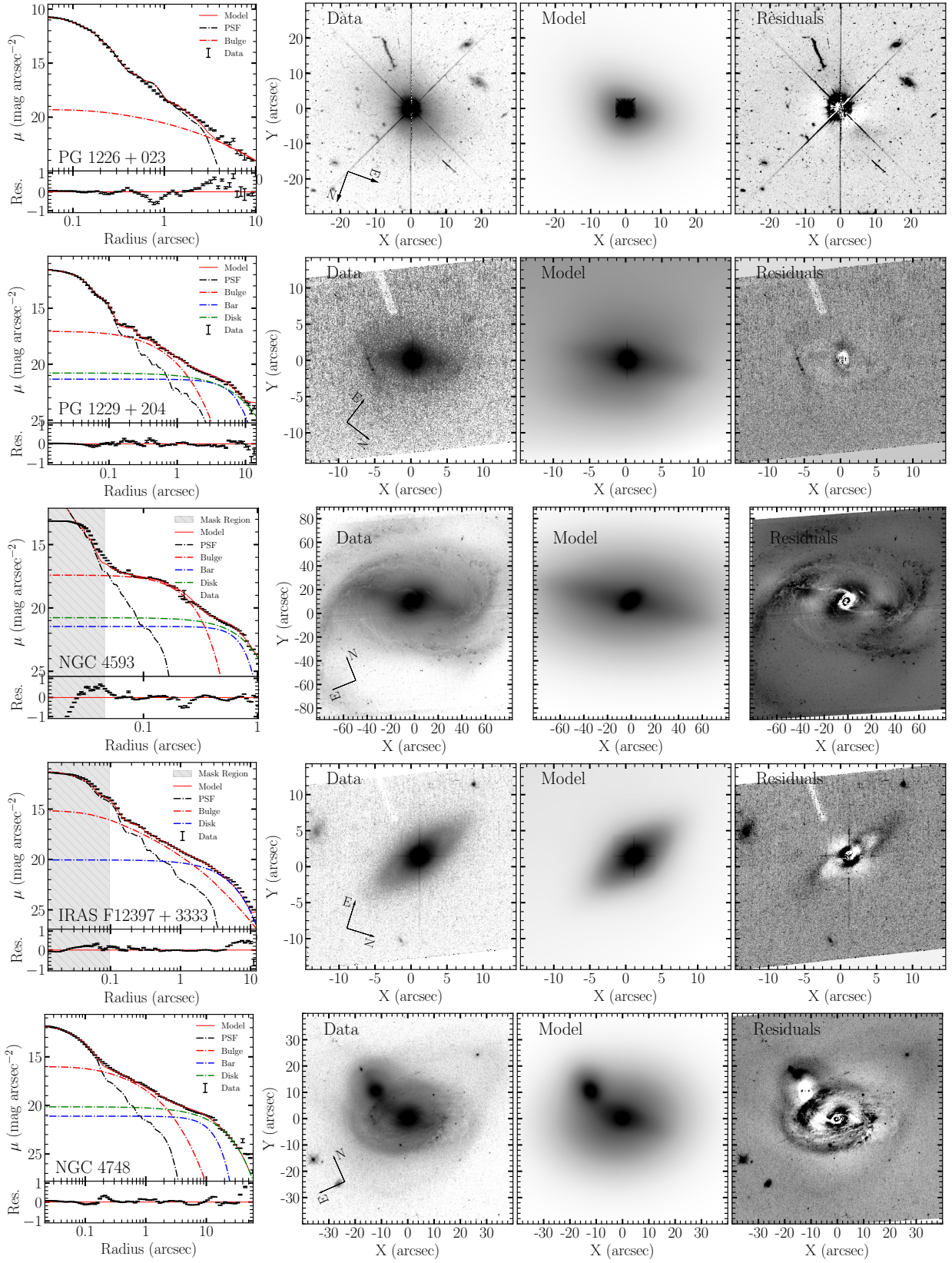


Figure 1. (Continued.)

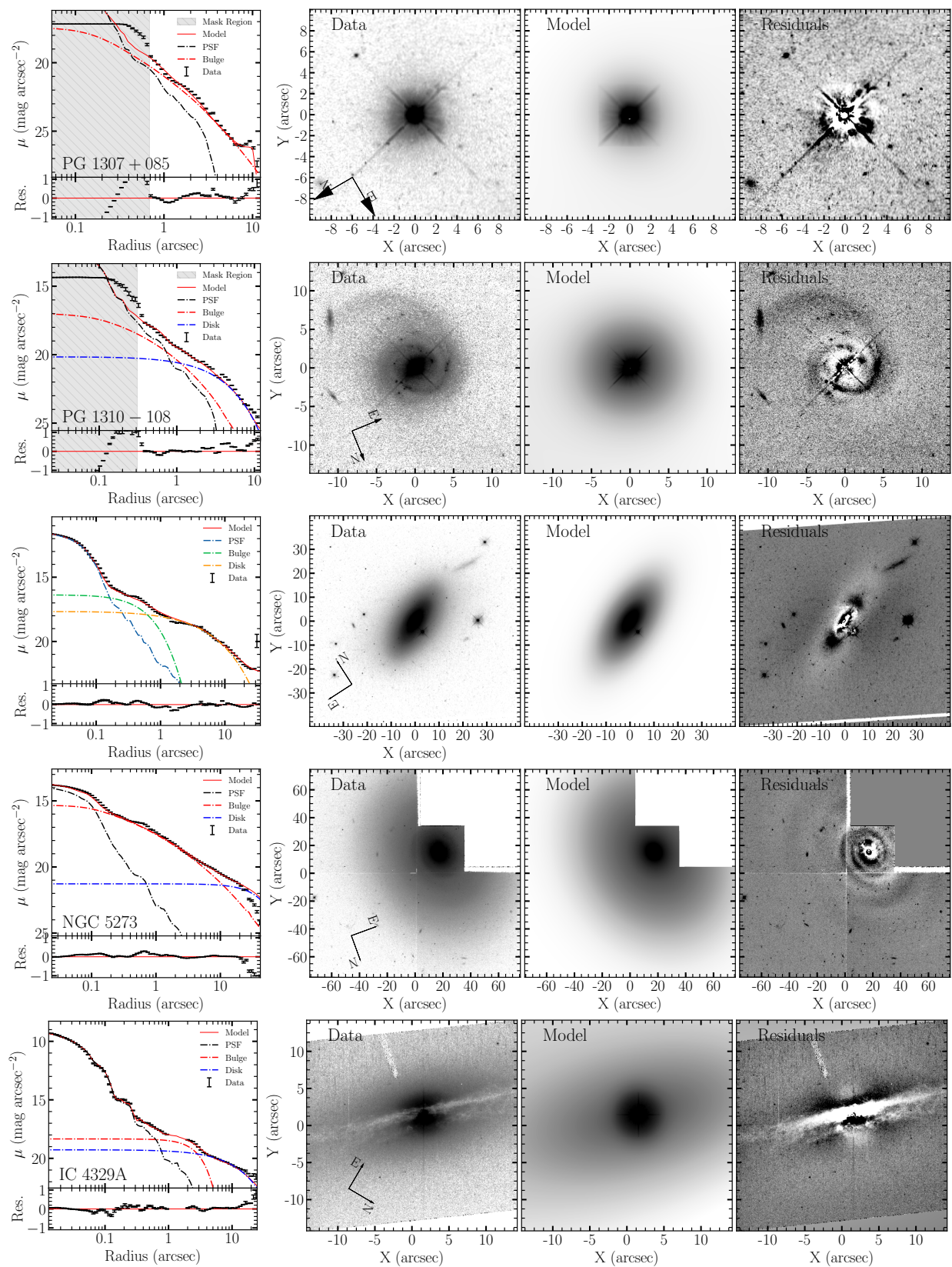


Figure 1. (Continued.)

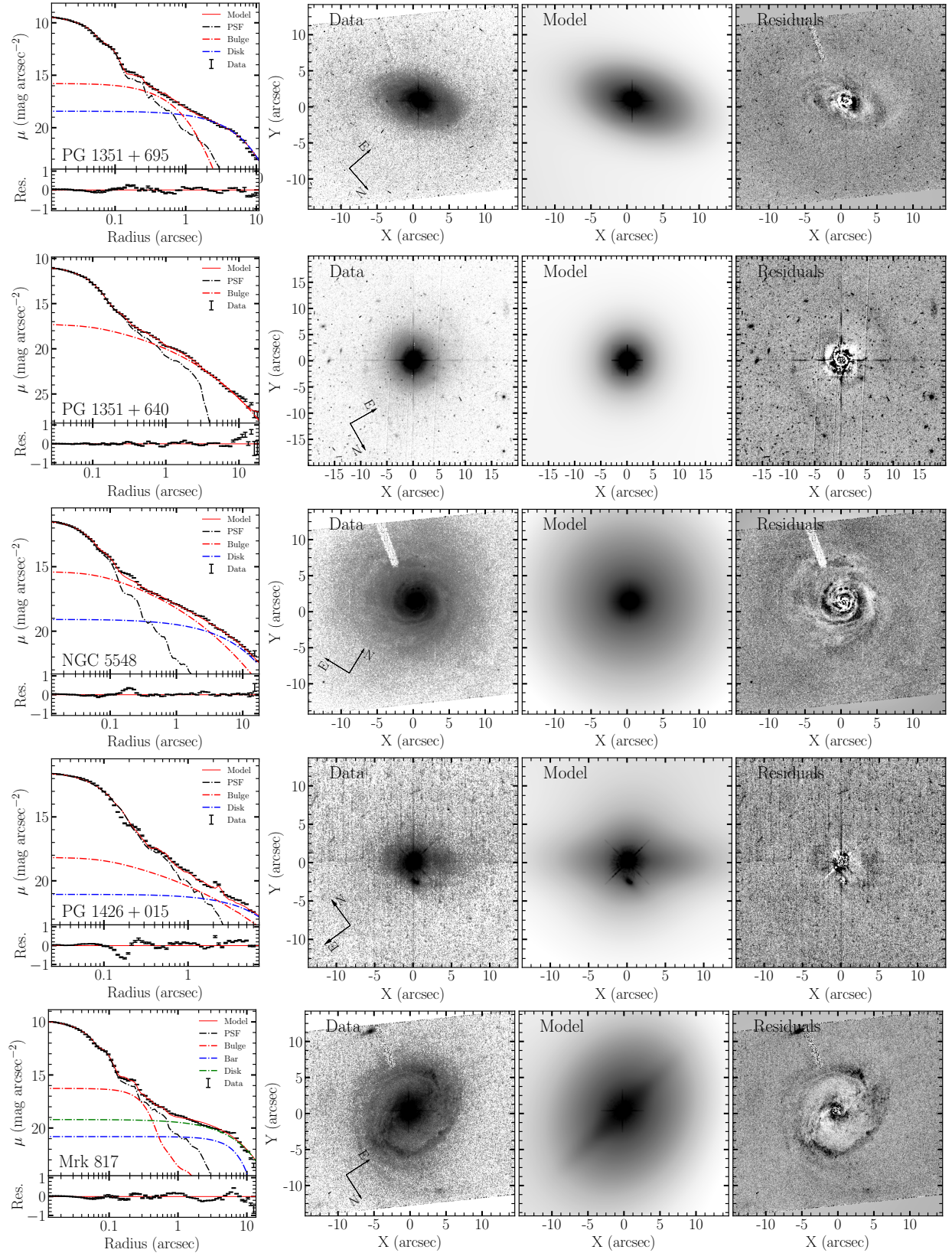


Figure 1. (Continued.)

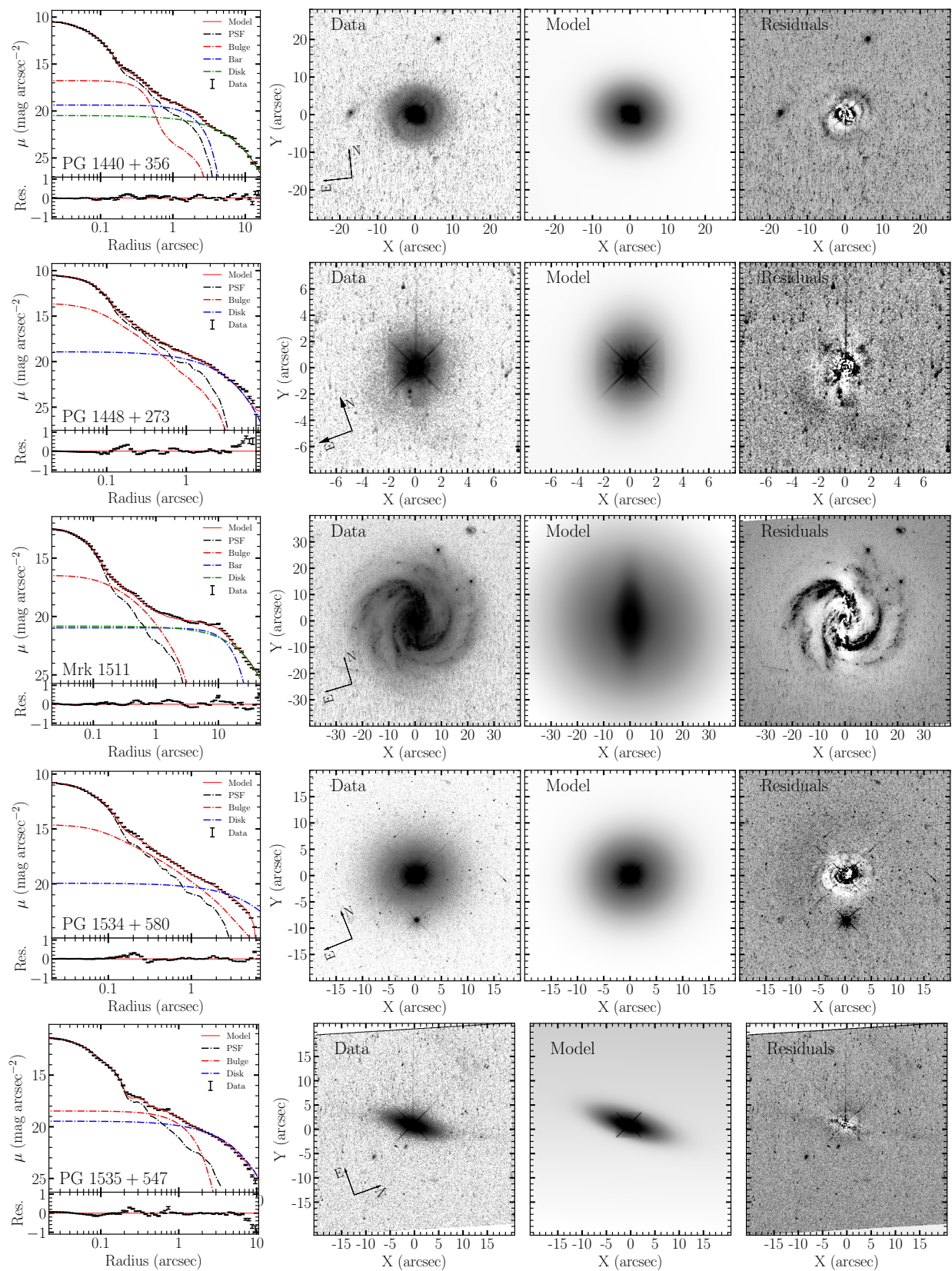


Figure 1. (Continued.)

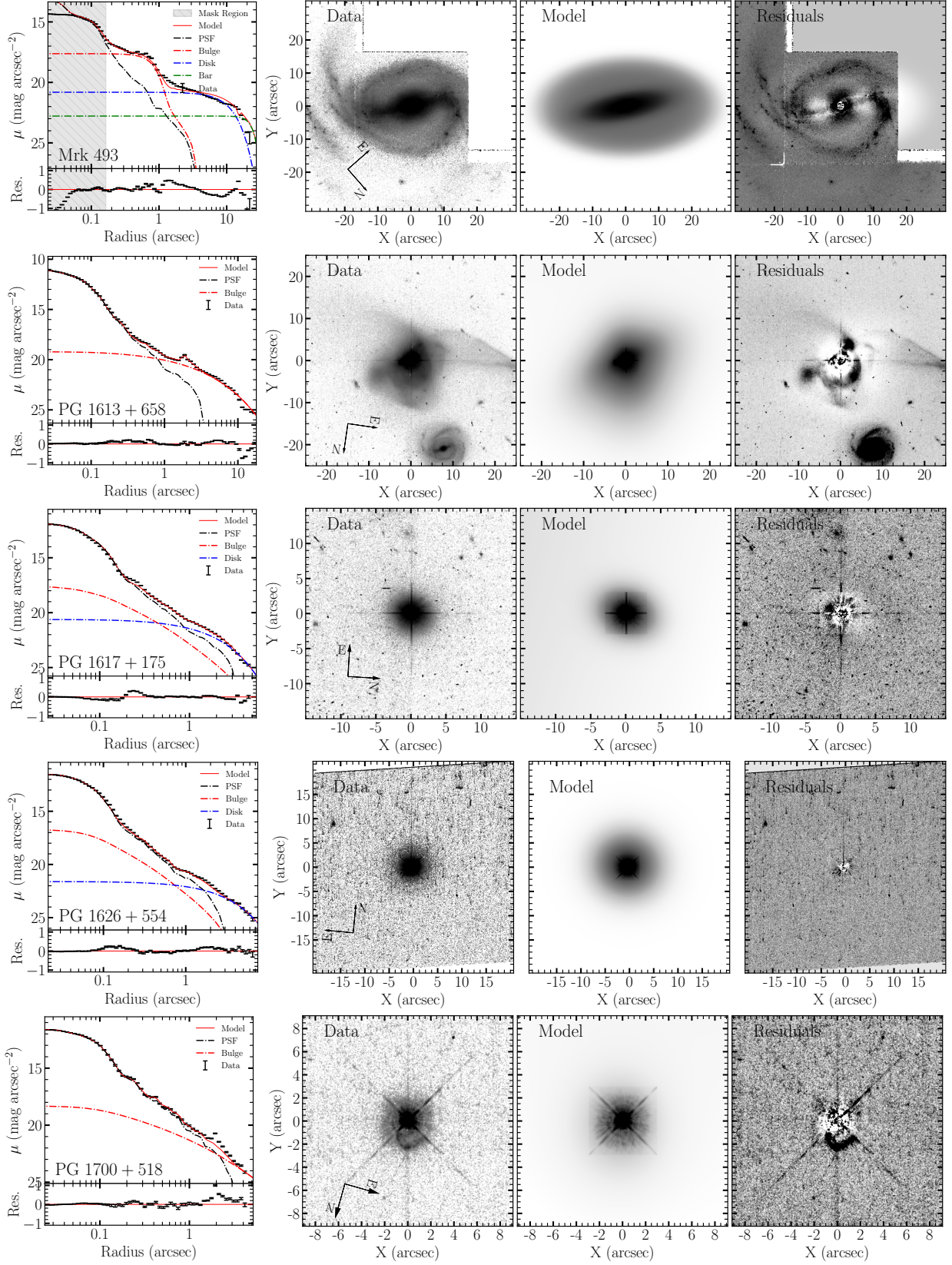


Figure 1. (Continued.)

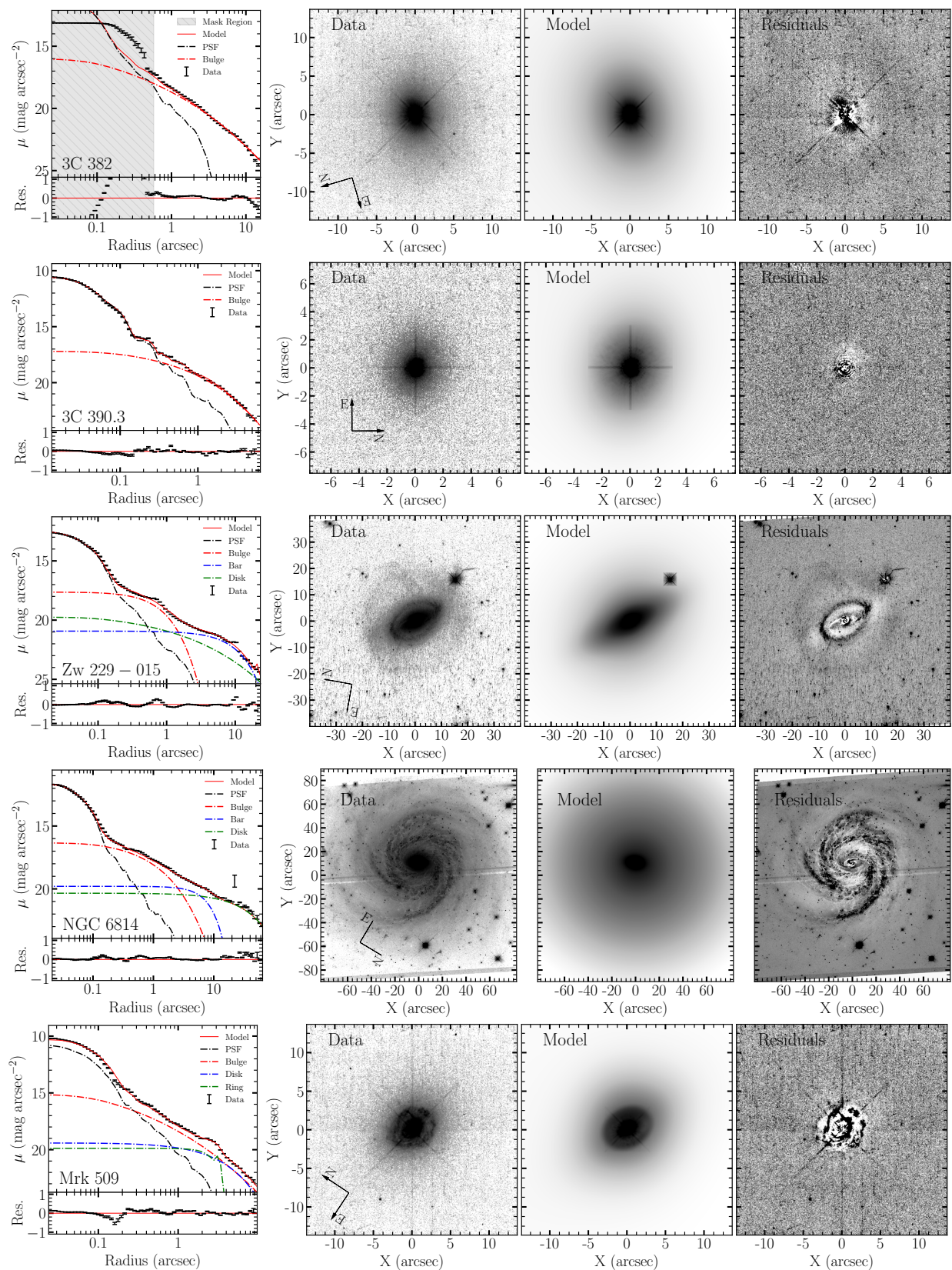


Figure 1. (Continued.)

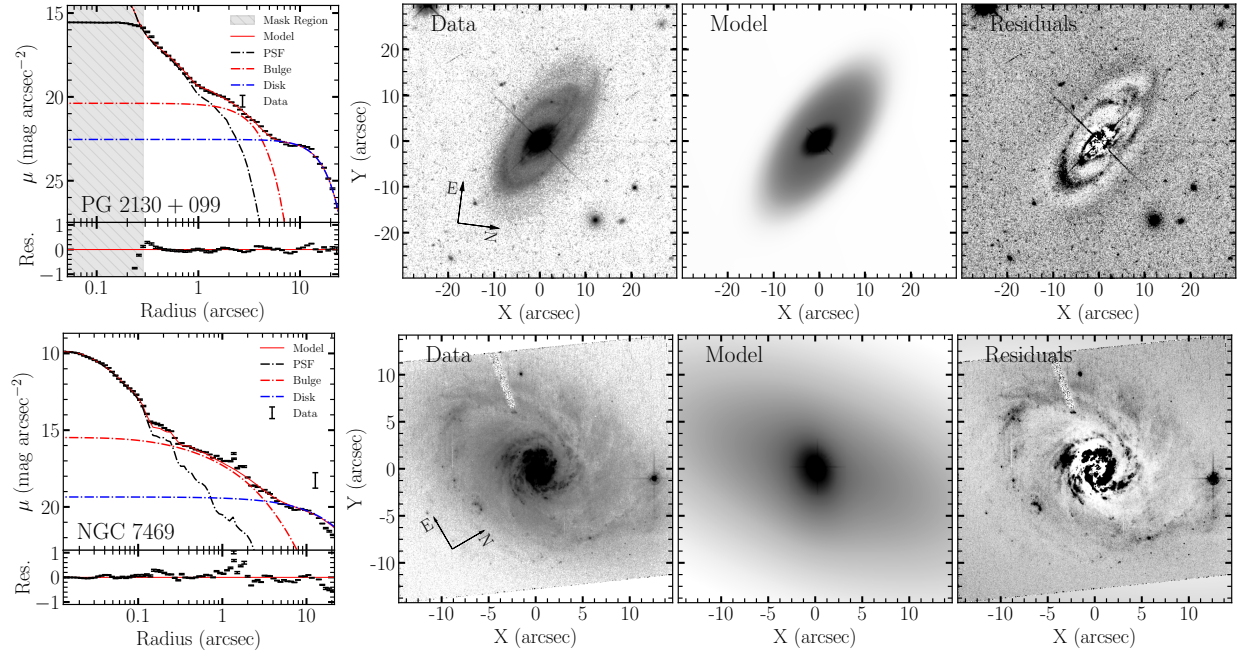


Figure 1. (Continued.)

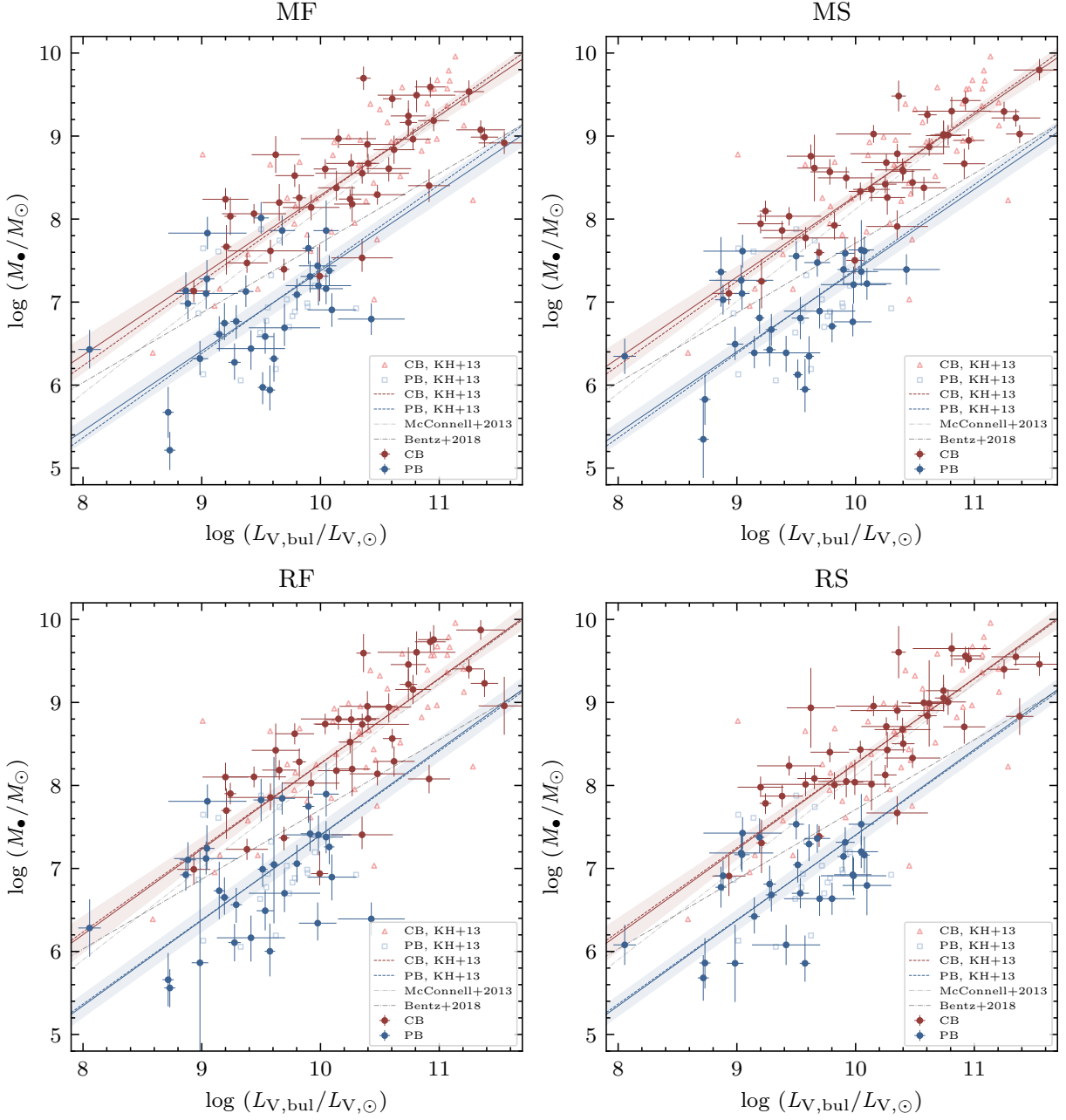


Figure 2. Calibration of virial factors based on the $M_{\bullet} - L_{V,\text{bul}}$ relation. The four panels are the calibrations of f_{MF} , f_{MS} , f_{RF} , and f_{RS} , respectively. The red open triangles and blue open squares are the quiescent galaxies from [Kormendy & Ho \(2013\)](#), while the red and blue circles with error bars are the RM AGNs with CB and PB host galaxies, respectively. The red and blue solid lines and the regions are the results and confidence bands of the joint fitting (Approach I, see Section 3.1). The dashed and dash-dotted lines are the $M_{\bullet} - L_{V,\text{bul}}$ relationships from previous works ([Kormendy & Ho 2013](#); [McConnell & Ma 2013](#); [Bentz & Manne-Nicholas 2018](#)).

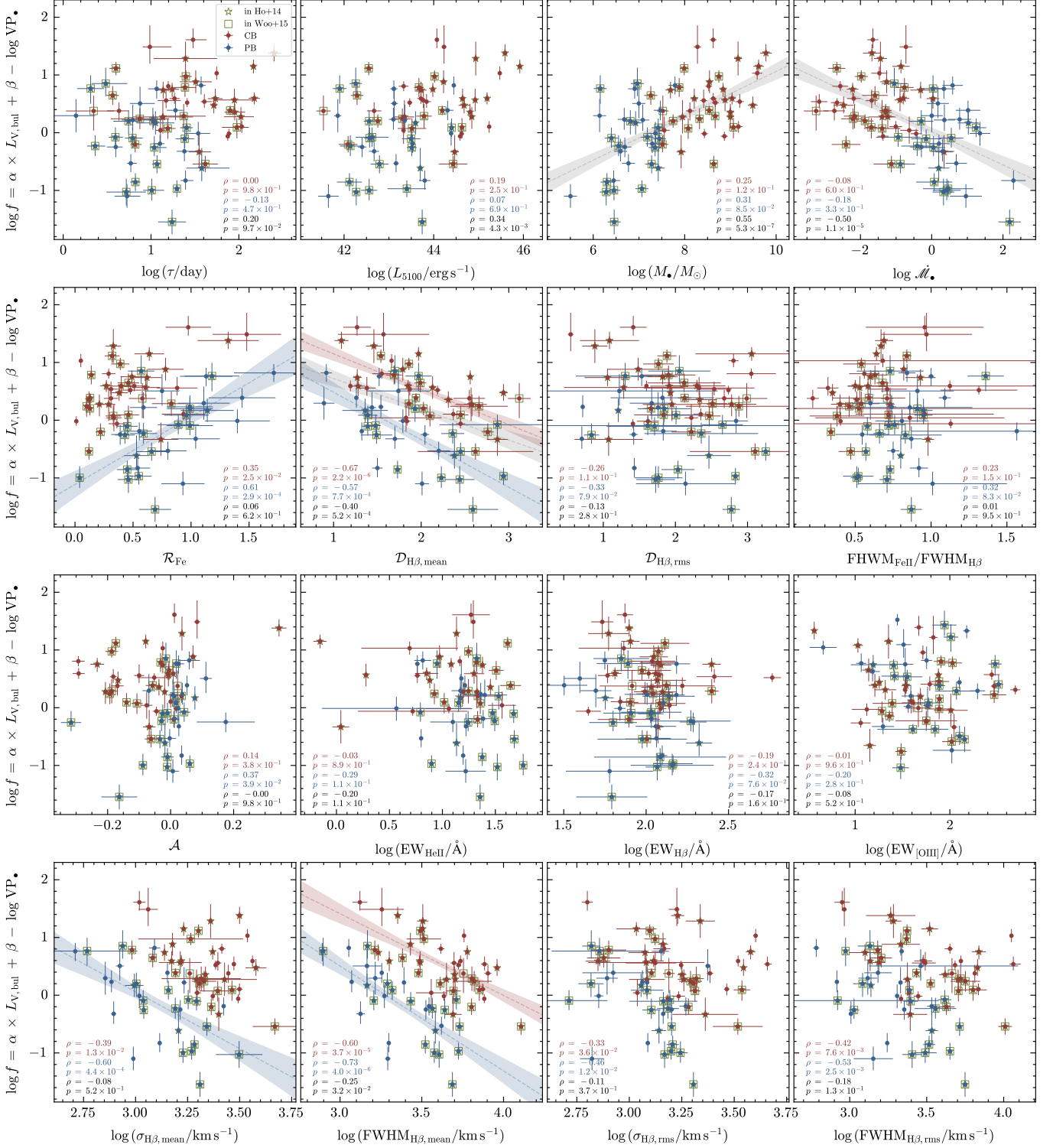


Figure 3. The correlations between f_{MF} and the spectral properties. The CB and PB objects are the red and blue circles, respectively. Spearman's rank correlation coefficients (ρ) and the null probabilities (p) are provided in each panel (red for CBs, blue for PBs, and black for the total sample). The linear regressions and the corresponding confidence bands of the significant correlations with $p < 0.001$ are shown as red (CB), blue (PB), and gray (total) dashed lines and color regions. The circles overlapped with green squares and stars are the same objects as in Woo et al. (2015) and Ho & Kim (2014).

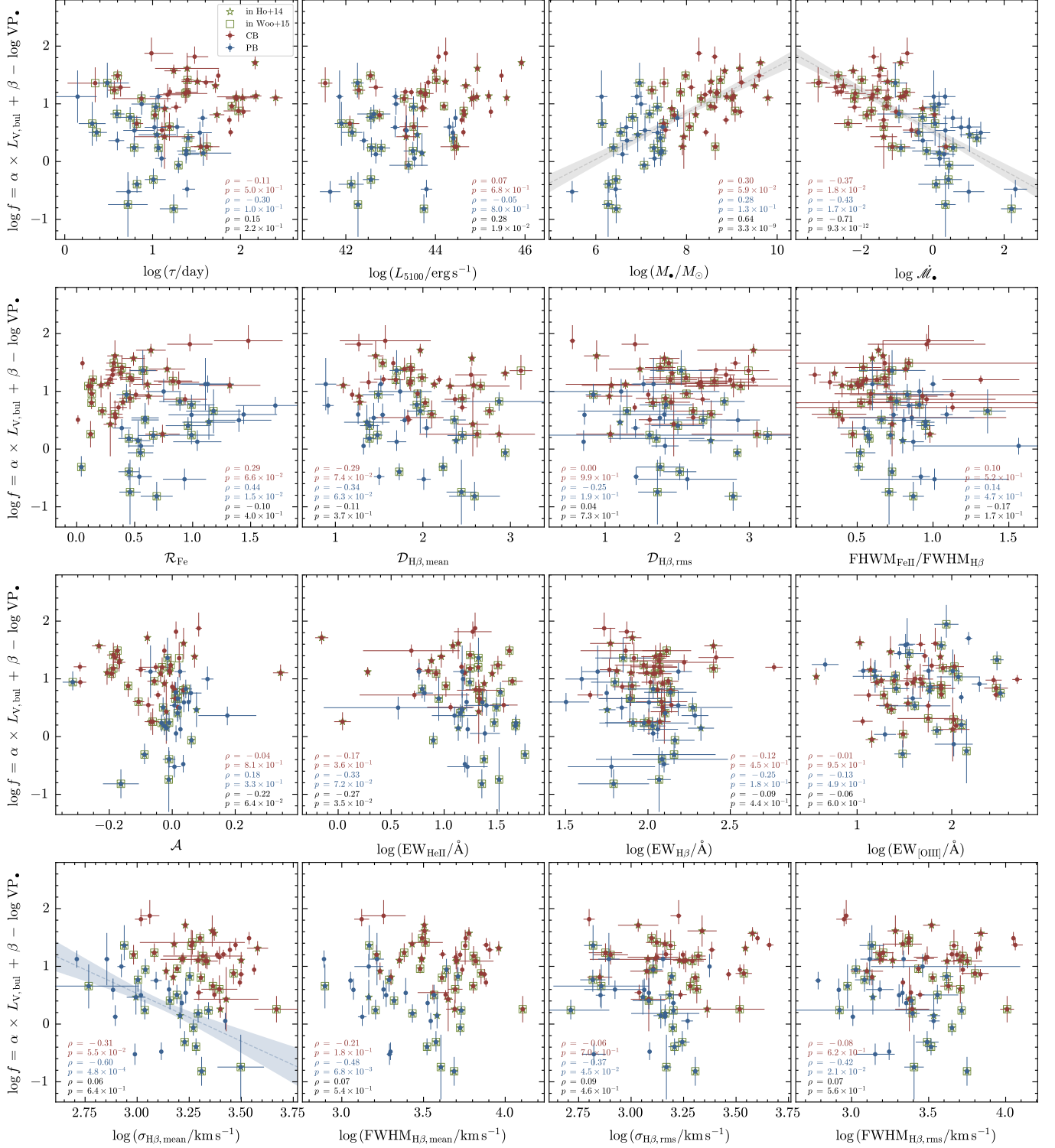


Figure 4. The correlations between f_{MS} and the spectral properties. The meanings of the symbols, lines, and regions are the same as in Figure 3.

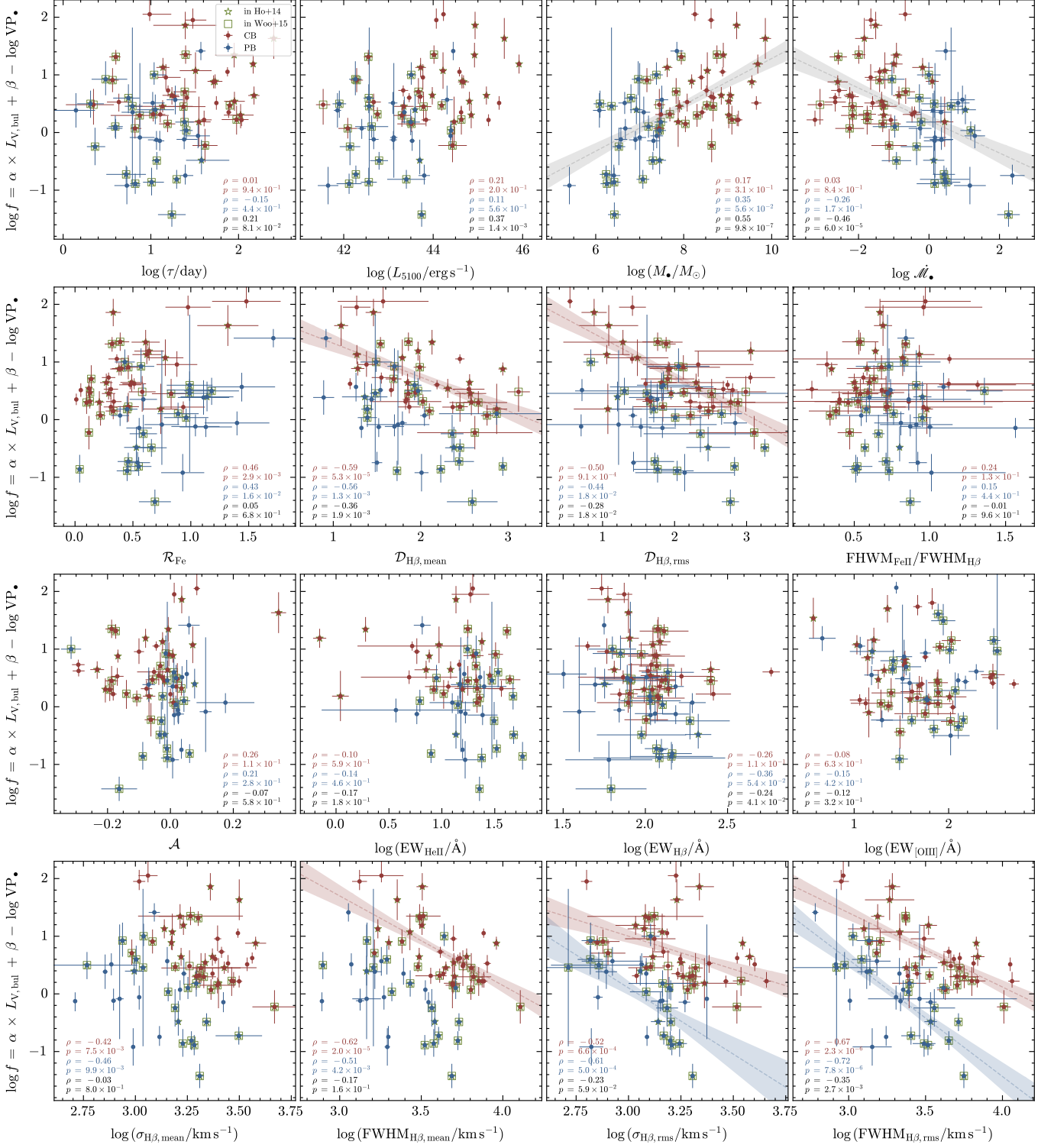


Figure 5. The correlations between f_{RF} and the spectral properties. The meanings of the symbols, lines, and regions are the same as in Figure 3.

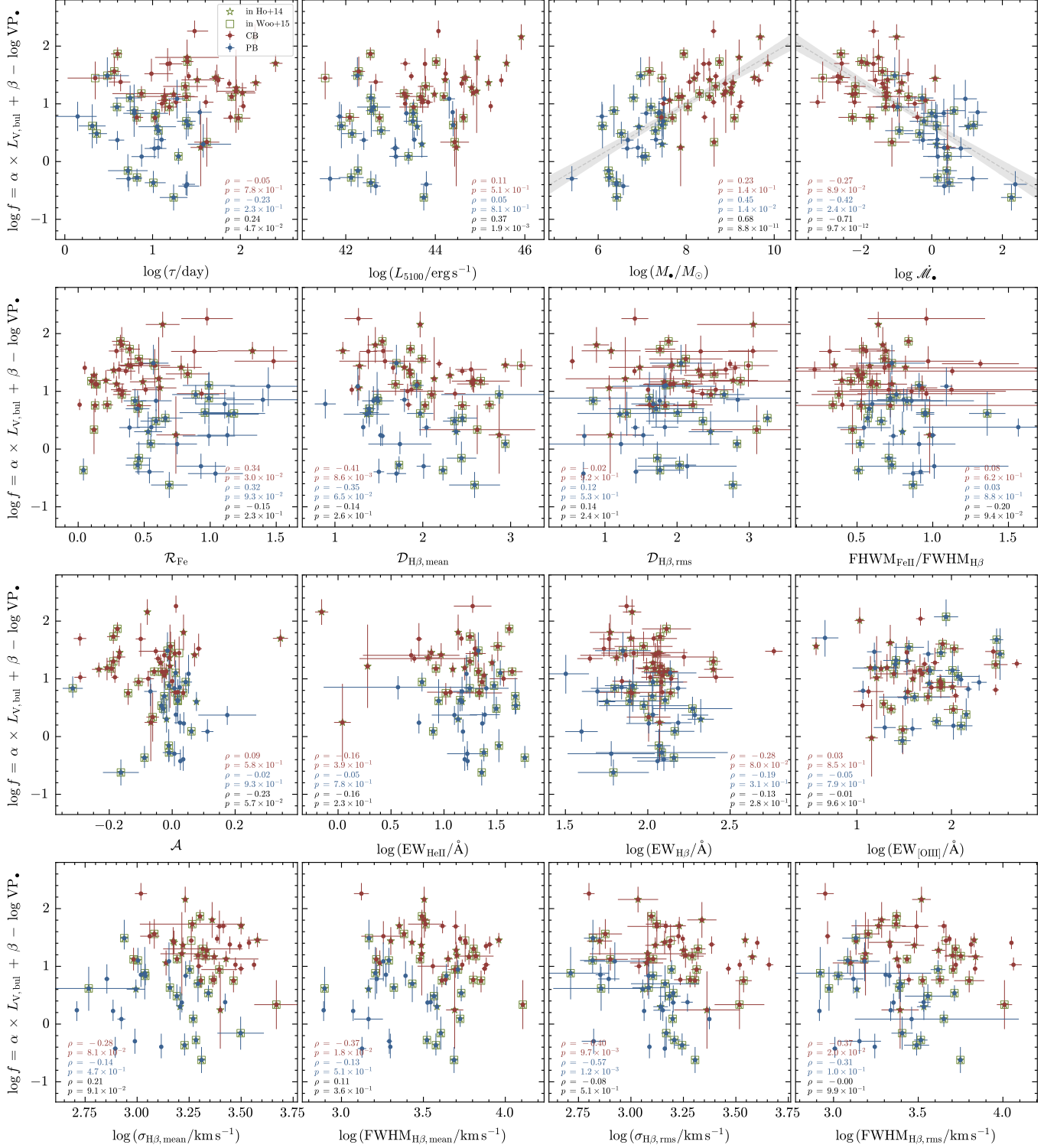


Figure 6. The correlations between f_{RS} and the spectral properties. The meanings of the symbols, lines, and regions are the same as in Figure 3.

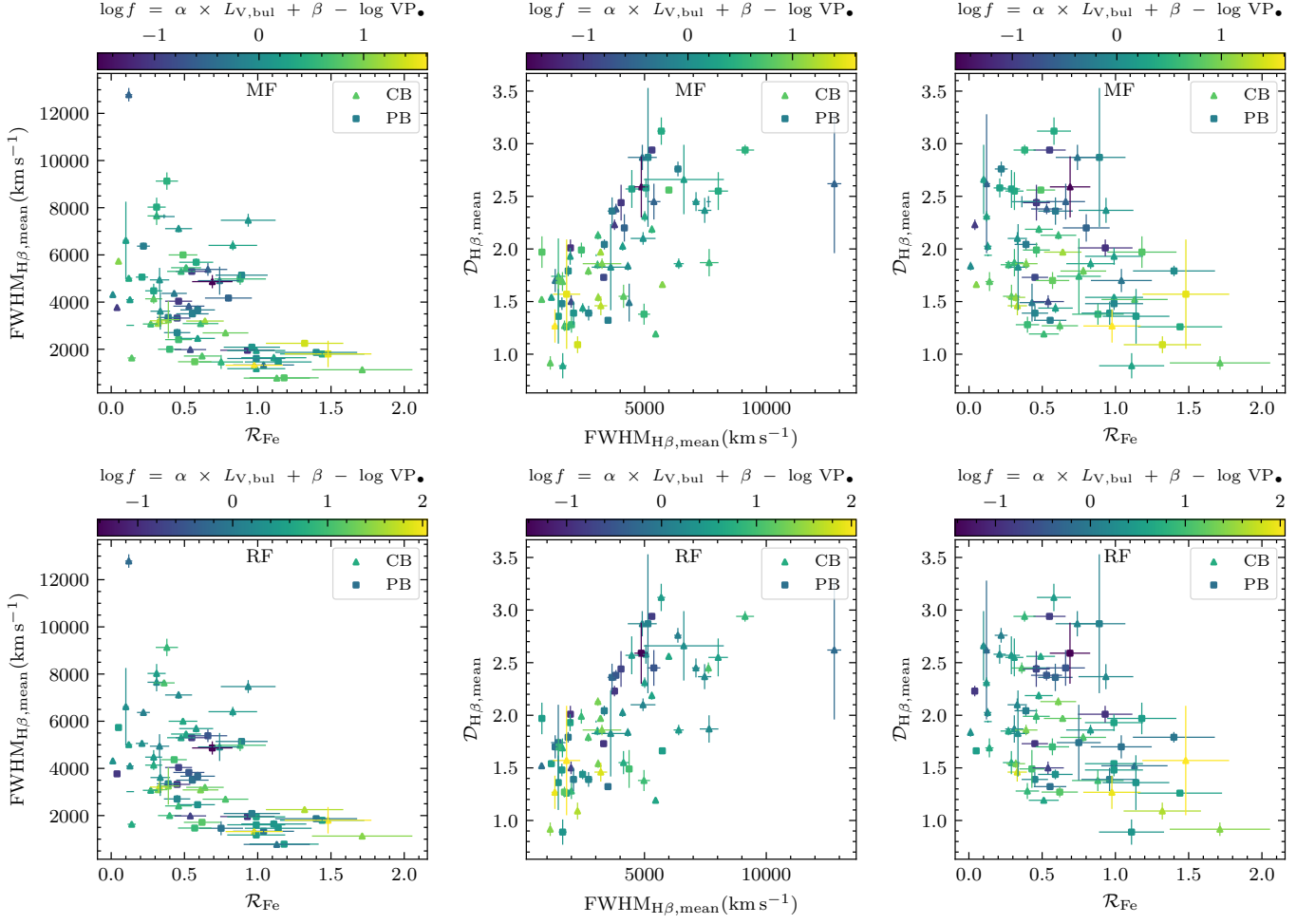


Figure 7. Pairwise correlations between $\text{FWHM}_{\text{H}\beta,\text{mean}}$, \mathcal{R}_{Fe} and $\mathcal{D}_{\text{H}\beta,\text{mean}}$, color-coded by the virial factors (the upper panels for f_{MF} and the lower ones for f_{RF}). The triangles and squares are the CB and PB objects, respectively.

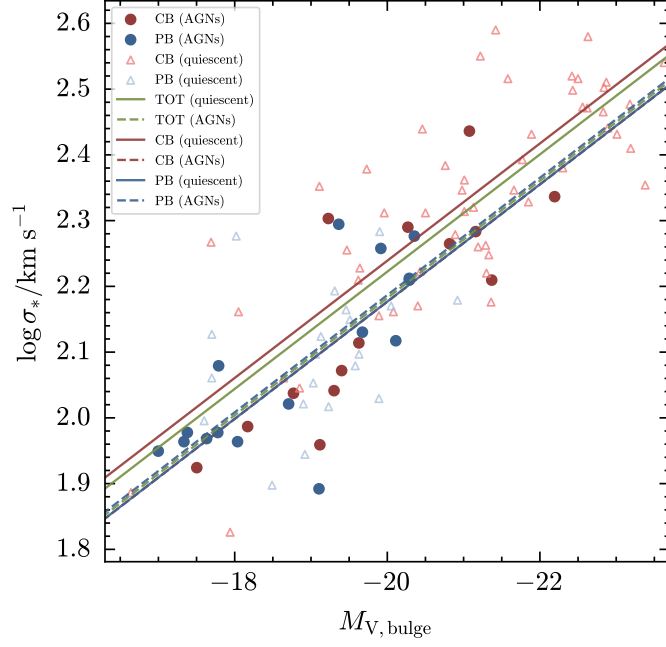


Figure 8. Comparison between the Faber-Jackson relationships of the AGNs and quiescent galaxies. The open triangles are the quiescent galaxies, and the circles are the AGNs. $M_{V,\text{bul}}$ is the absolute V-band magnitude of the bulge. The solid and dashed lines are the linear regressions of the quiescent galaxies and AGNs with CB (red) and PB (blue). Those of the total sample are marked in green. The offsets between the AGNs and quiescent galaxies are obvious for the CB and total samples.

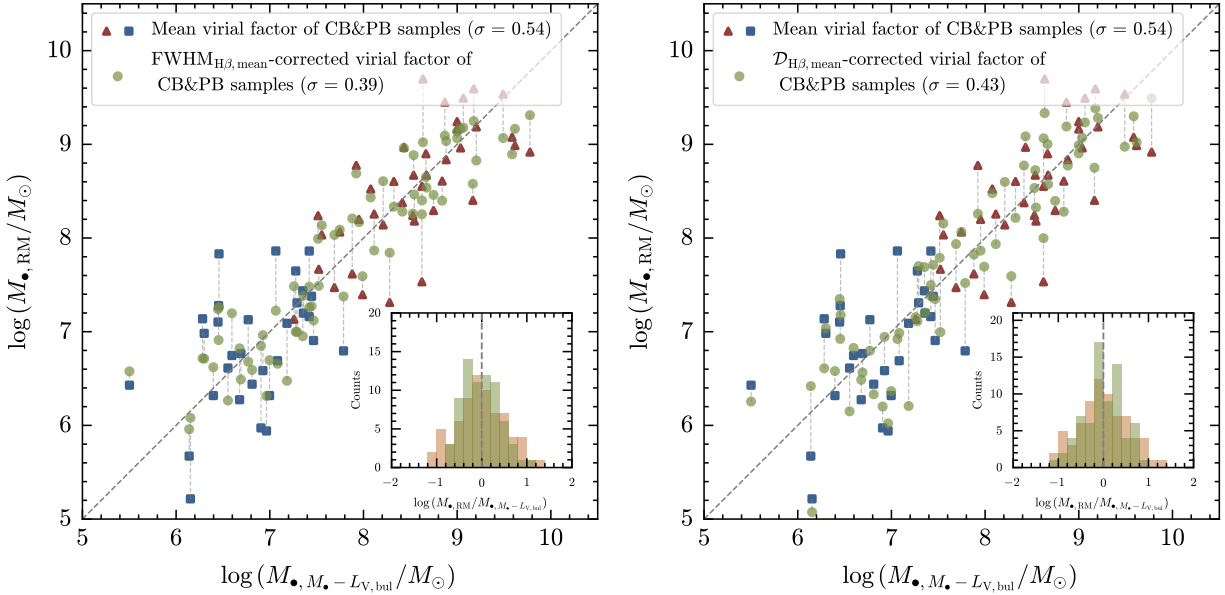


Figure 9. Comparisons between the SMBH masses derived from the $M_{\bullet} - L_{V,\text{bul}}$ relations ($M_{\bullet, M_{\bullet}-L_{V,\text{bul}}}$) and from the RM with the calibrated virial factors ($M_{\bullet, \text{RM}}$). The red triangles (CB) and blue squares (PB) are the RM masses derived from the average virial factors from Table 5, and the green circles are the masses obtained by using the $\text{FWHM}_{\text{H}\beta, \text{mean}}$ - or $\mathcal{D}_{\text{H}\beta, \text{mean}}$ -corrected virial factors. The embedded panel is the distributions of $\log M_{\bullet, \text{RM}}/M_{\bullet, M_{\bullet}-L_{V,\text{bul}}}$ (green for $\text{FWHM}_{\text{H}\beta, \text{mean}}$ - or $\mathcal{D}_{\text{H}\beta, \text{mean}}$ -corrected virial factors, and orange for the average virial factors). Here we only show the MF case as an example. It is clear that the circles from the corrected virial factors show significantly smaller scatters. The σ in the panels denote the standard deviations of $\log(M_{\bullet, \text{RM}}/M_{\bullet, M_{\bullet}-L_{V,\text{bul}}})$.

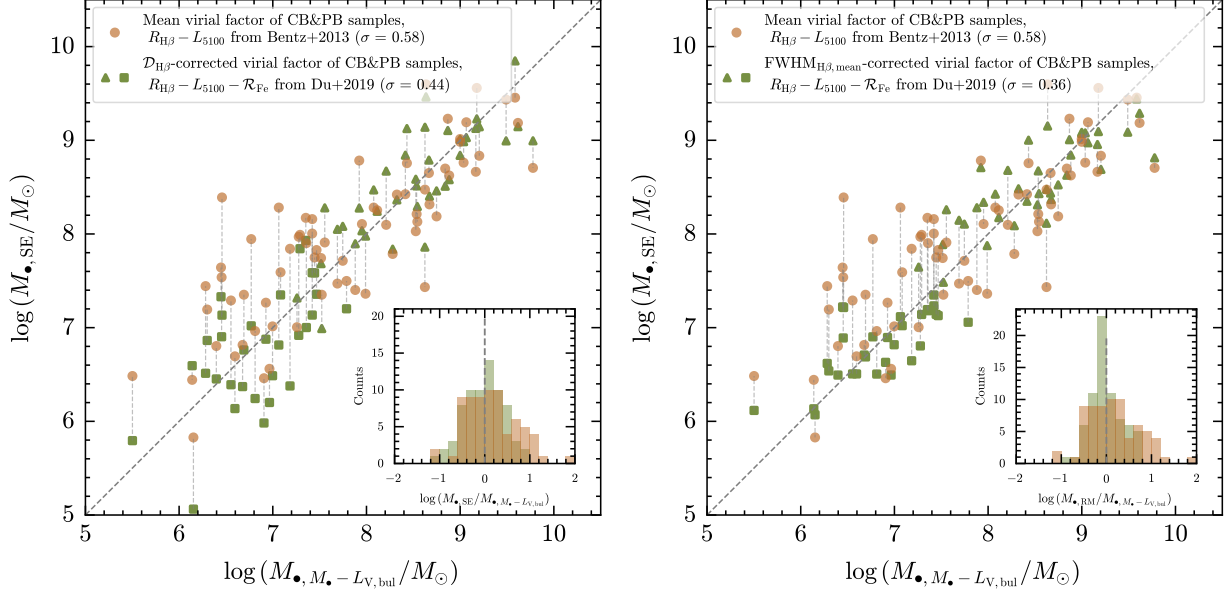


Figure 10. Comparisons between the $M_{\bullet, M_{\star} - L_{V, bul}}$, the SMBH masses from the new single-epoch estimators, and those from the traditional single-epoch estimator. The orange circles are the single-epoch masses ($M_{\bullet, SE}$) from the traditional estimator (the average virial factor and the $R_{H\beta} - L_{5100}$ relation in Bentz et al. 2013), and the green triangles (CB)/ squares (PB) are the those from the new estimators in Section 4.3. The embedded panel is the distributions of $\log M_{\bullet, SE}/M_{\bullet, M_{\star} - L_{V, bul}}$. The σ in the panels denote the standard deviations of $\log(M_{\bullet, SE}/M_{\bullet, M_{\star} - L_{V, bul}})$.

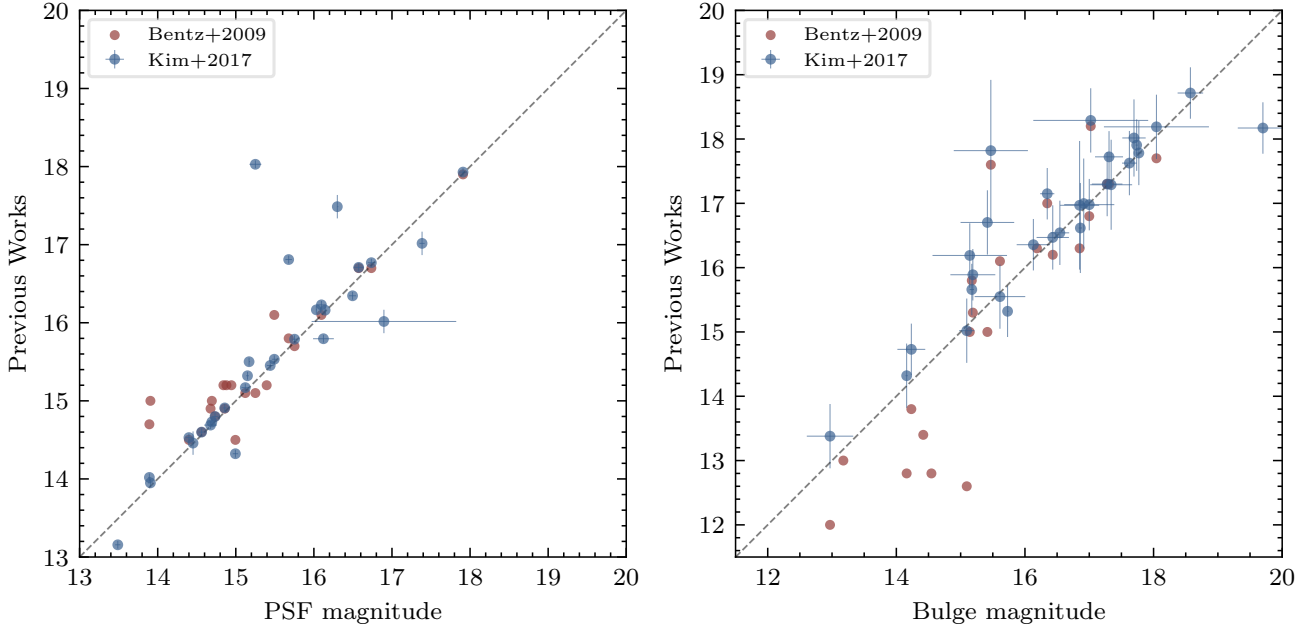


Figure 11. Comparisons of the PSF & bulge magnitudes between our GALFIT fitting and those from the previous works in Bentz et al. (2009) and Kim et al. (2017).

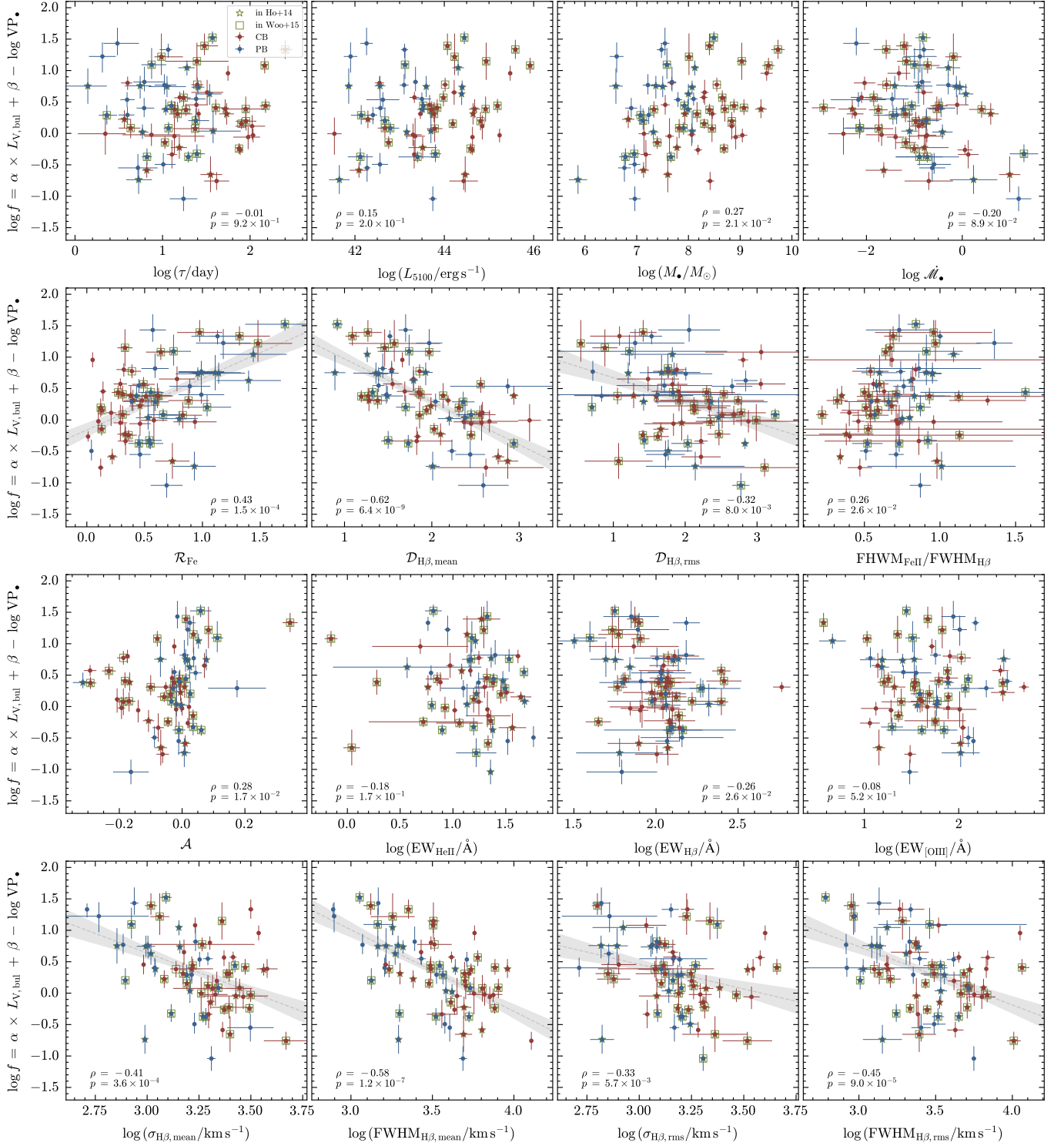


Figure 12. The correlations between f_{MF} and the spectral properties for the total-sample calibration (do not distinguish PB and CB). The meanings of the symbols, lines, and regions are the same as in Figure 3.

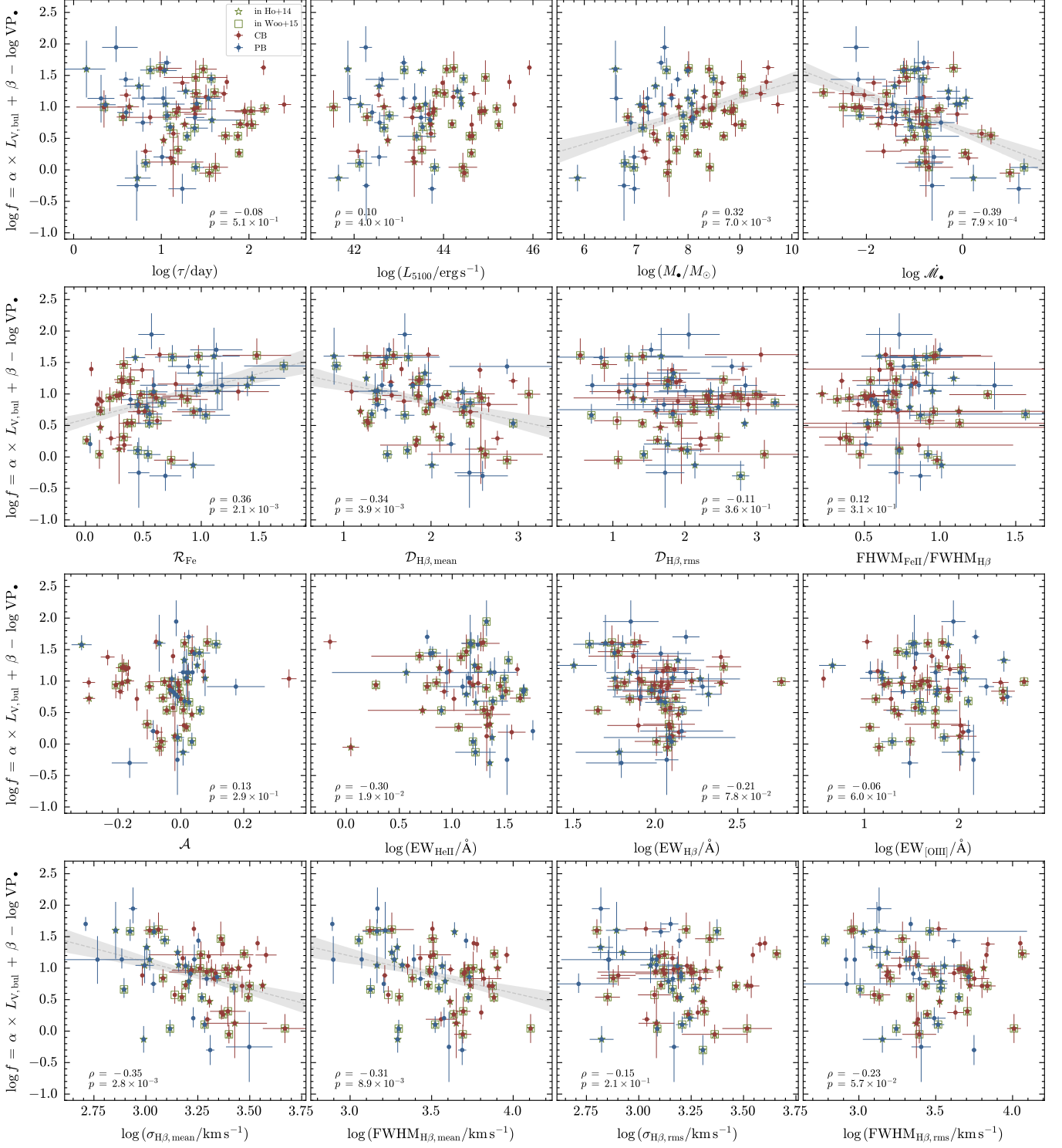


Figure 13. The correlations between f_{MS} and the spectral properties for the total-sample calibration (do not distinguish PB and CB). The meanings of the symbols, lines, and regions are the same as in Figure 3.

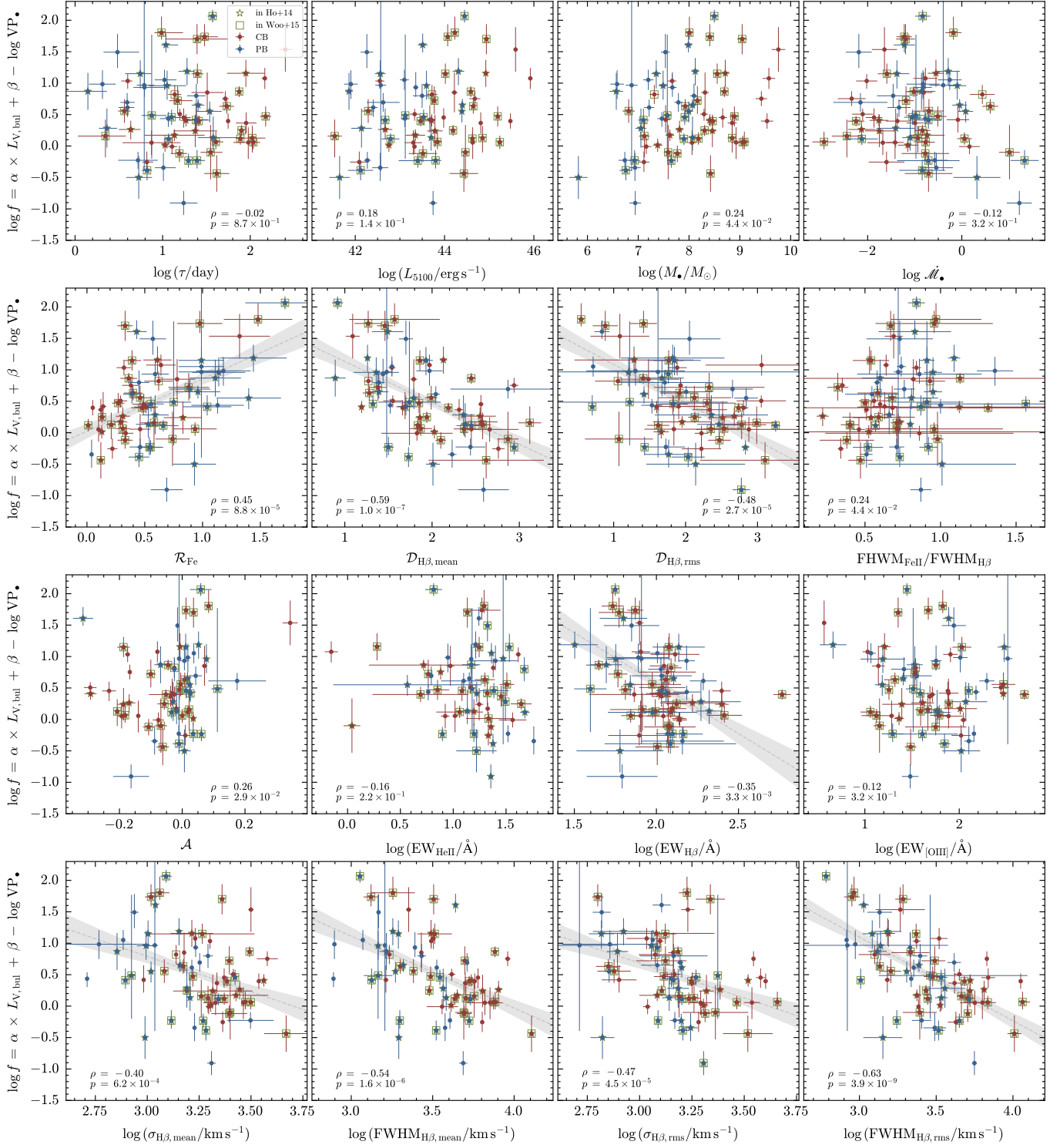


Figure 14. The correlations between f_{RF} and the spectral properties for the total-sample calibration (do not distinguish PB and CB). The meanings of the symbols, lines, and regions are the same as in Figure 3.

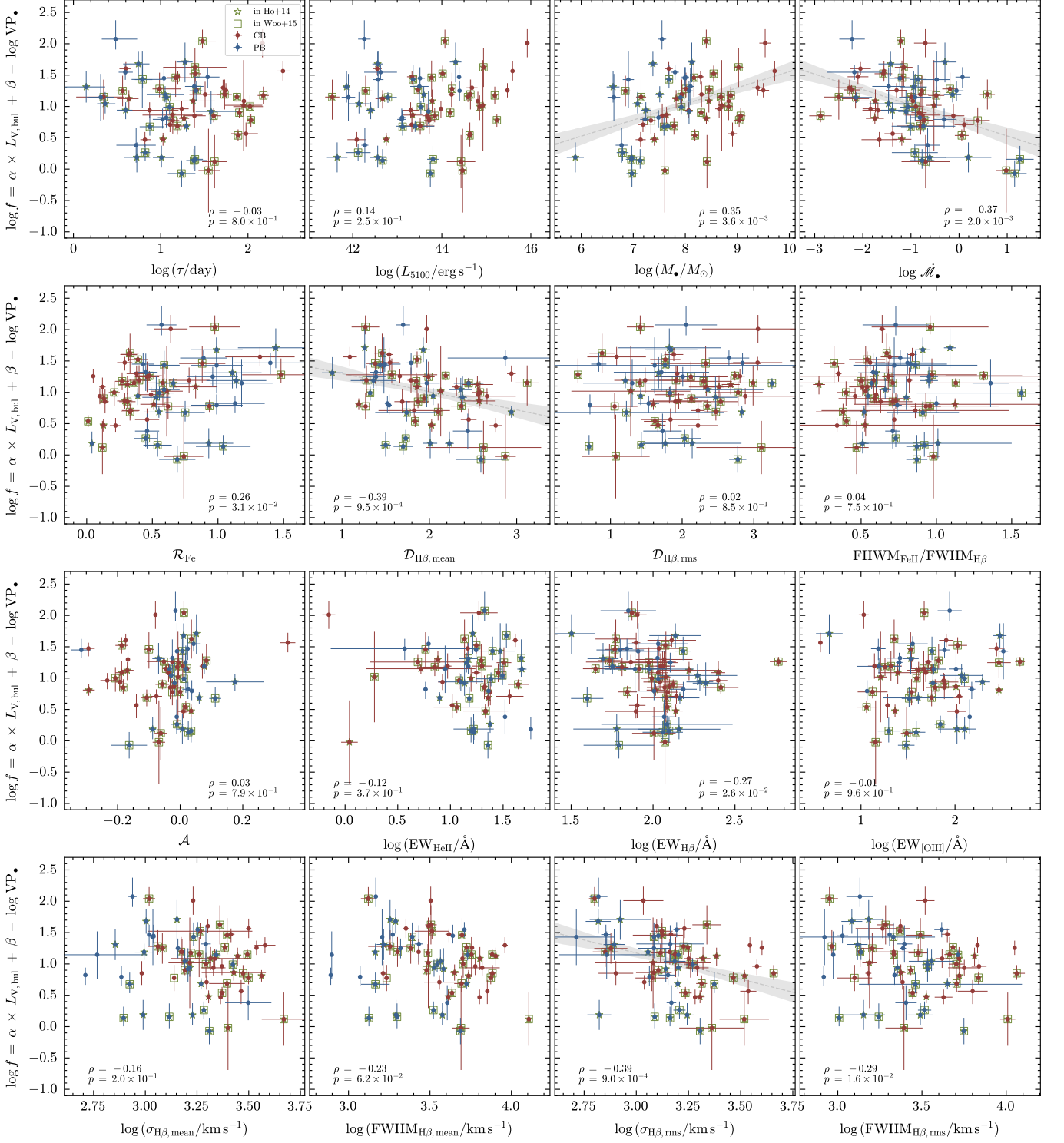


Figure 15. The correlations between f_{RS} and the spectral properties for the total-sample calibration (do not distinguish PB and CB). The meanings of the symbols, lines, and regions are the same as in Figure 3.

Table 1. Target Informations

Name	RA	DEC	A_V	z	Inst./Aper./Filt.	Exp. Time	Dataset
Mrk 335	00:06:19.5	+20:12:10.5	0.11	0.026	ACS/HRC/F550M	2040	J9MU010
PG 0007+106	00:10:31.0	+10:58:29.5	0.313	0.087	WFC3/UVIS1/F547M	2236	ICNO010
PG 0026+129	00:29:13.7	+13:16:04.0	0.221	0.145	WFPC2/PC1/F547M	1445	U9MU520
I Zw1	00:53:34.9	+12:41:36.2	0.198	0.061	WFC3/UVIS2-M1K1C-SUB/F438W	340	IBY8070
PG 0052+251	00:54:52.1	+25:25:39.0	0.146	0.154	WFPC2/WF2/F675W	1991	U402220
Fairall 9	01:23:45.8	-58:48:20.8	0.081	0.046	ACS/HRC/F550M	1020	J8SC040
Mrk 590	02:14:33.6	-00:46:00.1	0.113	0.026	ACS/HRC/F550M	1020	J8SC050
Mrk 1044	02:30:05.5	-08:59:53.3	0.107	0.016	WFC3/UVIS1/F547M	725	IBGU100
3C 120	04:33:11.1	+05:21:15.6	0.922	0.033	ACS/HRC/F550M	1020	J8SC060
Ark 120	05:16:11.4	-00:08:59.4	0.394	0.033	ACS/HRC/F550M	2040	J9MU540
UGC 3374	05:54:53.6	+46:26:21.6	0.661	0.02	WFC3/UVIS-FIX/F547M	2370	ICNO140
Mrk 6	06:52:12.3	+74:25:37.5	0.42	0.02	WFC3/UVIS1/F547M	2620	ICNO030
Mrk 374	06:59:38.1	+54:11:47.9	0.16	0.043	WFC3/UVIS1/F547M	2420	ICNO040
Mrk 79	07:42:32.8	+49:48:34.7	0.22	0.022	ACS/HRC/F550M	2040	J9MU050
Mrk 382	07:55:25.3	+39:11:10.1	0.152	0.033	WFPC2/PC1/F606W	500	U2E6210
PG 0804+761	08:10:58.6	+76:02:42.5	0.11	0.1	ACS/HRC/F550M	2040	J9MU060
NGC 2617	08:35:38.8	-04:05:17.6	0.104	0.014	WFC3/UVIS1/F547M	2230	ICNO130
PG 0844+349	08:47:42.5	+34:45:04.4	0.114	0.064	ACS/WFC1/F625W	1685	J8NT020
Mrk 704	09:18:26.0	+16:18:19.2	0.089	0.029	WFC3/UVIS1/F547M	2240	ICNO050
Mrk 110	09:25:12.9	+52:17:10.5	0.038	0.035	ACS/HRC/F550M	1020	J8SC110
PG 0923+201	09:25:54.7	+19:54:05.1	0.131	0.193	WFPC2/WF2/F675W	1931	U402270
PG 0923+129	09:26:03.3	+12:44:03.6	0.126	0.029	WFC3/UVIS2-M1K1C-SUB/F814W	212	IBY8140
SDSS J093302.68+385228.0	09:33:02.7	+38:52:28.0	0.042	0.177	ACS/WFC1/F606W	2272	JBSZ030
PG 0953+414	09:56:52.4	+41:15:22.3	0.037	0.234	WFPC2/WF2/F675W	1991	U402280
NGC 3227	10:23:30.6	+19:51:54.2	0.07	0.004	ACS/HRC/F550M	1020	J8SC130
Mrk 142	10:25:31.3	+51:40:34.9	0.052	0.045	WFC3/UVIS1/F547M	2450	IB5F010
PG 1100+772	11:04:13.7	+76:58:58.0	0.112	0.312	ACS/WFC/CLEAR1LF814W	1200	JBZ0090
NGC 3516	11:06:47.5	+72:34:06.9	0.129	0.009	ACS/HRC/F550M	2220	J9DQ010
SBS 1116+583A	11:18:57.7	+58:03:23.7	0.035	0.028	WFC3/UVIS1/F547M	2510	IB5F020
Arp 151	11:25:36.2	+54:22:57.0	0.044	0.021	WFC3/UVIS1/F547M	2450	IB5F030
NGC 3783	11:39:01.8	-37:44:19.2	0.378	0.01	WFC3/UVIS-FIX/F547M	2300	IB5E030
Z 186-18	11:39:13.9	+33:55:51.2	0.059	0.032	WFPC2/PC1/F606W	500	U2E61L0
UGC 06728	11:45:16.0	+79:40:53.4	0.317	0.007	WFC3/UVIS1/F547M	1770	IDGO010
Mrk 1310	12:01:14.4	-03:40:41.1	0.094	0.02	WFC3/UVIS1/F547M	2240	IB5F040
NGC 4051	12:03:09.6	+44:31:52.8	0.041	0.002	ACS/HRC/F550M	1020	J8SC160
NGC 4151	12:10:32.6	+39:24:20.6	0.084	0.003	ACS/HRC/F550M	1020	J8SC170
PG 1211+143	12:14:17.7	+14:03:13.1	0.105	0.081	ACS/WFC1/F625W	1655	J8NT030
Mrk 202	12:17:55.0	+58:39:35.5	0.063	0.023	WFC3/UVIS1/F547M	2510	IB5F050
NGC 4253	12:18:26.5	+29:48:46.3	0.061	0.013	WFC3/UVIS1/F547M	2270	IB5F060
Mrk 50	12:23:24.1	+02:40:44.8	0.05	0.024	WFC3/UVIS1/F547M	2230	ICNO060
PG 1226+023	12:29:06.7	+02:03:08.6	0.064	0.158	WFPC2/WF3/F606W	2201	U2SU100
PG 1229+204	12:32:03.6	+20:09:29.2	0.083	0.064	ACS/HRC/F550M	2040	J9MU100
NGC 4593	12:39:39.4	-05:20:39.3	0.077	0.008	WFC3/UVIS-FIX/F547M	2240	IB5E060
IRAS F12397+3333	12:42:10.6	+33:17:02.6	0.06	0.044	ACS/HRC/F625W	2464	J96I090
NGC 4748	12:52:12.5	-13:24:53.0	0.159	0.015	WFC3/UVIS1/F547M	2250	IB5F070
PG 1307+085	13:09:47.0	+08:19:48.2	0.107	0.154	WFPC2/WF3/F606W	2100	U2AR090
PG 1310-108	13:13:05.8	-11:07:42.4	0.162	0.034	WFPC2/PC1/F606W	500	U2E60X0
MCG -6-30-15	13:35:53.7	-34:17:43.9	0.188	0.008	WFC3/UVIS1/F547M	2290	IB5F090
NGC 5273	13:42:08.3	+35:39:15.2	0.032	0.004	WFPC2/PC1/F606W	560	U67N530
IC 4329A	13:49:19.3	-30:18:34.0	0.181	0.016	ACS/HRC/F550M	2220	J9DQ040
PG 1351+695	13:53:03.4	+69:18:29.6	0.049	0.03	ACS/HRC/F550M	1020	J8SC240
PG 1351+640	13:53:15.8	+63:45:45.7	0.064	0.088	ACS/WFC1/F625W	1865	J8NT040

Table 1 continued

Table 1 (continued)

Name	RA	DEC	A_V	z	Inst./Aper./Filt.	Exp. Time	Dataset
NGC 5548	14:17:59.5	+25:08:12.4	0.062	0.017	ACS/HRC/F550M	1020	J8SC270
PG 1426+015	14:29:06.6	+01:17:06.5	0.099	0.087	WFPC2/PC1/F547M	1425	U9MU130
Mrk 817	14:36:22.1	+58:47:39.4	0.021	0.031	ACS/HRC/F550M	1020	J8SC290
PG 1440+356	14:42:07.5	+35:26:22.9	0.044	0.079	WFC3/UVIS1/F547M	2290	ICNO070
PG 1448+273	14:51:08.8	+27:09:26.9	0.092	0.064	WFC3/UVIS2-M1K1C-SUB/F438W	615	IBY8650
Mrk 1511	15:31:18.1	+07:27:27.9	0.126	0.034	WFC3/UVIS1/F547M	2230	ICNO110
PG 1534+580	15:35:52.4	+57:54:09.2	0.044	0.03	WFC3/UVIS1/F547M	2520	IB5F100
PG 1535+547	15:36:38.4	+54:33:33.2	0.045	0.039	WFC3/UVIS2-M1K1C-SUB/F814W	280	IBY8700
Mrk 493	15:59:09.6	+35:01:47.5	0.077	0.031	WFPC2/PC1/F606W	500	U2E62O0
PG 1613+658	16:13:57.2	+65:43:09.6	0.082	0.121	ACS/WFC1/F625W	1955	J8NT060
PG 1617+175	16:20:11.3	+17:24:27.7	0.129	0.115	ACS/WFC1/F625W	1655	J8NT070
PG 1626+554	16:27:56.1	+55:22:31.5	0.018	0.134	WFC3/UVIS2-M1K1C-SUB/F475W	510	IBY8770
PG 1700+518	17:01:24.8	+51:49:20.0	0.103	0.289	WFPC2/PC1/F547M	2240	U4FHA40
3C 382	18:35:03.4	+32:41:46.8	0.217	0.056	WFPC2/PC1/F555W	600	U4493N0
3C 390.3	18:42:09.0	+79:46:17.1	0.222	0.056	ACS/HRC/F550M	1020	J8SC340
Zw 229-015	19:05:25.9	+42:27:39.7	0.225	0.028	WFC3/UVIS1/F547M	2320	ICNO080
NGC 6814	19:42:40.6	-10:19:24.6	0.575	0.005	WFC3/UVIS-FIX/F547M	2240	IB5F120
Mrk 509	20:44:09.7	-10:43:24.5	0.178	0.034	WFPC2/PC1/F547M	1445	U9MU170
PG 2130+099	21:32:27.8	+10:08:19.5	0.138	0.063	WFPC2/WF2/F555W	1800	U2KU010
NGC 7469	23:03:15.6	+08:52:26.4	0.213	0.016	ACS/HRC/F550M	2220	J9DQ030

NOTE— A_V is the Galactic extinction at V-band (Schlegel et al. 1998). “Inst./Aper./Filt.” is the instrument/aperture/filter employed in the *HST* observation used in the present paper. “Exp. Time” is the exposure time. The redshifts (z) are derived from NASAIPAC Extragalactic Database (<https://ned.ipac.caltech.edu/>).

Table 2. Results of GALFIT Fitting

Name	Bulge Type	m_{st}	R_e	n	b/a	P.A.	Note
	(B/T)		(arcsec)			(deg)	
Mrk 335	C	14.68±0.083					PSF
	0.26±0.045	16.85±0.304	0.42±0.31	4	0.74±0.178	12.69±37.113	Bulge
		15.73±0.32	2.57±0.668	1	0.91±0.026	69.13±24.551	Disk
PG 0007+106	C	15.99±0.046					PSF
	0.29±0.022	17.42±0.12	0.34±0.088	1.85±0.59	0.67±0.085	34.81±5.219	Bulge
		16.47±0.317	5.11±0.632	1	0.72±0.022	49.13±22.481	Disk, f
PG 0026+129	E	15.49±0.031					PSF
	1	17.31±0.218	3.79±1.764	4	0.75±0.044	161.74±3.33	Bulge, f
I Zw1	P	14.61±0.021					PSF
	0.31±0.039	17.13±0.213	0.62±0.182	1.73	0.69±0.107	-79.61±1.097	Bulge
		16.24±0.317	3.35±0.65	1	0.92±0.055	103.65±24.975	Disk, f
PG 0052+251	C	16.03±0.004					PSF
	0.75±0.002	17.62±0.114	2.61±0.216	2.12±0.983	0.83±0.016	11.84±5.767	Bulge
		18.81±0.145	4.05±0.047	0.09±0.011	0.55±0.005	24.94±0.411	Disk/Ring
Fairall 9	C	15.25±0.077					PSF
	0.6±0.139	15.19±0.35	2.58±1.077	4	0.83±0.059	1.12±7.99	Bulge
		15.64±0.413	6.27±0.633	1	0.4±0.062	-24.82±1.226	Disk
Mrk 590	P	17.91±0.049					PSF
	0.34±0.01	15.17±0.034	1.3±0.028	1.33±0.052	0.79±0.002	82.52±0.07	Bulge
		14.44±0.317	5.54±0.075	1	0.83±0.006	-17.76±0.216	Disk
Mrk 1044	P	15.22±0.037					PSF
	0.24±0.014	16.14±0.083	0.69±0.025	1±0.204	0.9±0.015	46.63±3.576	Bulge

Table 2 continued

Table 2 (continued)

Name	Bulge Type	m_{st}	R_e	n	b/a	P.A.	Note
	(B/T)		(arcsec)			(deg)	
3C 120		14.9±0.316	6.3±0.118	1	0.67±0.005	-24.43±0.103	Disk
	E	14.86±0.024					PSF
Ark 120	1	15.47±0.577	5.32±8.245	2.6±2.23	0.79±0.023	-57.72±5.56	Bulge
	C	13.89±0.016					PSF
	0.35±0.034	15.14±0.58	1.96±0.799	1.74±0.602	0.8±0.012	72.71±0.684	Bulge
UGC 3374		14.46±0.521	11.88±6.191	1	0.83±0.021	89.28±9.085	Disk, f
	C	15.47±0.047					PSF
	0.31±0.05	14.77±0.213	4.84±1.196	4.52±1.216	0.86±0.01	-87.49±72.028	Bulge
		14.81±0.322	29.31±0.698	0.5	0.21±0.013	73.93±0.071	Bar
Mrk 6		14.55±0.111	33.09±0.109	0.12±0.006	0.49±0.008	79.28±0.411	Disk
	C	14.2±0.839					PSF
	0.72±0.358	14.17±0.934	7.93±6.268	4	0.87±0.038	24.63±72.968	Bulge
Mrk 374		15.2±0.797	17.92±7.288	1	0.39±0.216	18±0.96	Disk
	C	16.44±0.048					PSF
	0.28±0.051	16.22±0.209	1.55±0.409	4	0.74±0.047	55.42±9.011	Bulge
		16.56±0.212	4.07±0.23	1.07±0.161	0.32±0.031	-80.44±0.413	Bar
Mrk 79		15.53±0.108	11.47±0.104	0.28±0.015	0.59±0.004	47.36±0.107	Disk
	C	15.75±0.035					PSF
	0.27±0.082	15.61±0.394	2.46±2.752	2.98±1.686	0.79±0.028	-39.87±7.696	Bulge
Mrk 382	P	16.3					PSF
	0.19±0.004	16.86±0.025	1.09±0.031	0.93±0.062	0.8±0.004	17.56±1.298	Bulge
		16.2±0.1	6.96±0.01	0.39±0.002	0.6±0.001	25.25±0.019	Bar
		15.84±0.1	13.95±0.007	0.22±0.001	0.94±0	-35.63±0.17	Disk
PG 0804+761	E	13.91±0.031					PSF
	1	17±0.39	2.87±1.401	1.17±3.47	0.62±0.179	-1.36±22.151	Bulge
NGC 2617	C	16.44±0.062					PSF
	0.25±0.018	14.46±0.094	7.11±1.022	6.67±0.875	0.85±0.009	64.07±3.623	Bulge
		13.27±0.317	15.2±0.312	1	0.95±0.005	-20.87±2.807	Disk
PG 0844+349	C	14.64±0.083					PSF
	0.64±0.12	16.63±0.208	1.73±1.226	4	0.76±0.075	-16.71±27.615	Bulge
		17.28±0.533	7.86±3.545	1	0.52±0.182	53.7±35.095	Disk
Mrk 704	P	15.03±0.038					PSF
	0.35±0.049	15.8±0.165	1.69±0.138	1.76±0.445	0.71±0.015	-73.29±1.334	Bulge
		17.03±0.14	6.35±0.258	0.36±0.026	0.33±0.032	76.97±0.37	Bar
		15.34±0.124	11.98±0.275	0.47±0.061	0.59±0.002	-77.77±0.115	Disk
Mrk 110	C	16.1±0.06					PSF
	0.28±0.308	17.02±0.893	1.1±3.858	1.98±3.986	0.93±0.014	44.8±6.612	Bulge
		16.01±0.655	7.28±1.285	1	0.76±0.096	-11.46±7.087	Disk, f
PG 0923+201	E	16.5±0.045					PSF
	1	17.74±0.018	3.66±0.945	4	0.92±0.013	-11.72±2.389	Bulge
PG 0923+129	P	16.42±0.01					PSF
	0.3±0.001	16.22±0.006	0.88±0.009	0.83±0.019	0.68±0.005	-87.1±0.239	Bulge
		15.31±0.316	3.46±0.017	1	0.99±0.001	41.68±10.173	Disk
SDSS J093302	P	19.02					PSF
	0.14	19.65±0.5	1.07	0.92	0.96	88.97	Bulge
		18.62±0.5	2.49	0.35	0.8	81.44	Bar
		18.26±0.5	5.55	0.42	0.8	-9.63	Disk
PG 0953+414	E	16.12±0.133					PSF
	1	18.57±0.199	1.94±0.492	1.5	0.91±0.06	-30.56±9.085	Bulge, f
NGC 3227	P	14.88±0.048					PSF
	0.34±0.009	14.55±0.01	0.65±0.024	1.42±0.072	0.75±0.009	58.19±2.47	Bulge
		13.81±0.32	5.31±0.394	1	0.51±0.004	26.64±0.441	Disk, f

Table 2 continued

Table 2 (continued)

Name	Bulge Type	m_{st}	R_e	n	b/a	P.A.	Note
	(B/T)		(arcsec)			(deg)	
Mrk 142	P	16.19±0.028					PSF
	0.2±0.019	17.71±0.125	0.37±0.035	0.85±0.117	0.85±0.022	27.21±8.266	Bulge
		17.11±0.317	3.39±0.024	0.5	0.48±0.005	49.99±0.141	Bar
PG 1100+772		16.84±0.106	7.97±0.012	0.55±0.045	0.82±0.004	22.24±0.926	Disk
	C	16.5±0.955					PSF
	0.66±0.067	17.89±0.397	0.06±0.031	4	0.72±0.202	85.51±8.126	Bulge
NGC 3516		18.61±0.32	2.66±0.188	1	0.84±0.046	-11.76±3.524	Disk
	P	14.84±0.035					PSF
	0.6±0.026	13.18±0.048	2.89±0.157	1.74±0.152	0.75±0.012	-34.52±0.692	Bulge
SBS 1116+583A		13.62±0.326	6.73±0.716	1	0.55±0.025	-107.34±0.884	Disk, f
	P	18.09±0.053					PSF
	0.14±0.004	17.6±0.038	0.66±0.035	1.58±0.24	0.83±0.03	-84.49±2.11	Bulge
Arp 151		17.98±0.116	3.25±0.093	0.53±0.054	0.27±0.004	-82.63±0.191	Bar
		15.77±0.316	5.37±0.033	1	0.88±0.002	-85.01±0.153	Disk
	C	16.95±0.072					PSF
NGC 3783		15.57±0.041	2.76±0.168	5.35±1.03	0.77±0.027	-55.23±1.561	Bulge
		16.8±0.333	5.18±0.54	1	0.27±0.023	-53.35±0.354	Disk
	P	14.42±0.042					PSF
Z 186-18		14.62±0.123	3.03±0.148	1.34±0.286	0.89±0.004	-31.82±2.929	Bulge
		15.08±0.318	11.42±0.12	0.5	0.25±0.006	21.7±0.043	Bar
		12.58±0.101	19.05±0.199	0.55±0.024	0.9±0.001	17.24±0.181	Disk
UGC 06728	P	18.2					PSF
	0.07±0	17.76±0.004	1±0.019	1.03±0.023	0.87±0.003	-53.28±3.214	Bulge
		16.91±0.1	6.05±0.017	0.42±0.004	0.32±0	89.64±0.012	Bar
Mrk 1310		15.21±0.1	11.3±0	0.46±0	0.85	-15.83±0.007	Disk
	P	16.17±0.034					PSF
	0.17±0.008	15.94±0.056	2.96±0.1	1.15±0.103	0.67±0.004	78.84±0.214	Bulge
NGC 4051		15.86±0.104	11.41±0.07	0.42±0.007	0.29±0.006	73.85±0.017	Bar
		14.47±0.316	16.56±0.161	1	0.76±0.002	86.92±0.078	Disk
	C	17.4±0.063					PSF
PG 1211+143		17.39±0.146	0.55±0.302	4	0.87±0.049	-21.5±11.613	Bulge
		15.15±0.317	4.29±0.067	1	0.75±0.004	-18.33±0.602	Disk
	P	14.73±0.036					PSF
Mrk 202		14.16±0.017	1.08±0.033	1.22±0.054	0.87±0.008	-80.03±1.564	Bulge, f
		13.63±0.317	12.11±0.423	1	0.44±0.007	75.38±0.154	Disk
	P	14.4±0.042					PSF
NGC 4151		12.97±0.361	4.7±1.306	4	0.66±0.02	64.87±1.332	Bulge
		13.11±0.349	6.04±0.538	1	0.78±0.074	-25.32±3.126	Disk
	C	14.74±0.035					PSF
PG 1226+023		18.08±0.497	0.08±0.031	4	0.83±0.353	76.04±89.298	Bulge
		17.56±0.316	2.96±0.286	1	0.89±0.02	51.79±2.326	Disk
	C	18.3±0.095					PSF
Mrk 50		16.12±0.035	0.76±0.057	3.57±0.212	0.79±0.017	-82.44±0.853	Bulge
		15.85±0.317	7.25±0.121	1	0.78±0.007	-80.74±0.343	Disk, f
	P	15.77±0.047					PSF
NGC 4253		16.28±0.143	1.4±0.17	1.47±0.401	0.59±0.013	-34.24±1.115	Bulge
		14.77±0.317	7.81±0.075	0.5	0.29±0.005	-48.99±0.096	Bar
		13.49±0.316	16.42±0.073	1	0.84±0.001	106.85±0.242	Disk, f
PG 1226+023	C	16.36±0.048					PSF
	0.26±0.173	16.51±0.594	1.62±1.975	4	0.79±0.033	9.77±4.442	Bulge
		15.38±0.395	5.2±0.12	1	0.78±0.023	13.45±2.681	Disk
PG 1226+023	E	13.49±0.034					PSF

Table 2 continued

Table 2 (continued)

Name	Bulge Type	m_{st}	R_e	n	b/a	P.A.	Note	
	(B/T)		(arcsec)			(deg)		
PG 1229+204	1	16.13±0.259	7.67±2.491	2.75±1.918	0.77±0.026	-108.92±4.291	Bulge, f	
	P	16.74±0.046					PSF	
	0.2±0.017	17.28±0.237	0.62±0.123	1.18±0.568	0.9±0.02	41.23±9.28	Bulge	
NGC 4593		17.58±0.38	4.78±0.309	0.5	0.3±0.052	81.34±1.592	Bar	
		15.97±0.368	6.67±1.489	1	0.81±0.028	105.11±4.851	Disk, f	
	P	16.18±0.118					PSF	
	0.17±0	13.28±0.003	5.14±0.003	0.96±0.007	0.68±0	-53.72±0.025	Bulge	
IRAS F12397+3333		13.54±0.316	36.71±0.04	0.5	0.24±0	78.28±0.007	Bar	
		11.72±0.316	58.36±0.242	1	0.54±0	87.93±0.008	Disk	
	C	16.39±0.221					PSF	
NGC 4748		0.65±0.076	16.4±0.146	0.99±0.124	4.13±0.588	0.91±0.028	-59.74±2.557	Bulge
		17.05±0.267	3.47±0.504	0.82±0.182	0.42±0.066	-52.47±0.374	Disk	
	P	16.09±0.267					PSF	
PG 1307+085		0.14±0.121	15.59±0.711	1.02±1.331	1.66±3.32	0.93±0.022	-82.9±69.172	Bulge
		15.94±0.319	8.16±2.735	0.5	0.38±0.097	70.57±5.278	Bar	
		13.79±0.335	14.15±1.453	1	0.77±0.011	-83.2±2.933	Disk	
PG 1310-108	E	16.9±0.926					PSF	
	1	17.7±0.182	1.01±0.219	4	0.96±0.029	36.18±57.014	Bulge	
MCG -6-30-15	C	15.78					PSF	
		0.2±0.013	17.86±0.073	0.89±0.105	2.65±0.346	0.55±0.025	-45.23±6.656	Bulge
		16.39±0.317	3.8±0.035	1	0.94±0.01	85.67±77.035	Disk	
NGC 5273	P	16.16±0.045					PSF	
		0.04±0.007	16.94±0.215	0.53±0.072	0.83±0.386	0.56±0.068	-51.21±6.109	Bulge
		13.42±0.101	8.1±0.033	1.29±0.054	0.49±0.002	-32.2±0.065	Disk	
IC 4329A	C	17.8±0.044					PSF	
		0.34±0.009	12.89±0.031	10.92±0.467	4.33±0.102	0.88±0	27.98±0.243	Bulge
		12.18±0.101	36.33±0.016	0.59±0.005	0.82±0	29.51±0.012	Disk	
PG 1351+695	P	14.56±0.037					PSF	
		0.19±0.017	15.1±0.118	2.14±0.033	0.49±0.13	0.92±0.004	6.36±2.154	Bulge
		13.49±0.316	13.71±0.955	1	0.48±0.023	-76.13±0.162	Disk	
PG 1351+640	P	14.69±0.039					PSF	
		0.21±0.045	16.43±0.251	0.44±0.06	0.97±0.587	0.71±0.016	71.57±2.664	Bulge, f
		15.01±0.317	4.13±0.418	1	0.57±0.012	73.39±0.774	Disk, f	
NGC 5548	E	15.15±0.017					PSF	
	1	16.54±0.145	2.19±0.409	2.95±1.1	0.96±0.013	-18.13±11.994	Bulge	
	C	16.57±0.064					PSF	
PG 1426+015		0.36±0.089	14.23±0.217	4.99±1.87	3.94±1.946	0.88±0.018	-80.34±7.445	Bulge
		13.6±0.288	11.8±1.208	1.44±0.682	0.93±0.006	20.51±18.931	Disk, f	
	C	15.4±0.009					PSF	
Mrk 817		0.7±0.232	16.19±0.742	7.16±2.455	4	0.84±0.232	-12.12±4.247	Bulge
		17.09±0.453	6.89±0.822	1	0.33±0.089	89.35±0.368	Disk	
	P	15.12±0.048					PSF	
PG 1440+356		0.04±0.027	18.04±0.817	0.2±0.151	0.39±3.092	0.8±0.126	30.69±23.079	Bulge
		17.43±0.758	4.77±0.513	0.5	0.21±0.088	-45.8±0.743	Bar	
		14.54±0.366	6.26±1.832	1	0.81±0.034	-27.29±11.637	Disk	
	P	14.82±0.039					PSF	
PG 1448+273		0.15±0.062	17.95±0.668	0.25±0.125	0.31±0.205	0.81±0.186	26.97±77.414	Bulge
		17.59±0.317	1.39±0.078	0.5	0.56±0.002	52.62±0.442	Bar	
		16.35±0.316	4.72±0.125	1	0.86±0.004	83.52±2.446	Disk	
PG 1448+273	C	15.06±0.017					PSF	
		0.36±0.03	17.33±0.135	0.07±0.025	4	0.42±0.236	-5.29±43.291	Bulge
		16.69±0.316	1.99±0.173	1	0.79±0.017	-5.52±0.498	Disk	

Table 2 continued

Table 2 (continued)

Name	Bulge Type	m_{st}	R_e	n	b/a	P.A.	Note	
	(B/T)		(arcsec)			(deg)		
Mrk 1511	P	16.71±0.033					PSF	
	0.02±0.002	17.59±0.102	0.43±0.015	1.75±0.622	0.89±0.033	-30.72±14.176	Bulge	
		15.47±0.316	10.1±0.041	0.5	0.34±0.001	0.35±0.068	Bar	
PG 1534+580		13.65±0.316	18.68±0.097	1	0.94±0.001	34.11±0.395	Disk	
	C	15.31±0.053					PSF	
	0.34±0.051	16.51±0.159	0.47±0.434	4	0.88±0.062	-72.92±7.353	Bulge	
PG 1535+547		15.78±0.327	4.69±0.592	1	0.89±0.022	-81.96±5.16	Disk, f	
	P	15.68±0.016					PSF	
	0.2±0.016	18.5±0.106	0.81±0.045	0.59±0.173	0.31±0.006	71.86±1.517	Bulge	
Mrk 493		16.98±0.316	3.37±0.052	1	0.32±0.004	72.04±0.042	Disk, f	
	P	17.39±0.034					PSF	
	0.13±0.002	16.91±0.018	0.59±0.003	0.29±0.021	0.9±0.005	-1.53±0.702	Bulge	
PG 1613+658		15.85±0.316	8.37±0.031	0.5	0.3±0	-79.13±0.026	Disk	
		15.42±0.1	16.25±0.053	0.18±0.005	0.55±0.003	-88.83±0.007	Bar	
	E	15.17±0.011					PSF	
PG 1617+175	1	15.73±0.126	5.17±0.828	1.61±0.427	0.8±0.008	-48.01±0.863	Bulge, f	
	C	16.14±0.012					PSF	
	0.24±0.075	19.7±0.391	0.39±0.149	4	0.72±0.173	-46.26±30.729	Bulge	
PG 1626+554		18.45±0.32	1.93±0.09	1	0.79±0.031	68.89±8.059	Disk	
	C	15.93±0.072					PSF	
	0.26±0.158	19.2±0.617	0.26	4	0.92	77.46	Bulge	
PG 1700+518		18.05±0.358	3.43	1	0.95	76.73	Disk	
	E	15.44±0.043					PSF	
	1	17.77±0.047	2.6±0.923	4	0.87±0.026	5.22±3.205	Bulge, f	
3C 382	E	14.89±0.025					PSF	
	1	14.85±0.004	4.87±0.128	4	0.78±0.003	11.08±0.272	Bulge	
3C 390.3	E	15.68±0.042					PSF	
	1	16.35±0.11	1.81±0.255	2.02±0.452	0.78±0.024	-11.85±2.478	Bulge	
Zw 229-015	P	16.94±0.057					PSF	
	0.09±0.003	17.42±0.032	0.68±0.012	0.77±0.046	0.7±0.004	-51.07±1.538	Bulge	
		15.95±0.108	8.58±0.22	0.73±0.025	0.39±0.01	-62.7±0.03	Bar	
NGC 6814		15.41±0.112	16.14±0.452	2.69±0.372	0.85±0.007	-44.59±1.535	Disk	
	P	16.22±0.044					PSF	
	0.03±0.003	15.07±0.13	1.52±0.126	1.48±0.236	0.94±0.01	-88.46±1.939	Bulge	
Mrk 509		14.76±0.325	5.9±0.184	0.5	0.66±0.022	83.06±0.122	Bar	
		11.25±0.316	44.5±0.042	1	0.98±0.001	80.31±0.119	Disk	
	C	14.99±0.034					PSF	
PG 2130+099		0.58±0.198	15.42±0.417	1.99±1.139	4	0.57±0.062	-53.56±3.181	Bulge
		15.75±0.674	3.64±0.277	1	0.92±0.069	-4.73±25.077	Disk	
	P	14.45					PSF	
NGC 7469		0.31±0.059	17.34±0.326	2.43±0.37	0.43±0.169	0.57±0.017	-49.07±1.413	Bulge
		16.46±0.102	10.65±0.097	0.36±0.016	0.45±0.001	-36.24±0.124	Disk	
	P	14.94±0.043					PSF	
NGC 7469		0.18±0.011	14.42±0.378	1.71±1.095	1.69±0.887	0.68±0.015	19.39±3.038	Bulge, f
		12.79±0.495	19.94±17.753	1	0.47±0.128	70.31±2.755	Disk	

NOTE—“B/T” is the bulge-to-total luminosity ratio. “ m_{st} ” is the apparent magnitude in ST magnitude system. “ R_e ” is the effective radius. “ n ” is the Sérsic indexes. “ b/a ” is the axial ratio. “P.A.” is the position angle. “f” in the last column denotes that the fourier mode is used in the fitting. “C”, “P”, and “E” represents the classifications of CB, PB and elliptical. The parameters without errors are fixed in the fitting. We note here that the uncertainties here include the error bars from the GALFIT and the uncertainties from the PSF mismatch (see Section 2.2.3). The systematic errors resulting from the over- or under-estimation of the sky background (0.1 mag) and those caused by fixing the Sérsic index (0.3 mag for some objects) are not included here, but are added in quadrature to the total error bars in the analysis in Section 3.

Table 3. Measurements of RM campaigns

Name	FWHM _{Hβ,mean}	$\sigma_{H\beta,mean}$	FWHM _{Hβ,rms}	$\sigma_{H\beta,rms}$	$\tau_{H\beta}$	log L_{5100}	EW(H β)	EW([O III])	References
	(km s ⁻¹)	(km s ⁻¹)	(km s ⁻¹)	(km s ⁻¹)	(days)	(erg s ⁻¹)	(Å)	(erg s ⁻¹)	
Mrk 335	1748 ⁺¹²⁰ ₋₁₂₀	1259 ⁺⁶⁰ ₋₆₀	836 ⁺³⁴⁸ ₋₃₄₈	589 ⁺⁹⁸ ₋₉₈	17 ^{+2.5} _{-3.2}	43.51 ^{+0.07} _{-0.07}	133.37 ± 8.57	39.42 ± 3.24	8
	2096 ⁺¹⁷⁰ ₋₁₇₀	1470 ⁺⁵⁰ ₋₅₀	1561 ⁺⁶¹ ₋₂₂	1287 ⁺¹⁸ ₋₃₃	8.7 ^{+1.6} _{-1.9}	43.69 ^{+0.06} _{-0.06}	110.5 ± 22.3	31.8 ± 2.4	1,5
	1792 ⁺³ ₋₃	1380 ⁺⁶ ₋₆	1629 ⁺¹⁴⁵ ₋₁₄₅	917 ⁺⁵² ₋₅₂	16.8 ^{+4.8} _{-4.2}	43.76 ^{+0.06} _{-0.06}	119.7 ± 23.3	36.9 ± 1.9	1,3,5
	1679 ⁺² ₋₂	1371 ⁺⁸ ₋₈	1375 ⁺³⁵⁷ ₋₃₅₇	948 ⁺¹¹³ ₋₁₁₃	12.5 ^{+6.6} _{-5.5}	43.84 ^{+0.06} _{-0.06}	111.2 ± 21.1	31.1 ± 1.6	1,3,5
	1724 ⁺²³⁶ ₋₂₃₆	1542 ⁺⁶⁶ ₋₆₆	1025 ⁺³⁵ ₋₃₅	1293 ⁺⁶⁴ ₋₆₄	14.3 ^{+0.7} _{-0.7}	43.74 ^{+0.06} _{-0.06}	89.5 ± 19.5	38.6 ± 2.5	1,5,7
	1714⁺⁵⁸₋₅₈	1378⁺²¹₋₂₁	1257⁺³⁰²₋₃₀₁	1188⁺²¹⁵₋₂₁₆	13.75^{+2.37}_{-2.37}	43.72^{+0.12}_{-0.12}	122.8 ± 18.11	34.49 ± 3.88	...
PG 0007+106	5301⁺³³₋₂₈	2424⁺³⁹₋₄₁	4832⁺¹⁰₋₁₁	1766⁺¹¹₋₉	25.8^{+1.2}_{-1.1}	43.46^{+0.06}_{-0.06}	582.73 ± 70.85	491.28 ± 58.56	2
PG 0026+129	3374 ⁺²⁷ ₋₂₇	2274 ⁺⁴ ₋₄	2735 ⁺⁵⁷⁸ ₋₅₇₈	2446 ⁺⁸⁸ ₋₈₈	11.7 ^{+7.4} _{-7.8}	44.9 ^{+0.01} _{-0.01}	70.96 ± 8.26	26.68 ± 2.47	11
	3198 ⁺²¹ ₋₂₁	2315 ⁺⁴ ₋₄	1902 ⁺¹¹⁴ ₋₁₁₄	1901 ⁺⁹⁷ ₋₉₇	27.7 ⁺⁵ ₋₆	44.95 ^{+0.01} _{-0.01}	74.35 ± 6.04	22.33 ± 2.18	11
	2544 ⁺⁵⁶ ₋₅₆	1738 ⁺¹⁰⁰ ₋₁₀₀	1718 ⁺⁴⁹⁵ ₋₄₉₅	1774 ⁺²⁸⁵ ₋₂₈₅	111 ^{+24.1} _{-28.3}	44.97 ^{+0.02} _{-0.02}	46.2 ± 4.7	21.6 ± 1.2	1,3,10
	3206⁺²⁶⁰₋₂₆₀	2294⁺³²₋₃₂	1923⁺²²⁵₋₂₂₅	2179⁺³⁴⁹₋₃₄₉	24.7^{+20.59}_{-20.72}	44.94^{+0.03}_{-0.03}	59.2 ± 16.9	22.52 ± 2.4	...
I Zw1	1131⁺³⁵₋₃₈	1233⁺⁷⁷₋₇₇	606⁺²⁸₋₂₈	...	37.2^{+4.5}_{-4.9}	44.45^{+0.02}_{-0.02}	56.15 ± 1.43	27.93 ± 0.64	37
PG 0052+251	5008⁺⁷³₋₇₃	2167⁺³⁰₋₃₀	4165⁺³⁸¹₋₃₈₁	1783⁺⁸⁶₋₈₆	89.8^{+24.5}_{-24.1}	44.81^{+0.03}_{-0.03}	107.4 ± 14.8	48.9 ± 3.6	1,3,15
Fairall 9	5999⁺⁶⁶₋₆₆	2347⁺¹⁶₋₁₆	6901⁺⁷⁰⁷₋₇₀₇	3787⁺¹⁹⁷₋₁₉₇	17.4^{+3.2}_{-4.3}	43.98^{+0.04}_{-0.04}	249.8 ± 32	75.8 ± 4.5	1,3,16
Mrk 590	2788 ⁺²⁹ ₋₂₉	1942 ⁺²⁶ ₋₂₆	1675 ⁺⁵⁸⁷ ₋₅₈₇	789 ⁺⁷⁴ ₋₇₄	20.7 ^{+3.5} _{-2.7}	43.59 ^{+0.06} _{-0.06}	107 ± 22	25.8 ± 2.1	1,3
	3729 ⁺⁴²⁶ ₋₄₂₆	2168 ⁺³⁰ ₋₃₀	2566 ⁺¹⁰⁶ ₋₁₀₆	1934 ⁺⁵² ₋₅₂	14 ^{+8.5} _{-8.8}	43.14 ^{+0.09} _{-0.09}	142.8 ± 62.2	74.4 ± 13.2	1,3
	2744 ⁺⁷⁹ ₋₇₉	1967 ⁺¹⁹ ₋₁₉	2115 ⁺⁵⁷⁵ ₋₅₇₅	1251 ⁺⁷² ₋₇₂	29.2 ^{+4.9} ₋₅	43.38 ^{+0.07} _{-0.07}	119.7 ± 28.1	42.3 ± 4.7	1,3
	2500 ⁺⁴² ₋₄₂	1880 ⁺¹⁹ ₋₁₉	1979 ⁺³⁸⁶ ₋₃₈₆	1201 ⁺¹³⁰ ₋₁₃₀	28.8 ^{+3.6} _{-4.2}	43.65 ^{+0.06} _{-0.06}	94.9 ± 20.7	22.8 ± 1.8	1,3
	2705⁺¹⁶²₋₁₆₂	1962⁺¹⁰⁷₋₁₀₇	2488⁺²⁶⁶₋₂₆₆	1454⁺⁵⁴³₋₅₄₃	24.23^{+5.92}_{-5.87}	43.5^{+0.21}_{-0.21}	106.51 ± 19.13	25.97 ± 8.18	...
Mrk 1044	1178⁺²²₋₂₂	766⁺⁸₋₈	825⁺⁶₋₆	1156⁺³₋₂	10.5^{+3.3}_{-2.7}	43.1^{+0.1}_{-0.1}	101.4 ± 31.9	11.6 ± 1.4	1,17
3C 120	2327 ⁺⁴⁸ ₋₄₈	1248 ⁺²¹ ₋₂₁	2205 ⁺¹⁸⁵ ₋₁₈₅	1166 ⁺⁵⁰ ₋₅₀	38.1 ^{+18.3} _{-18.3}	44.07 ^{+0.05} _{-0.05}	100.9 ± 18.3	81.2 ± 5	1,3,10
	3529 ⁺¹⁷⁶ ₋₁₇₆	1908 ⁺⁹⁵ ₋₉₅	2539 ⁺⁴⁶⁶ ₋₄₆₆	1514 ⁺⁶⁵ ₋₆₅	25.9 ^{+2.3} _{-2.3}	43.94 ^{+0.05} _{-0.05}	135.9 ± 22.3	134 ± 5.1	1,7
	3711 ⁺³⁴ ₋₃₄	3174 ⁺³² ₋₃₂	2343 ⁺²⁶ ₋₂₆	1360 ⁺⁴² ₋₄₂	20.2 ⁺⁵ _{-4.2}	44.04 ^{+0.05} _{-0.05}	119.36 ± 5.6	106.16 ± 4.15	40
	3255⁺⁷⁹²₋₇₉₂	1842⁺¹⁰⁷⁰₋₁₀₇₀	2341⁺³⁷₋₃₇	1326⁺¹⁵⁷₋₁₅₇	24.93^{+3.91}_{-3.88}	44.02^{+0.07}_{-0.07}	118.77 ± 9.51	106.69 ± 24.67	...
Ark 120	6042 ⁺³⁵ ₋₃₅	1753 ⁺⁶ ₋₆	5536 ⁺²⁹⁷ ₋₂₉₇	1959 ⁺¹⁰⁹ ₋₁₀₉	47.1 ^{+8.3} _{-12.4}	43.98 ^{+0.06} _{-0.06}	211.5 ± 37.5	18.5 ± 1.6	1,3,10
	6246 ⁺⁷⁸ ₋₇₈	1862 ⁺¹³ ₋₁₃	5284 ⁺²⁰³ ₋₂₀₃	1884 ⁺⁴⁸ ₋₄₈	37.1 ^{+4.8} _{-5.4}	43.63 ^{+0.08} _{-0.08}	321.1 ± 77.6	41.5 ± 6.5	1,3,10
	6487 ⁺¹⁶ ₋₁₆	3929 ⁺¹⁴ ₋₁₄	5247 ⁺²⁵ ₋₂₅	2184 ⁺³¹ ₋₃₁	16.2 ^{+3.2} _{-3.1}	43.71 ^{+0.05} _{-0.05}	252.86 ± 13.14	39.11 ± 2.7	40
	6404⁺²⁰⁷₋₂₀₇	2069⁺⁹⁰⁹₋₉₀₉	5250⁺³⁹₋₃₉	2088⁺¹⁶⁹₋₁₆₉	23.55^{+13.6}_{-13.62}	43.78^{+0.17}_{-0.17}	250.15 ± 24.21	24.62 ± 11.76	...
UGC 3374	4139⁺²⁰⁷₋₂₀₇	2597⁺¹⁰⁰₋₁₀₀	4475⁺¹⁹²₋₃₅₆	1466⁺¹⁰²₋₁₇₄	15.72^{+0.5}_{-0.52}	43.33^{+0.11}_{-0.11}	108.7 ± 35.3	276.8 ± 54.3	1,18
Mrk 6	5457⁺¹⁶₋₁₆	3647⁺²⁹₋₂₉	5274⁺²²₋₂₂	3300⁺³⁰₋₃₀	18.5^{+2.5}_{-2.4}	43.71^{+0.08}_{-0.08}	103.61 ± 12.94	293.4 ± 23.1	40
Mrk 374	4980⁺²⁴⁹₋₂₄₉	2486⁺¹⁰⁰₋₁₀₀	3094⁺⁴⁸⁸₋₆₁₉	1329⁺³⁰⁸₋₄₂₉	14.84^{+5.76}_{-3.3}	43.77^{+0.04}_{-0.04}	58.3 ± 7.9	33.7 ± 1.8	18
Mrk 79	5056 ⁺⁸⁵ ₋₈₅	2314 ⁺²³ ₋₂₃	5086 ⁺¹⁴³⁶ ₋₁₄₃₆	2137 ⁺³⁷⁵ ₋₃₇₅	9 ^{+8.3} _{-7.8}	43.63 ^{+0.07} _{-0.07}	92.4 ± 21	56.1 ± 3.8	1,3,10
	4760 ⁺³¹ ₋₃₁	2281 ⁺²⁶ ₋₂₆	4219 ⁺²⁶² ₋₂₆₂	1682 ⁺⁷² ₋₇₂	16.1 ^{+6.6} _{-6.6}	43.74 ^{+0.07} _{-0.07}	78.1 ± 18.3	44 ± 2.9	1,3,10
	4766 ⁺⁷¹ ₋₇₁	2312 ⁺²¹ ₋₂₁	5251 ⁺⁵³³ ₋₅₃₃	1854 ⁺⁷² ₋₇₂	16 ^{+6.4} _{-5.8}	43.66 ^{+0.07} _{-0.07}	86 ± 19.3	51.9 ± 3.5	1,3,10
	6191 ⁺⁷⁸ ₋₇₈	3505 ⁺³² ₋₃₂	5087 ⁺²⁷ ₋₂₇	2092 ⁺¹⁸ ₋₁₈	16.2 ^{+2.4} _{-3.5}	43.06 ^{+0.07} _{-0.07}	158.85 ± 11.58	246.65 ± 10.14	39
	4941⁺⁵¹⁰₋₅₁₀	2483⁺⁴⁹⁴₋₄₉₄	5078⁺¹⁰⁶₋₁₀₆	2056⁺¹²⁴₋₁₂₄	15.54^{+3.13}_{-3.5}	43.52^{+0.32}_{-0.32}	120.68 ± 43.72	56.36 ± 42.16	...
Mrk 382	1462⁺²⁹⁶₋₂₉₆	840⁺³⁷₋₃₇	2890⁺⁴²¹³₋₂₂₂₉	2364⁺⁴⁰₋₅₃	7.5^{+2.9}₋₂	43.12^{+0.08}_{-0.08}	39.6 ± 9	32.5 ± 5.9	1,17
PG 0804+761	3251 ⁺⁸¹ ₋₈₁	2007 ⁺²⁴ ₋₂₄	1534 ⁺¹²¹ ₋₁₂₁	822 ⁺⁷⁴ ₋₇₄	72.9 ⁺⁹ ₋₁₁	44.94 ^{+0.02} _{-0.02}	117.71 ± 8.89	10.01 ± 3.39	8
	3053 ⁺³⁸ ₋₃₈	1434 ⁺¹⁸ ₋₁₈	2012 ⁺⁸⁴⁵ ₋₈₄₅	1971 ⁺¹⁰⁵ ₋₁₀₅	146.9 ^{+18.8} _{-18.9}	44.91 ^{+0.02} _{-0.02}	122.5 ± 10.3	16.6 ± 0.9	1,3
	3089⁺¹¹³₋₁₁₃	1640⁺³⁸⁹₋₃₈₉	1544⁺¹⁵³₋₁₅₃	1203⁺⁷⁶⁸₋₇₆₈	89.15^{+44.08}_{-44.36}	44.92^{+0.02}_{-0.02}	119.76 ± 7.52	16.17 ± 2.47	...
NGC 2617	8026⁺⁴⁰¹₋₄₀₁	2791⁺⁶₋₆	6489⁺²¹³₋₁₆₂	2424⁺⁹¹₋₈₆	4.32^{+1.1}_{-1.35}	42.67^{+0.16}_{-0.16}	165.8 ± 74.9	41 ± 11.4	1,18
PG 0844+349	2694⁺⁵⁸₋₅₈	1505⁺¹⁴₋₁₄	2148⁺⁶¹²₋₆₁₂	1448⁺⁷⁹₋₇₉	32.3^{+13.7}_{-13.4}	44.22^{+0.07}_{-0.07}	111.2 ± 22.1	13.9 ± 2.2	1,3,19
Mrk 704	3502⁺³²₋₃₀	2650⁺⁴₋₃	3406⁺³¹⁰₋₂₄₀	1860⁺¹⁹⁸₋₁₃₀	12.65^{+1.49}_{-1.24}	43.53^{+0.06}_{-0.06}	107.55 ± 8.59	126.04 ± 7.37	36
Mrk 110	1543 ⁺⁵ ₋₅	962 ⁺¹⁵ ₋₁₅	1494 ⁺⁸⁰² ₋₈₀₂	1196 ⁺¹⁴¹ ₋₁₄₁	24.3 ^{+5.5} _{-8.3}	43.68 ^{+0.04} _{-0.04}	139.6 ± 20.4	78.3 ± 5.4	1,3,10
	1658 ⁺³ ₋₃	953 ⁺¹⁰ ₋₁₀	1381 ⁺⁵²⁸ ₋₅₂₈	1115 ⁺¹⁰³ ₋₁₀₃	20.4 ^{+10.5} _{-6.3}	43.75 ^{+0.04} _{-0.04}	94.8 ± 14.7	66.2 ± 4.5	1,3,10
	1600 ⁺³⁹ ₋₃₉	987 ⁺¹⁸ ₋₁₈	1521 ⁺⁵⁹ ₋₅₉	755 ⁺²⁹ ₋₂₉	33.3 ^{+14.9} ₋₁₀	43.53 ^{+0.05} _{-0.05}	139.4 ± 20.5	110.7 ± 8.3	1,3,10
	1632⁺⁵⁹₋₅₉	961⁺¹⁷₋₁₇	1520⁺⁶²₋₆₂	798⁺¹⁵³₋₁₅₃	24.37^{+7.24}_{-7.15}	43.67^{+0.11}_{-0.11}	117.52 ± 29.25	77 ± 18.73	...
PG 0923+201	7469⁺²⁷³₋₂₇₃	3156⁺¹⁰⁹₋₁₀₉	6853⁺²¹⁴₋₂₁₄	2914⁺⁸⁸₋₈₈	108.2^{+6.6}_{-12.3}	45.24^{+0.02}_{-0.02}	69.7 ± 9.29	13.28 ± 4.86	13

Table 3 continued

Table 3 (continued)

Name	FWHM _{Hβ} ,mean (km s ⁻¹)	σ _{Hβ} ,mean (km s ⁻¹)	FWHM _{Hβ} ,rms (km s ⁻¹)	σ _{Hβ} ,rms (km s ⁻¹)	τ _{Hβ} (days)	log L ₅₁₀₀ (erg s ⁻¹)	EW(H β) (Å)	EW([O III]) (erg s ⁻¹)	References
PG 0923+129	2461 ⁺³⁴ ₋₃₄	1711 ⁺⁵¹ ₋₄₈	2138 ⁺¹⁷ ₋₁₃	1215 ⁺²⁰ ₋₁₉	6.2 ^{+3.2} _{-1.8}	43.36 ^{+0.06} _{-0.06}	152.7 ± 17.65	56.83 ± 7.56	2
SDSS J093302	1800 ⁺²⁵ ₋₂₅	1423 ⁺⁷ ₋₇	1526 ⁺³¹³ ₋₃₁₃	838 ⁺²⁸³ ₋₂₈₃	19 ^{+3.8} _{-4.3}	44.31 ^{+0.13} _{-0.13}	31.8 ± 10.3	4.6 ± 1.5	1,14
PG 0953+414	3071 ⁺²⁷ ₋₂₇	1659 ⁺³¹ ₋₃₁	3002 ⁺³⁹⁸ ₋₃₉₈	1306 ⁺¹⁴⁴ ₋₁₄₄	150.1 ^{+21.6} _{-22.6}	45.19 ^{+0.01} _{-0.01}	64.7 ± 5.9	18 ± 1	1,3,10
NGC 3227	4112 ⁺²⁰⁶ ₋₂₀₆	1688 ⁺⁸⁴ ₋₈₄	3578 ⁺⁸³ ₋₈₃	1376 ⁺⁴⁴ ₋₄₄	3.75 ^{+0.76} _{-0.82}	42.24 ^{+0.11} _{-0.11}	71 ± 23.6	142.2 ± 22.1	1,5,17,21
	4032 ⁺⁵⁷ ₋₅₇	3370 ⁺³³ ₋₃₃	2476 ⁺²¹ ₋₂₁	1502 ⁺²⁴ ₋₂₄	7.6 ⁺¹ ₋₁	42.29 ^{+0.09} _{-0.09}	120.39 ± 6.58	143.22 ± 3.08	39
	4038 ⁺⁶² ₋₆₂	3145 ⁺⁸¹⁰ ₋₈₁₀	2542 ⁺³⁷¹ ₋₃₇₁	1473 ⁺⁷⁸ ₋₇₈	5.23 ^{+2.72} _{-2.72}	42.27 ^{+0.08} _{-0.08}	116.83 ± 19.14	143.2 ± 3.05	...
Mrk 142	1588 ⁺⁵⁸ ₋₅₈	948 ⁺¹² ₋₁₂	1374 ⁺⁴² ₋₄₄	1138 ⁺⁴ ₋₄	7.9 ^{+2.9} ₋₂	43.56 ^{+0.06} _{-0.06}	55.2 ± 9.5	10 ± 1.3	1,17
	1462 ⁺² ₋₂	1116 ⁺²² ₋₂₂	1368 ⁺³⁷⁹ ₋₃₇₉	859 ⁺¹⁰² ₋₁₀₂	15.3 ^{+2.7} _{-2.7}	43.61 ^{+0.04} _{-0.04}	57.6 ± 8.6	21.9 ± 1.4	1,20
	1462 ⁺⁶ ₋₆	987 ⁺¹⁰⁰ ₋₁₀₀	1373 ⁺⁴² ₋₄₄	1138 ⁺¹⁶ ₋₁₆	11.24 ^{+5.58} _{-5.46}	43.59 ^{+0.05} _{-0.05}	56.52 ± 6.6	15.51 ± 8.44	...
PG 1100+772	5733 ⁺³² ₋₂₁	3449 ⁺³¹ ₋₃₀	11229 ⁺²⁹ ₋₂₃	4002 ⁺⁸⁷ ₋₈₇	55.9 ⁺³ _{-1.4}	45.47 ^{+0.02} _{-0.02}	73.24 ± 46.24	51.94 ± 4.08	2
NGC 3516	5384 ⁺²⁶⁹ ₋₂₆₉	2201 ⁺¹¹⁰ ₋₁₁₀	5175 ⁺⁹⁶ ₋₉₆	1591 ⁺¹⁰ ₋₁₀	11.7 ⁺¹ _{-1.5}	42.79 ^{+0.2} _{-0.2}	94.7 ± 59.2	59.5 ± 18.2	1,5,10,21
SBS 1116+583A	3668 ⁺¹⁸⁶ ₋₁₈₆	1552 ⁺³⁶ ₋₃₆	3604 ⁺¹¹²³ ₋₁₁₂₃	1528 ⁺¹⁸⁴ ₋₁₈₄	2.31 ^{+0.62} _{-0.49}	42.14 ^{+0.23} _{-0.23}	186.8 ± 104.1	117.4 ± 61.1	1,10,20
Arp 151	3098 ⁺⁶⁹ ₋₆₉	2006 ⁺²⁴ ₋₂₄	2357 ⁺¹⁴² ₋₁₄₂	1252 ⁺⁴⁶ ₋₄₆	3.99 ^{+0.49} _{-0.68}	42.55 ^{+0.1} _{-0.1}	130 ± 44.4	80.7 ± 14.2	1,10,20
NGC 3783	3770 ⁺⁶⁸ ₋₆₈	1691 ⁺¹⁹ ₋₁₉	3093 ⁺⁵²⁹ ₋₅₂₉	1753 ⁺¹⁴¹ ₋₁₄₁	10.2 ^{+3.3} _{-2.3}	42.56 ^{+0.18} _{-0.18}	144 ± 83.7	126.5 ± 14.6	1,3,10
Z 186-18	1334 ⁺⁸⁰ ₋₈₀	785 ⁺²¹ ₋₂₁	1018 ⁺³³ ₋₃₃	1451 ⁺²³ ₋₂₃	24 ^{+8.4} _{-4.8}	42.67 ^{+0.11} _{-0.11}	114.6 ± 32.5	38.7 ± 8.6	1,17
UGC 06728	1642 ⁺¹⁶¹ ₋₁₆₁	715 ⁺¹⁹ ₋₁₉	1310 ⁺¹⁸² ₋₁₈₂	784 ⁺⁹² ₋₉₂	1.4 ^{+0.7} _{-0.8}	41.86 ^{+0.08} _{-0.08}	49.5 ± 10.8	33.8 ± 6.6	1,22
Mrk 1310	2409 ⁺²⁴ ₋₂₄	1209 ⁺⁴² ₋₄₂	1602 ⁺²⁵⁰ ₋₂₅₀	755 ⁺¹³⁸ ₋₁₃₈	3.66 ^{+0.59} _{-0.61}	42.29 ^{+0.14} _{-0.14}	94.3 ± 38.2	293.8 ± 84.8	1,10,20
NGC 4051	765 ⁺³ ₋₃	470 ⁺² ₋₂	941 ⁺¹⁷ ₋₁₉	493 ⁺³⁴ ₋₃₆	2.87 ^{+0.86} _{-1.33}	41.85 ^{+0.18} _{-0.18}	86.8 ± 51.7	79.2 ± 14.6	1,18
	799 ⁺² ₋₂	1045 ⁺⁴ ₋₄	927 ⁺⁶⁴ ₋₆₄	1034 ⁺⁴¹ ₋₄₁	1.87 ^{+0.54} _{-0.5}	41.96 ^{+0.19} _{-0.19}	71.7 ± 41.3	108.7 ± 7.5	1,10,21
	789 ⁺²² ₋₂₂	585 ⁺³²⁵ ₋₃₂₅	940 ⁺¹⁷ ₋₁₉	721 ⁺³⁷⁹ ₋₃₇₉	2.05 ^{+0.72} _{-0.73}	41.9 ^{+0.15} _{-0.15}	77.58 ± 33.91	102.54 ± 18.22	...
NGC 4151	6371 ⁺¹⁵⁰ ₋₁₅₀	2311 ⁺¹¹ ₋₁₁	4248 ⁺⁵¹⁶ ₋₅₁₆	1914 ⁺⁴² ₋₄₂	6.6 ^{+1.1} _{-0.8}	42.09 ^{+0.21} _{-0.21}	78.6 ± 34.3	104.6 ± 24.4	1,3,10
PG 1211+143	1918 ⁺⁹⁵ ₋₉₅	1499 ⁺⁴⁹ ₋₄₉	1358 ⁺¹⁴ ₋₁₁	697 ⁺¹⁸ ₋₁₉	53 ^{+5.1} _{-5.8}	44.64 ^{+0.02} _{-0.02}	116.42 ± 8.64	24.2 ± 2.97	2
	2012 ⁺³⁷ ₋₃₇	1487 ⁺³⁰ ₋₃₀	1317 ⁺¹³⁸ ₋₁₃₈	1080 ⁺¹⁰² ₋₁₀₂	93.8 ^{+33.85} _{-33.85}	44.73 ^{+0.08} _{-0.08}	100.2 ± 22.9	16.9 ± 3.2	1,3
	2000 ⁺⁵⁶ ₋₅₆	1490 ⁺²⁶ ₋₂₆	1358 ⁺¹⁵ ₋₁₂	709 ⁺⁹⁷ ₋₉₇	54.03 ^{+10.36} _{-10.71}	44.64 ^{+0.04} _{-0.04}	114.4 ± 11.08	20.82 ± 5.59	...
Mrk 202	1471 ⁺¹⁸ ₋₁₈	867 ⁺⁴⁰ ₋₄₀	1354 ⁺²⁵⁰ ₋₂₅₀	659 ⁺⁶⁵ ₋₆₅	3.05 ^{+1.73} _{-1.12}	42.26 ^{+0.14} _{-0.14}	70.6 ± 27.5	87.7 ± 25.8	1,10,20
NGC 4253	1609 ⁺³⁹ ₋₃₉	1088 ⁺³⁷ ₋₃₇	834 ⁺¹²⁶⁰ ₋₁₂₆₀	516 ⁺²¹⁸ ₋₂₁₈	6.16 ^{+1.63} _{-0.92}	42.57 ^{+0.12} _{-0.12}	81.1 ± 31.6	326.8 ± 37.5	1,10,20
Mrk 50	4101 ⁺⁵⁶ ₋₅₆	2024 ⁺³¹ ₋₃₁	3355 ⁺¹²⁸ ₋₁₂₈	2020 ⁺¹⁰³ ₋₁₀₃	10.64 ^{+0.82} _{-0.93}	42.75 ^{+0.07} _{-0.07}	137.55 ± 13.73	23.02 ± 2.82	33,34
PG 1226+023	3197 ⁺³⁹ ₋₃₉	1703 ⁺¹⁶ ₋₁₆	3305 ⁺⁴²⁰ ₋₄₂₀	1081 ⁺²³⁹ ₋₂₃₉	146.8 ^{+8.3} _{-12.1}	45.92 ^{+0.05} _{-0.05}	80.3 ± 10.3	10.7 ± 1.3	1,23
PG 1229+204	3828 ⁺⁵⁴ ₋₅₄	1608 ⁺²⁴ ₋₂₄	3414 ⁺³²⁰ ₋₃₂₀	1385 ⁺¹¹¹ ₋₁₁₁	37.8 ^{+27.6} _{-15.3}	43.7 ^{+0.05} _{-0.05}	209.7 ± 38.3	58.2 ± 6.1	1,3,10
NGC 4593	5143 ⁺¹⁶ ₋₁₆	1790 ⁺³ ₋₃	4141 ⁺⁴¹⁶ ₋₄₁₆	1561 ⁺⁵⁵ ₋₅₅	3.73 ^{+0.75} _{-0.75}	42.87 ^{+0.18} _{-0.18}	101.6 ± 59	30.5 ± 3.2	1,10,24
	4395 ⁺³⁶² ₋₃₆₂	4.33 ^{+1.32} _{-0.79}	42.38 ^{+0.18} _{-0.18}	115.4 ± 67.6	51.8 ± 5.8	25
	5142 ⁺⁴⁹ ₋₄₉	1790 ⁺³ ₋₃	4141 ⁺⁴¹⁶ ₋₄₁₆	1561 ⁺⁵⁵ ₋₅₅	3.93 ^{+0.78} _{-0.69}	42.62 ^{+0.37} _{-0.37}	107.57 ± 45.49	35.47 ± 13.05	...
IRAS F12397+3333	1802 ⁺⁵⁶⁰ ₋₅₆₀	1150 ⁺¹²² ₋₁₂₂	922 ⁺³⁴ ₋₃₂	1685 ⁺⁵⁰ ₋₁₅₀	9.7 ^{+5.5} _{-1.8}	44.23 ^{+0.05} _{-0.05}	54.2 ± 8.4	66.9 ± 6.8	1,17
NGC 4748	1947 ⁺⁶⁶ ₋₆₆	1009 ⁺²⁷ ₋₂₇	1212 ⁺¹⁷³ ₋₁₇₃	657 ⁺⁹¹ ₋₉₁	5.55 ^{+1.62} _{-2.22}	42.56 ^{+0.12} _{-0.12}	136.8 ± 50.1	300.3 ± 48.4	1,10,20
PG 1307+085	5059 ⁺¹³³ ₋₁₃₃	1963 ⁺⁴⁷ ₋₄₇	5058 ⁺⁵²⁴ ₋₅₂₄	1820 ⁺¹²² ₋₁₂₂	105.6 ⁺³⁶ _{-46.6}	44.85 ^{+0.02} _{-0.02}	98.4 ± 15.1	39 ± 2.2	1,3
PG 1310-108	3613 ⁺⁸¹² ₋₇₈₁	1978 ⁺⁸⁷ ₋₆₅	2425 ⁺¹⁵ ₋₁₉	1092 ⁺³⁶ ₋₅₄	12.8 ^{+1.7} _{-1.7}	43.33 ^{+0.05} _{-0.05}	138.84 ± 13.87	110.82 ± 8.62	2
MCG -6-30-15	1958 ⁺⁷⁵ ₋₇₅	976 ⁺⁸ ₋₈	1422 ⁺⁴¹⁶ ₋₄₁₆	664 ⁺⁸⁷ ₋₈₇	5.33 ^{+1.86} _{-1.75}	41.65 ^{+0.23} _{-0.23}	60 ± 36.6	104.9 ± 48.6	1,38
NGC 5273	5688 ⁺¹⁶³ ₋₁₆₃	1821 ⁺⁵³ ₋₅₃	4615 ⁺³³⁰ ₋₃₃₀	1544 ⁺⁹⁸ ₋₉₈	2.22 ^{+1.19} _{-1.61}	41.54 ^{+0.16} _{-0.16}	82.2 ± 37.1	46.5 ± 14.5	1,26
IC 4329A	6944 ⁺⁵¹ ₋₅₁	2247 ⁺⁸ ₋₈	4789 ⁺⁸⁶⁹ ₋₈₆₉	2112 ⁺⁹³ ₋₉₃	16.33 ^{+2.59} _{-2.28}	43.67 ^{+0.14} _{-0.14}	181.14 ± 20.38	158.71 ± 17.22	32
PG 1351+695	5297 ⁺¹⁰ ₋₁₀	1871 ⁺⁶ ₋₆	4478 ⁺³ ₋₃	1583 ⁺¹² ₋₁₀	19.9 ⁺¹ ₋₁	43.11 ^{+0.07} _{-0.07}	182.6 ± 47.36	199.97 ± 34.29	2
	5354 ⁺³² ₋₃₂	1823 ⁺¹¹ ₋₁₁	3385 ⁺³⁴⁹ ₋₃₄₉	1420 ⁺⁹⁶ ₋₉₆	16.7 ^{+3.9} _{-3.9}	43.71 ^{+0.07} _{-0.07}	132.2 ± 28.7	36.9 ± 5.3	1,3,4
	5302 ⁺²⁵ ₋₂₅	1860 ⁺²⁹ ₋₂₉	4478 ⁺¹⁴ ₋₁₄	1581 ⁺²⁹ ₋₂₈	19.7 ^{+1.46} _{-1.46}	43.4 ^{+0.43} _{-0.43}	145.74 ± 40	40.7 ± 35.2	...
PG 1351+640	7625 ⁺⁹⁵ ₋₈₁	3114 ⁺⁶⁵ ₋₅₀	2154 ⁺¹⁸ ₋₁₃	1527 ⁺²³ ₋₂₁	74.8 ^{+2.3} _{-2.3}	44.59 ^{+0.02} _{-0.02}	44.56 ± 7.9	56.61 ± 4.3	2
NGC 5548	4674 ⁺⁶³ ₋₆₃	1934 ⁺⁵ ₋₅	4044 ⁺¹⁹⁹ ₋₁₉₉	1687 ⁺⁵⁶ ₋₅₆	19.7 ^{+1.5} _{-1.5}	43.39 ^{+0.1} _{-0.1}	128.1 ± 40.3	89.1 ± 10	1,3,6
	5418 ⁺¹⁰⁷ ₋₁₀₇	2227 ⁺²⁰ ₋₂₀	4664 ⁺³²⁴ ₋₃₂₄	1882 ⁺⁸³ ₋₈₃	18.6 ^{+2.1} _{-2.3}	43.14 ^{+0.11} _{-0.11}	151.3 ± 57.9	156.9 ± 24.4	1,3,6
	5236 ⁺⁸⁷ ₋₈₇	2205 ⁺¹⁶ ₋₁₆	5776 ⁺²³⁷ ₋₂₃₇	2075 ⁺⁸¹ ₋₈₁	15.9 ^{+2.9} _{-2.5}	43.35 ^{+0.09} _{-0.09}	119.7 ± 37.9	97.3 ± 10.4	1,3,6
	5986 ⁺⁹⁵ ₋₉₅	3110 ⁺⁵³ ₋₅₃	5691 ⁺¹⁶⁴ ₋₁₆₄	2264 ⁺⁸⁸ ₋₈₈	11 ^{+1.9} ₋₂	43.07 ^{+0.11} _{-0.11}	144.5 ± 66.7	185.1 ± 31.2	1,3,6
	5930 ⁺⁴² ₋₄₂	2486 ⁺¹³ ₋₁₃	2543 ⁺⁶⁰⁵ ₋₆₀₅	1909 ⁺¹²⁹ ₋₁₂₉	13 ^{+1.6} _{-1.4}	43.32 ^{+0.1} _{-0.1}	135.9 ± 41.2	103.5 ± 11.3	1,3,6
	7378 ⁺³⁹ ₋₃₉	2877 ⁺¹⁷ ₋₁₇	7202 ⁺³⁹² ₋₃₉₂	2895 ⁺¹¹⁴ ₋₁₁₄	13.4 ^{+3.8} _{-4.3}	43.38 ^{+0.09} _{-0.09}	114.4 ± 37	91.4 ± 9.8	1,3,6
	6946 ⁺⁷⁹ ₋₇₉	2432 ⁺¹³ ₋₁₃	6142 ⁺²⁸⁹ ₋₂₈₉	2248 ⁺¹³⁴ ₋₁₃₄	21.7 ^{+2.6} _{-2.6}	43.52 ^{+0.09} _{-0.09}	102.4 ± 30.2	65.9 ± 5.1	1,3,6

Table 3 continued

Table 3 (continued)

Name	FWHM _{Hβ} ,mean (km s ⁻¹)	σ _{Hβ} ,mean (km s ⁻¹)	FWHM _{Hβ} ,rms (km s ⁻¹)	σ _{Hβ} ,rms (km s ⁻¹)	τ _{Hβ} (days)	log L ₅₁₀₀ (erg s ⁻¹)	EW(H β) (Å)	EW([O III]) (erg s ⁻¹)	References
	6623 ⁺⁹³ ₋₉₃	2276 ⁺¹⁵ ₋₁₅	5706 ⁺³⁵⁷ ₋₃₅₇	2026 ⁺⁶⁸ ₋₆₈	16.4 ^{+1.2} _{-1.1}	43.43 ^{+0.09} _{-0.09}	106.3 ± 33.3	80.7 ± 7.7	1,3,6
	6298 ⁺⁶⁵ ₋₆₅	2178 ⁺¹² ₋₁₂	5541 ⁺³⁵⁴ ₋₃₅₄	1923 ⁺⁶² ₋₆₂	17.5 ⁺² _{-1.6}	43.24 ^{+0.1} _{-0.1}	153.5 ± 50.7	125.8 ± 15.3	1,3,6
	6177 ⁺³⁶ ₋₃₆	2035 ⁺¹¹ ₋₁₁	4596 ⁺⁵⁰⁵ ₋₅₀₅	1732 ⁺⁷⁶ ₋₇₆	26.5 ^{+4.3} _{-2.2}	43.59 ^{+0.09} _{-0.09}	98.1 ± 30	56.5 ± 4.8	1,3,6
	6247 ⁺⁵⁷ ₋₅₇	2021 ⁺¹⁸ ₋₁₈	6377 ⁺¹⁴⁷ ₋₁₄₇	1980 ⁺³⁰ ₋₃₀	24.8 ^{+3.2} ₋₃	43.51 ^{+0.09} _{-0.09}	106.6 ± 31.5	68 ± 6	1,3,6
	6240 ⁺⁷⁷ ₋₇₇	2010 ⁺³⁰ ₋₃₀	5957 ⁺²²⁴ ₋₂₂₄	1969 ⁺⁴⁸ ₋₄₈	6.5 ^{+5.7} _{-3.7}	43.11 ^{+0.11} _{-0.11}	172.8 ± 66.1	170.1 ± 26.8	1,3,6
	6478 ⁺¹⁰⁸ ₋₁₀₈	3111 ⁺¹³¹ ₋₁₃₁	6247 ⁺³⁴³ ₋₃₄₃	2173 ⁺⁸⁹ ₋₈₉	14.3 ^{+5.9} _{-7.3}	43.11 ^{+0.11} _{-0.11}	139.8 ± 55.7	167.5 ± 27	1,3,6
	6396 ⁺¹⁶⁷ ₋₁₆₇	2662 ⁺⁵³² ₋₅₃₂	6.3 ^{+2.6} _{-2.3}	42.96 ^{+0.13} _{-0.13}	74.4 ± 27.3	240 ± 53.5	1,5,27
	12771 ⁺⁷¹ ₋₇₁	4266 ⁺⁶⁵ ₋₆₅	11177 ⁺²²⁶⁶ ₋₂₂₆₆	4270 ⁺²⁹² ₋₂₉₂	4.18 ^{+0.86} _{-1.3}	43.01 ^{+0.11} _{-0.11}	105.3 ± 35.4	211.4 ± 32.6	1,5,20
	11481 ⁺⁵⁷⁴ ₋₅₇₄	4212 ⁺²¹¹ ₋₂₁₁	4849 ⁺¹¹² ₋₁₁₂	1822 ⁺³⁵ ₋₃₅	12.4 ^{+2.74} _{-3.85}	42.99 ^{+0.11} _{-0.11}	96.6 ± 34.4	220.3 ± 40	1,5,21
	9912 ⁺³⁶² ₋₃₆₂	3350 ⁺²⁷² ₋₂₇₂	9450 ⁺²⁹⁰ ₋₂₉₀	3124 ⁺³⁰² ₋₃₀₂	7.2 ^{+1.33} _{-0.35}	43.21 ^{+0.09} _{-0.09}	160.1 ± 46.2	107.7 ± 7.8	1,28
	9496 ⁺⁴¹⁸ ₋₄₁₈	3691 ⁺¹⁶² ₋₁₆₂	10161 ⁺⁵⁸⁷ ₋₅₈₇	4278 ⁺⁶⁷¹ ₋₆₇₁	4.17 ^{+0.36} _{-0.36}	43.45 ^{+0.09} _{-0.09}	91.2 ± 26.3	64.4 ± 4.5	1,29
	6615⁺¹⁶⁴²₋₁₆₄₂	2134⁺²⁸⁷₋₂₈₇	5641⁺¹²⁵¹₋₁₂₅₁	1959⁺²⁴⁶₋₂₄₆	7.46^{+5.69}_{-5.68}	43.3^{+0.19}_{-0.19}	110.19 ± 25.61	77.1 ± 26.32	...
PG 1426+015	7113⁺¹⁶⁰₋₁₆₀	2906⁺⁸⁰₋₈₀	6323⁺¹²⁹⁵₋₁₂₉₅	3442⁺³⁰⁸₋₃₀₈	95^{+29.9}_{-37.1}	44.63^{+0.02}_{-0.02}	80.1 ± 9.2	19.2 ± 1.2	1,3,10
Mrk 817	4711 ⁺⁴⁹ ₋₄₉	1984 ⁺⁸ ₋₈	3515 ⁺³⁹³ ₋₃₉₃	1392 ⁺⁷⁸ ₋₇₈	19 ^{+3.9} _{-3.7}	43.79 ^{+0.05} _{-0.05}	98 ± 16.5	28.2 ± 1.5	1,3,10
	5237 ⁺⁶⁷ ₋₆₇	2098 ⁺¹³ ₋₁₃	4952 ⁺⁵³⁷ ₋₅₃₇	1971 ⁺⁹⁶ ₋₉₆	15.3 ^{+3.7} _{-3.5}	43.67 ^{+0.05} _{-0.05}	108.5 ± 20.4	37 ± 1.9	1,3,10
	4767 ⁺⁷² ₋₇₂	2195 ⁺¹⁶ ₋₁₆	3752 ⁺⁹⁹⁵ ₋₉₉₅	1729 ⁺¹⁵⁸ ₋₁₅₈	33.6 ^{+6.5} _{-7.7}	43.67 ^{+0.05} _{-0.05}	91.1 ± 15.3	36.9 ± 1.9	1,3,10
	5627 ⁺³⁰ ₋₃₀	2025 ⁺⁵ ₋₅	14.04 ^{+3.41} _{-3.47}	43.84 ^{+0.05} _{-0.05}	43.2 ± 7.1	24.8 ± 1.4	21
	4867⁺²⁸⁰₋₂₈₀	2040⁺⁹⁶₋₉₆	5611⁺²⁰²₋₂₀₂	2022⁺⁴⁸₋₄₈	17.36^{+6.32}_{-6.31}	43.74^{+0.09}_{-0.09}	61.85 ± 30.7	30.26 ± 6.14	...
PG 1440+356	1868⁺⁴⁸₋₄₈	1043⁺¹²₋₁₂	2032⁺⁵¹₋₅₁	715⁺³⁷₋₃₇	34.5^{+10.8}_{-12.4}	44.39^{+0.02}_{-0.02}	69.34 ± 5.49	15.28 ± 2.72	8
PG 1448+273	1323⁺¹³⁹₋₁₃₉	1043⁺⁷⁰₋₇₀	893⁺¹⁰⁴₋₁₀₄	631⁺³⁹₋₃₉	30.1^{+10.7}_{-5.9}	44.07^{+0.04}_{-0.04}	74.38 ± 8.34	47 ± 5.05	8
Mrk 1511	4171⁺¹³⁷₋₁₃₇	5.89^{+0.93}_{-0.58}	43.16^{+0.06}_{-0.06}	115.5 ± 23.1	36.4 ± 4.1	25
PG 1534+580	4217 ⁺⁷⁵¹ ₋₁₅₅	3180 ⁺⁸⁴ ₋₄₇	2362 ⁺¹¹ ₋₇	1142 ⁺²⁰ ₋₂₀	25.4 ⁺² _{-1.4}	43.48 ^{+0.05} _{-0.05}	118.4 ± 15.01	84.66 ± 8.01	2
	4543 ⁺²²⁷ ₋₂₂₇	1769 ⁺⁸⁸ ₋₈₈	4270 ⁺¹⁵⁷ ₋₁₅₇	1609 ⁺⁴⁷ ₋₄₇	8.72 ^{+1.2} _{-1.2}	43.17 ^{+0.06} _{-0.06}	153 ± 29	150.6 ± 13.2	1,3,5,21
	4478⁺³⁰⁰₋₂₆₁	2677⁺⁹⁵⁸₋₉₅₇	2368⁺¹⁵⁵₋₁₅₄	1214⁺²³⁹₋₂₃₉	13.64^{+10.81}_{-10.79}	43.35^{+0.22}_{-0.22}	125.71 ± 24.02	102.41 ± 41.92	...
PG 1535+547	2004 ⁺⁴² ₋₄₂	1311 ⁺¹⁶ ₋₁₆	1737 ⁺³³⁷ ₋₃₃₇	845 ⁺²⁰⁷ ₋₂₀₇	25.9 ^{+6.1} ₋₅	43.87 ^{+0.04} _{-0.04}	123.87 ± 7.26	14.77 ± 2.48	8
	1942 ⁺⁶⁷ ₋₆₇	1296 ⁺²³ ₋₂₃	1752 ⁺¹² ₋₁₂	1226 ⁺¹¹ ₋₁₁	23.7 ^{+7.5} _{-12.7}	43.69 ^{+0.05} _{-0.05}	135.9 ± 20.3	22.3 ± 1.8	1,9
	1987⁺⁵³₋₅₃	1306⁺¹⁶₋₁₆	1752⁺¹²₋₁₂	1225⁺²⁹₋₂₉	24.71^{+5.17}_{-3.13}	43.8^{+0.13}_{-0.13}	125.23 ± 8.71	19.71 ± 5.27	...
Mrk 493	778⁺¹²₋₁₂	513⁺⁵₋₅	2174⁺⁵³₋₂₀	1419⁺¹²¹₋₁₄₇	11.6^{+1.2}_{-2.6}	43.11^{+0.08}_{-0.08}	153 ± 29	150.6 ± 13.2	1,17
PG 1613+658	10269 ⁺⁷⁷³ ₋₁₆₇	3927 ⁺¹³ ₋₁₆	6762 ⁺⁹ ₋₁₀	3504 ⁺¹³ ₋₁₄	52.4 ^{+3.4} _{-2.8}	44.6 ^{+0.02} _{-0.02}	152.31 ± 8.24	35.17 ± 2.4	2
	9074 ⁺¹⁰³ ₋₁₀₃	3084 ⁺³³ ₋₃₃	7897 ⁺¹⁷⁹² ₋₁₇₉₂	2547 ⁺³⁴² ₋₃₄₂	40.1 ⁺¹⁵ _{-15.2}	44.77 ^{+0.02} _{-0.02}	86.7 ± 7.6	33.7 ± 2.2	3,6
	9129⁺³⁶⁹₋₃₆₇	3789⁺⁴⁴²₋₄₄₂	6762⁺¹²₋₁₃	3503⁺⁵⁵₋₅₅	51.9^{+4.77}_{-4.4}	44.68^{+0.12}_{-0.12}	116.87 ± 46.58	34.37 ± 1.93	...
PG 1617+175	4807 ⁺⁴⁶ ₋₄₆	2511 ⁺³ ₋₃	2392 ⁺¹⁸⁷ ₋₁₈₇	1288 ⁺³⁷⁴ ₋₃₇₄	34.3 ^{+6.8} _{-3.8}	44.52 ^{+0.02} _{-0.02}	119.62 ± 9.9	34.48 ± 11.39	8
	6641 ⁺¹⁹⁰ ₋₁₉₀	2313 ⁺⁶⁹ ₋₆₉	4718 ⁺⁹⁹¹ ₋₉₉₁	2626 ⁺²¹¹ ₋₂₁₁	71.5 ^{+29.6} _{-33.7}	44.39 ^{+0.02} _{-0.02}	114.8 ± 15.1	14.2 ± 0.8	1,3,10
	4908⁺⁵⁹⁴₋₅₉₄	2511⁺¹³₋₁₃	2472⁺⁶²⁷₋₆₂₇	2303⁺⁸³⁰₋₈₃₀	35.31^{+10.86}_{-9.38}	44.47^{+0.09}_{-0.09}	118.17 ± 8.85	14.3 ± 2.16	...
PG 1626+554	4318⁺⁹⁵₋₉₅	2350⁺¹¹₋₁₁	2784⁺¹⁸⁰₋₁₈₀	1719⁺¹¹⁹₋₁₁₉	77.1^{+5.5}_{-2.6}	44.62^{+0.02}_{-0.02}	122.4 ± 10.11	11.46 ± 2.77	8
PG 1700+518	2252⁺⁸⁵₋₈₅	3160⁺⁹³₋₉₃	1846⁺⁶⁸²₋₆₈₂	1700⁺¹²³₋₁₂₃	251.8^{+45.9}_{-38.8}	45.59^{+0.01}_{-0.01}	78.9 ± 4.5	3.7 ± 0.2	1,3,10
3C 382	7652⁺³⁸³₋₃₈₃	2969⁺⁷₋₇	11549⁺¹²⁹²₋₆₆₇	4552⁺²¹⁴₋₁₆₃	40.49^{+8.02}_{-3.74}	43.84^{+0.1}_{-0.1}	259.3 ± 64	61.4 ± 13.9	1,18
3C 390.3	12694 ⁺¹³ ₋₁₃	3744 ⁺⁴² ₋₄₂	9958 ⁺¹⁰⁴⁶ ₋₁₀₄₆	3105 ⁺⁸¹ ₋₈₁	23.6 ^{+6.2} _{-6.7}	43.68 ^{+0.1} _{-0.1}	206.2 ± 50.7	169.1 ± 36.9	1,3,10
	13211 ⁺²⁸ ₋₂₈	5377 ⁺³⁷ ₋₃₇	10872 ⁺¹⁶⁷⁰ ₋₁₆₇₀	5455 ⁺²⁷⁸ ₋₂₇₈	46.4 ^{+3.6} _{-3.2}	44.5 ^{+0.03} _{-0.03}	97.1 ± 10	30.5 ± 0.8	1,30
	12791⁺²⁸⁶₋₂₈₆	4670⁺¹¹⁴⁵₋₁₁₄₅	10215⁺¹⁰⁶⁰₋₁₀₆₀	3290⁺⁸⁹⁸₋₈₉₈	41.44^{+13.66}_{-13.61}	44.43^{+0.32}_{-0.32}	101.19 ± 30.89	30.57 ± 4.32	...
Zw 229-015	3350⁺⁷²₋₇₂	1640⁺¹⁶₋₁₆	2260⁺⁶⁵₋₆₅	1590⁺⁴⁷₋₄₇	3.97^{+0.71}_{-0.93}	42.4^{+0.1}_{-0.1}	192.99 ± 36.31	196.08 ± 36.34	35
NGC 6814	3323⁺⁷₋₇	1918⁺³⁶₋₃₆	3277⁺²⁹⁷₋₂₉₇	1610⁺¹⁰⁸₋₁₀₈	6.64^{+0.87}_{-0.9}	42.12^{+0.28}_{-0.28}	121.6 ± 112.2	69.8 ± 10	1,10,20
Mrk 509	3015⁺²₋₂	1554⁺⁷₋₇	2715⁺¹⁰¹₋₁₀₁	1276⁺²⁸₋₂₈	79.6^{+5.75}_{-5.75}	44.19^{+0.05}_{-0.05}	132.7 ± 19.1	77.7 ± 5.2	1,3
PG 2130+099	2101 ⁺¹⁰⁰ ₋₁₀₀	1437 ⁺⁶⁴ ₋₆₄	2447 ⁺⁷³ ₋₇₃	1272 ⁺⁹⁷ ₋₉₇	22.6 ^{+2.7} _{-3.6}	44.39 ^{+0.03} _{-0.03}	126.38 ± 7.96	25.75 ± 2.84	12
	2072 ⁺¹⁰⁷ ₋₁₀₇	1438 ⁺⁴¹ ₋₄₁	2054 ⁺⁵⁵⁷ ₋₅₅₇	874 ⁺²³⁷ ₋₂₃₇	27.8 ^{+2.9} _{-2.9}	44.41 ^{+0.03} _{-0.03}	128.18 ± 7.93	25.24 ± 2.83	12
	2087⁺⁷⁶₋₇₆	1438⁺³⁵₋₃₅	2440⁺¹⁰²₋₁₀₂	1215⁺²¹⁷₋₂₁₇	25.41^{+4.17}_{-4.32}	44.4^{+0.02}_{-0.02}	127.29 ± 5.76	25.5 ± 2.04	...
NGC 7469	4369⁺⁶₋₆	1095⁺⁵₋₅	1066⁺⁸⁴₋₈₄	1274⁺¹²⁶₋₁₂₆	10.9^{+3.5}_{-1.3}	43.51^{+0.11}_{-0.11}	63 ± 21	77.4 ± 10.8	31

Table 3 continued

Table 3 (continued)

Name	FWHM _{Hβ} ,mean	$\sigma_{H\beta}$,mean	FWHM _{Hβ} ,rms	$\sigma_{H\beta}$,rms	$\tau_{H\beta}$	log L_{5100}	EW(H β)	EW([O III])	References
	(km s ⁻¹)	(km s ⁻¹)	(km s ⁻¹)	(km s ⁻¹)	(days)	(erg s ⁻¹)	(Å)	(erg s ⁻¹)	

NOTE—References: (1) Du & Wang (2019), (2) Bao et al. (2022), (3) Collin et al. (2006), (4) Santos-Lleó et al. (2001), (5) Yu et al. (2020), (6) Kaspi et al. (2005), (7) Grier et al. (2012), (8) Hu et al. (2021), (9) Hu et al. (2015), (10) Bentz et al. (2013), (11) Hu et al. (2020), (12) Hu et al. (2020), (13) Li et al. (2021), (14) Du et al. (2018), (15) Peterson et al. (2004), (16) Santos-Lleó et al. (1997), (17) Du et al. (2015), (18) Fausnaugh et al. (2017), (19) Kaspi et al. (2000), (20) Bentz et al. (2009), (21) Denney et al. (2010), (22) Bentz et al. (2016), (23) Zhang et al. (2019), (24) Denney et al. (2006), (25) Barth et al. (2013), (26) Bentz et al. (2014), (27) Bentz et al. (2007), (28) Lu et al. (2016), (29) Pei et al. (2017), (30) Dietrich et al. (2012), (31) Peterson et al. (2014), (32) Bentz et al. (2023), (33) Barth et al. (2015), (34) Barth et al. (2011), (35) Barth et al. (2011), (36) De Rosa et al. (2018), (37) Huang et al. (2019), (38) Hu et al. (2016), (39) Brotherton et al. (2020), (40) Du et al. (2018)

Table 4. Spectral Properties

Name	\mathcal{R}_{Fe}	FHWM _{Fe II} /FWHM _{Hβ}	\mathcal{A}	EW(He II)
				(Å)
PG 0007+106	0.48	1.32 ± 0.25	-0.052 ± 0.054	too weak
I Zw1	1.71	0.84 ± 0.06	0.059 ± 0.034	6.53 ± 1.2
Mrk 6	0.51	1.12 ± 0.67	-0.292 ± 0.019	too weak
Mrk 704	0.55	1.56 ± 0.7	0.012 ± 0.007	24.26 ± 7.92
PG 0923+201	0.94	0.96 ± 0.46	0 ± 0.001	too weak
PG 0923+129	0.59	0.86 ± 0.41	0.007 ± 0.015	25.1 ± 12.19
PG 1100+772	0.05	0.68 ± 5.74	-0.025 ± 0.006	4.91 ± 5.15
Mrk 50	0.13	0.52 ± 1.23	0.035 ± 0.003	21.6 ± 10.6
PG 1310-108	0.34	0.86 ± 0.62	-0.076 ± 0.018	36.53 ± 11
IC 4329A	0.85	1.43 ± 0.16	0.025 ± 0.004	40.61 ± 6.76
PG 1351+640	0.36	1.13 ± 1.81	-0.045 ± 0.012	5.24 ± 6.24
PG 1440+356	1.4	0.81 ± 0.18	0.024 ± 0.003	3.68 ± 5.95
PG 1448+273	0.98	0.96 ± 0.39	0.012 ± 0.006	18.64 ± 7.63
PG 1626+554	0.01	0.4 ± 0.01	0.018 ± 0.002	11.51 ± 5.85
Zw 229-015	0.39	0.55 ± 0.18	0.175 ± 0.092	12.55 ± 6.18

NOTE—Most of the spectral properties utilized in this paper are from Du & Wang (2019). Here, we only list the additional objects included in this study.

REFERENCES

- Abuter, R., Allouche, F., Amorim, A., et al. 2024, *Nature*, 627, 281. doi:10.1038/s41586-024-07053-4
- Bahcall, J. N., Kozlovsky, B.-Z., & Salpeter, E. E. 1972, *ApJ*, 171, 467. doi:10.1086/151300
- Bao, D.-W., Brotherton, M. S., Du, P., et al. 2022, *ApJS*, 262, 14. doi:10.3847/1538-4365/ac7beb
- Barth, A. J., Pancoast, A., Thorman, S. J., et al. 2011, *ApJL*, 743, L4. doi:10.1088/2041-8205/743/1/L4
- Barth, A. J., Nguyen, M. L., Malkan, M. A., et al. 2011, *ApJ*, 732, 121. doi:10.1088/0004-637X/732/2/121
- Barth, A. J., Pancoast, A., Bennert, V. N., et al. 2013, *ApJ*, 769, 128. doi:10.1088/0004-637X/769/2/128
- Barth, A. J., Bennert, V. N., Canalizo, G., et al. 2015, *ApJS*, 217, 26. doi:10.1088/0067-0049/217/2/26
- Bennert, V. N., Treu, T., Woo, J.-H., et al. 2010, *ApJ*, 708, 1507. doi:10.1088/0004-637X/708/2/1507
- Bentz, M. C. & Manne-Nicholas, E. 2018, *ApJ*, 864, 146. doi:10.3847/1538-4357/aad808
- Bentz, M. C., Denney, K. D., Cackett, E. M., et al. 2007, *ApJ*, 662, 205. doi:10.1086/516724

Table 5. Joint Fitting and Calibrations of Virial Factors

VP	Param.	CB			PB			PB+CB		
		Approach I	Approach II	Approach III	Approach I	Approach II	Approach III	Approach I	Approach II	Approach III
MF	α	0.96±0.09	1.46±0.05	[1.02]	[0.96]	[1.46]	[1.02]	1.11±0.08	1.48±0.03	[1.27]
MF	β	-1.35±0.9	-6.49±0.53	[-1.9]	-2.26±0.14	-7±0.07	[-2.76]	-3.05±0.78	-6.83±0.33	[-4.67]
MF	f	3.31±0.85	2.79±0.36	3.24±0.2	0.67±0.28	0.58±0.11	0.62±0.03	2.16±0.53	1.58±0.17	1.93±0.09
MF	ϵ	0.48	0.58	0.58
MS	α	0.98±0.08	1.24±0.04	[1.02]	[0.98]	[1.24]	[1.02]	1.11±0.07	1.35±0.03	[1.27]
MS	β	-1.5±0.84	-4.26±0.43	[-1.9]	-2.4±0.13	-4.95±0.06	[-2.76]	-3.03±0.73	-5.52±0.31	[-4.67]
MS	f	12.73±3.05	11.26±1.27	12.63±0.75	2.22±0.86	2.08±0.33	2.14±0.13	7.81±1.82	6.45±0.63	6.99±0.33
MS	ϵ	0.44	0.53	0.54
RF	α	1.03±0.09	1.34±0.04	[1.02]	[1.03]	[1.34]	[1.02]	1.13±0.08	1.37±0.03	[1.27]
RF	β	-2.03±0.94	-5.27±0.46	[-1.9]	-2.89±0.15	-5.88±0.07	[-2.76]	-3.26±0.79	-5.76±0.32	[-4.67]
RF	f	5.42±1.45	4.61±0.57	5.46±0.34	0.91±0.4	0.54±0.09	0.58±0.04	3.27±0.82	2.08±0.21	2.33±0.12
RF	ϵ	0.49	0.59	0.58
RS	α	1.03±0.08	1.3±0.04	[1.02]	[1.03]	[1.3]	[1.02]	1.1±0.07	1.28±0.03	[1.27]
RS	β	-2.03±0.85	-4.82±0.45	[-1.9]	-2.89±0.13	-5.47±0.07	[-2.76]	-2.95±0.73	-4.82±0.3	[-4.67]
RS	f	20.28±4.9	19.55±2.34	22.4±1.42	2.4±0.93	1.99±0.33	2.17±0.14	10.62±2.47	8.86±0.85	9.12±0.46
RS	ϵ	0.43	0.52	0.53

NOTE— The slopes of the joint fitting for PB samples are fixed to those of the CB results, and marked with square brackets. α and β are the slope and intercept of the joint fitting of the $M_{\bullet} - L_{V, \text{bul}}$ relation. f is the virial factor. ϵ is the intrinsic error. The slope and intercept of Approach III are obtained by the quiescent galaxies in Kormendy & Ho (2013).

Table 6. Linear Regression of Correlations between Virial factors and Spectral properties

VP	Param.	CB			PB			PB+CB		
		α'	β'	ϵ'	α'	β'	ϵ'	α'	β'	ϵ'
MF	$\mathcal{D}_{H\beta, \text{mean}}$	-0.61 ± 0.11	1.76 ± 0.23	0.31	-0.82 ± 0.19	1.31 ± 0.34	0.45	-0.53 ± 0.13	1.25 ± 0.27	0.56
	\mathcal{R}_{Fe}	1.17 ± 0.28	-1.11 ± 0.23	0.45
	$\log(\text{FWHM}_{H\beta, \text{mean}}/\text{km s}^{-1})$	-1.42 ± 0.26	5.66 ± 0.94	0.32	-1.82 ± 0.33	5.95 ± 1.12	0.4
	$\log(\sigma_{H\beta, \text{mean}}/\text{km s}^{-1})$	-1.96 ± 0.51	5.94 ± 1.59	0.48
MS	$\log(\sigma_{H\beta, \text{mean}}/\text{km s}^{-1})$	-1.65 ± 0.48	5.48 ± 1.51	0.42
RF	$\mathcal{D}_{H\beta, \text{mean}}$	-0.59 ± 0.13	1.91 ± 0.27	0.4
	$\mathcal{D}_{H\beta, \text{rms}}$	-0.66 ± 0.11	2.08 ± 0.24	0.33
	$\log(\text{FWHM}_{H\beta, \text{mean}}/\text{km s}^{-1})$	-1.55 ± 0.28	6.36 ± 1.02	0.35
	$\log(\text{FWHM}_{H\beta, \text{rms}}/\text{km s}^{-1})$	-1.29 ± 0.21	5.27 ± 0.76	0.33	-2.03 ± 0.33	6.67 ± 1.11	0.39
	$\log(\sigma_{H\beta, \text{rms}}/\text{km s}^{-1})$	-1.15 ± 0.36	4.44 ± 1.17	0.44	-2.3 ± 0.7	6.99 ± 2.16	0.47

Bentz, M. C., Peterson, B. M., Netzer, H., et al. 2009, ApJ, 697, 160. doi:10.1088/0004-637X/697/1/160

Bentz, M. C., Walsh, J. L., Barth, A. J., et al. 2009, ApJ, 705, 199. doi:10.1088/0004-637X/705/1/199

Bentz, M. C., Denney, K. D., Grier, C. J., et al. 2013, ApJ, 767, 149. doi:10.1088/0004-637X/767/2/149

Bentz, M. C., Horenstein, D., Bazhaw, C., et al. 2014, ApJ, 796, 8. doi:10.1088/0004-637X/796/1/8

Bentz, M. C., Batista, M., Seals, J., et al. 2016, ApJ, 831, 2. doi:10.3847/0004-637X/831/1/2

Bentz, M. C., Onken, C. A., Street, R., et al. 2023, ApJ, 944, 29. doi:10.3847/1538-4357/acab62

Bentz, M. C. 2021, ApJ, 908, 25. doi:10.3847/1538-4357/abceca

Blandford, R. D. & McKee, C. F. 1982, ApJ, 255, 419. doi:10.1086/159843

- Boroson, T. A. & Green, R. F. 1992, *ApJS*, 80, 109.
doi:10.1086/191661
- Brotherton, M. S., Du, P., Xiao, M., et al. 2020, *ApJ*, 905, 77. doi:10.3847/1538-4357/abc2d2
- Collin, S., Kawaguchi, T., Peterson, B. M., et al. 2006, *A&A*, 456, 75. doi:10.1051/0004-6361:20064878
- Contini, T., Considere, S., & Davoust, E. 1998, *A&AS*, 130, 285. doi:10.1051/aas:1998412
- De Robertis, M. 1985, *ApJ*, 289, 67. doi:10.1086/162865
- De Rosa, G., Fausnaugh, M. M., Grier, C. J., et al. 2018, *ApJ*, 866, 133. doi:10.3847/1538-4357/aadd11
- de Vaucouleurs, G., de Vaucouleurs, A., Corwin, H. G., et al. 1991, *Third Reference Catalogue of Bright Galaxies*.
- Denney, K. D., Bentz, M. C., Peterson, B. M., et al. 2006, *ApJ*, 653, 152. doi:10.1086/508533
- Denney, K. D., Peterson, B. M., Pogge, R. W., et al. 2010, *ApJ*, 721, 715. doi:10.1088/0004-637X/721/1/715
- Deo, R. P., Crenshaw, D. M., & Kraemer, S. B. 2006, *AJ*, 132, 321. doi:10.1086/504894
- Dietrich, M., Peterson, B. M., Grier, C. J., et al. 2012, *ApJ*, 757, 53. doi:10.1088/0004-637X/757/1/53
- Ding, X., Onoue, M., Silverman, J. D., et al. 2023, *Nature*, 621, 51. doi:10.1038/s41586-023-06345-5
- Du, P. & Wang, J.-M. 2019, *ApJ*, 886, 42.
doi:10.3847/1538-4357/ab4908
- Du, P., Hu, C., Lu, K.-X., et al. 2014, *ApJ*, 782, 45.
doi:10.1088/0004-637X/782/1/45
- Du, P., Hu, C., Lu, K.-X., et al. 2015, *ApJ*, 806, 22.
doi:10.1088/0004-637X/806/1/22
- Du, P., Wang, J.-M., Hu, C., et al. 2016, *ApJL*, 818, L14.
doi:10.3847/2041-8205/818/1/L14
- Du, P., Lu, K.-X., Zhang, Z.-X., et al. 2016, *ApJ*, 825, 126.
doi:10.3847/0004-637X/825/2/126
- Du, P., Zhang, Z.-X., Wang, K., et al. 2018, *ApJ*, 856, 6.
doi:10.3847/1538-4357/aae6b
- Du, P., Brotherton, M. S., Wang, K., et al. 2018, *ApJ*, 869, 142. doi:10.3847/1538-4357/aaed2c
- Du, P. 2024, *DASpec: A code for spectral decomposition of active galactic nuclei, v0.8*, Zenodo,
doi:10.5281/zenodo.12578529
- Farina, E. P., Schindler, J.-T., Walter, F., et al. 2022, *ApJ*, 941, 106. doi:10.3847/1538-4357/ac9626
- Fausnaugh, M. M., Grier, C. J., Bentz, M. C., et al. 2017, *ApJ*, 840, 97. doi:10.3847/1538-4357/aa6d52
- Fisher, D. B. & Drory, N. 2008, *AJ*, 136, 773.
doi:10.1088/0004-6256/136/2/773
- GRAVITY Collaboration, Amorim, A., Bauböck, M., et al. 2020, *A&A*, 643, A154. doi:10.1051/0004-6361/202039067
- GRAVITY Collaboration, Amorim, A., Bauböck, M., et al. 2021, *A&A*, 648, A117. doi:10.1051/0004-6361/202040061
- Gadotti, D. A. 2009, *MNRAS*, 393, 1531.
doi:10.1111/j.1365-2966.2008.14257.x
- Gennaro, M. 2018, *WFC3 Data Handbook v. 4*, 4
- Gonzaga, S., Biretta, J., et al. 2010, *HST WFPC2 Data Handbook, v. 5.0*, ed., Baltimore, STScI
- Gonzaga, S., Hack, W., Fruchter, A., et al. 2012, *The DrizzlePac Handbook, HST Data Handbook*
- Goulding, A. D., Greene, J. E., Setton, D. J., et al. 2023, *ApJL*, 955, L24. doi:10.3847/2041-8213/acf7c5
- Graham, A. W., Onken, C. A., Athanassoula, E., et al. 2011, *MNRAS*, 412, 2211.
doi:10.1111/j.1365-2966.2010.18045.x
- Gravity Collaboration, Sturm, E., Dexter, J., et al. 2018, *Nature*, 563, 657. doi:10.1038/s41586-018-0731-9
- Grier, C. J., Peterson, B. M., Pogge, R. W., et al. 2012, *ApJ*, 755, 60. doi:10.1088/0004-637X/755/1/60
- Grier, C. J., Martini, P., Watson, L. C., et al. 2013, *ApJ*, 773, 90. doi:10.1088/0004-637X/773/2/90
- Grier, C. J., Pancoast, A., Barth, A. J., et al. 2017, *ApJ*, 849, 146. doi:10.3847/1538-4357/aa901b
- Guyon, O., Sanders, D. B., & Stockton, A. N. 2006, *NewAR*, 50, 748. doi:10.1016/j.newar.2006.06.086
- Harikane, Y., Zhang, Y., Nakajima, K., et al. 2023, *ApJ*, 959, 39. doi:10.3847/1538-4357/ad029e
- Hamilton, T. S., Casertano, S., & Turnshek, D. A. 2008, *ApJ*, 678, 22. doi:10.1086/524182
- Ho, L. C. & Kim, M. 2014, *ApJ*, 789, 17.
doi:10.1088/0004-637X/789/1/17
- Hu, C., Du, P., Lu, K.-X., et al. 2015, *ApJ*, 804, 138.
doi:10.1088/0004-637X/804/2/138
- Hu, C., Wang, J.-M., Ho, L. C., et al. 2016, *ApJ*, 832, 197.
doi:10.3847/0004-637X/832/2/197
- Hu, C., Li, S.-S., Guo, W.-J., et al. 2020, *ApJ*, 905, 75.
doi:10.3847/1538-4357/abc2da
- Hu, C., Li, Y.-R., Du, P., et al. 2020, *ApJ*, 890, 71.
doi:10.3847/1538-4357/ab6a17
- Hu, C., Li, S.-S., Yang, S., et al. 2021, *ApJS*, 253, 20.
doi:10.3847/1538-4365/abd774
- Huang, Y.-K., Hu, C., Zhao, Y.-L., et al. 2019, *ApJ*, 876, 102. doi:10.3847/1538-4357/ab16ef
- Izumi, T., Onoue, M., Matsuoka, Y., et al. 2019, *PASJ*, 71, 111. doi:10.1093/pasj/psz096
- Izumi, T., Matsuoka, Y., Fujimoto, S., et al. 2021, *ApJ*, 914, 36. doi:10.3847/1538-4357/abf6dc
- Kaspi, S., Smith, P. S., Netzer, H., et al. 2000, *ApJ*, 533, 631. doi:10.1086/308704
- Kaspi, S., Maoz, D., Netzer, H., et al. 2005, *ApJ*, 629, 61.
doi:10.1086/431275

- Khorunzhev, G. A., Sazonov, S. Y., Burenin, R. A., et al. 2012, *Astronomy Letters*, 38, 475. doi:10.1134/S1063773712080026
- Kim, M., Ho, L. C., Peng, C. Y., et al. 2008, *ApJS*, 179, 283. doi:10.1086/591796
- Kim, M., Ho, L. C., Peng, C. Y., et al. 2017, *ApJS*, 232, 21. doi:10.3847/1538-4365/aa8a75
- Kinney, A. L., Calzetti, D., Bohlin, R. C., et al. 1996, *ApJ*, 467, 38. doi:10.1086/177583
- Kollatschny, W. & Zetzl, M. 2011, *Nature*, 470, 366. doi:10.1038/nature09761
- Kormendy, J. & Ho, L. C. 2013, *ARA&A*, 51, 511. doi:10.1146/annurev-astro-082708-101811
- Kormendy, J., Cornell, M. E., Block, D. L., et al. 2006, *ApJ*, 642, 765. doi:10.1086/501341
- Krist, J. E., Hook, R. N., & Stoehr, F. 2011, *Proc. SPIE*, 8127, 81270J. doi:10.1117/12.892762
- Kuhn, L., Shangquan, J., Davies, R., et al. 2024, *A&A*, 684, A52. doi:10.1051/0004-6361/202348138
- Li, Y.-R., Wang, J.-M., Ho, L. C., et al. 2013, *ApJ*, 779, 110. doi:10.1088/0004-637X/779/2/110
- Li, Y.-R., Songsheng, Y.-Y., Qiu, J., et al. 2018, *ApJ*, 869, 137. doi:10.3847/1538-4357/aee6b
- Li, S.-S., Yang, S., Yang, Z.-X., et al. 2021, *ApJ*, 920, 9. doi:10.3847/1538-4357/ac116e
- Li, Y.-R., Wang, J.-M., Songsheng, Y.-Y., et al. 2022, *ApJ*, 927, 58. doi:10.3847/1538-4357/ac4bcb
- Lu, K.-X., Du, P., Hu, C., et al. 2016, *ApJ*, 827, 118. doi:10.3847/0004-637X/827/2/118
- Lucas, R. A. & Ryon, J. E. 2022, *ACS Data Handbook v. 11.0*, 11
- Maiolino, R., Scholtz, J., Witstok, J., et al. 2024, *Nature*, 627, 59. doi:10.1038/s41586-024-07052-5
- Makidon, R. B., Lallo, M. D., Casertano, S., et al. 2006, *Proc. SPIE*, 6270, 62701L. doi:10.1117/12.671604
- Malik, U., Sharp, R., Penton, A., et al. 2023, *MNRAS*, 520, 2009. doi:10.1093/mnras/stad145
- Malkan, M. A., Gorjian, V., & Tam, R. 1998, *ApJS*, 117, 25. doi:10.1086/313110
- Marziani, P., Sulentic, J. W., Zwitter, T., et al. 2001, *ApJ*, 558, 553. doi:10.1086/322286
- Mathur, S., Fields, D., Peterson, B. M., et al. 2012, *ApJ*, 754, 146. doi:10.1088/0004-637X/754/2/146
- McConnell, N. J. & Ma, C.-P. 2013, *ApJ*, 764, 184. doi:10.1088/0004-637X/764/2/184
- Mejía-Restrepo, J. E., Lira, P., Netzer, H., et al. 2018, *Nature Astronomy*, 2, 63. doi:10.1038/s41550-017-0305-z
- Naim, A., Lahav, O., Buta, R. J., et al. 1995, *MNRAS*, 274, 1107. doi:10.1093/mnras/274.4.1107
- Onken, C. A., Ferrarese, L., Merritt, D., et al. 2004, *ApJ*, 615, 645. doi:10.1086/424655
- Orban de Xivry, G., Davies, R., Schartmann, M., et al. 2011, *MNRAS*, 417, 2721. doi:10.1111/j.1365-2966.2011.19439.x
- Osterbrock, D. E. & Ferland, G. J. 2006, *Astrophysics of gaseous nebulae and active galactic nuclei*, 2nd. ed. by D.E. Osterbrock and G.J. Ferland. Sausalito, CA: University Science Books, 2006
- Pacucci, F., Nguyen, B., Carniani, S., et al. 2023, *ApJL*, 957, L3. doi:10.3847/2041-8213/ad0158
- Pancoast, A., Brewer, B. J., & Treu, T. 2011, *ApJ*, 730, 139. doi:10.1088/0004-637X/730/2/139
- Pancoast, A., Brewer, B. J., Treu, T., et al. 2014, *MNRAS*, 445, 3073. doi:10.1093/mnras/stu1419
- Park, D., Kelly, B. C., Woo, J.-H., et al. 2012, *ApJS*, 203, 6. doi:10.1088/0067-0049/203/1/6
- Park, D., Barth, A. J., Ho, L. C., et al. 2022, *ApJS*, 258, 38. doi:10.3847/1538-4365/ac3f3e
- Pei, L., Fausnaugh, M. M., Barth, A. J., et al. 2017, *ApJ*, 837, 131. doi:10.3847/1538-4357/aa5eb1
- Peng, C. Y., Ho, L. C., Impey, C. D., et al. 2010, *AJ*, 139, 2097. doi:10.1088/0004-6256/139/6/2097
- Peterson, B. M., Ferrarese, L., Gilbert, K. M., et al. 2004, *ApJ*, 613, 682. doi:10.1086/423269
- Peterson, B. M., Grier, C. J., Horne, K., et al. 2014, *ApJ*, 795, 149. doi:10.1088/0004-637X/795/2/149
- Peterson, B. M. 1993, *PASP*, 105, 247. doi:10.1086/133140
- Petrosian, A., McLean, B., Allen, R., et al. 2008, *ApJS*, 175, 86. doi:10.1086/523105
- Planck Collaboration, Ade, P. A. R., Aghanim, N., et al. 2014, *A&A*, 571, A16. doi:10.1051/0004-6361/201321591
- Planck Collaboration, Aghanim, N., Akrami, Y., et al. 2020, *A&A*, 641, A6. doi:10.1051/0004-6361/201833910
- Press, W. H., Teukolsky, S. A., Vetterling, W. T., et al. 1992, *Cambridge: University Press*, —c1992, 2nd ed.
- Robinson, J. H., Bentz, M. C., Johnson, M. C., et al. 2019, *ApJ*, 880, 68. doi:10.3847/1538-4357/ab29f9
- Santos-Lleó, M., Chatzichristou, E., de Oliveira, C. M., et al. 1997, *ApJS*, 112, 271. doi:10.1086/313046
- Santos-Lleó, M., Clavel, J., Schulz, B., et al. 2001, *A&A*, 369, 57. doi:10.1051/0004-6361:20010103
- Schade, U., Bartl, F., Hofmann, K. P., et al. 2000, *Synchrotron Radiation Instrumentation: SRI99: Eleventh US National Conference*, 521, 51. doi:10.1063/1.1291758
- Schlegel, D. J., Finkbeiner, D. P., & Davis, M. 1998, *ApJ*, 500, 525. doi:10.1086/305772
- Shen, Y. & Ho, L. C. 2014, *Nature*, 513, 210. doi:10.1038/nature13712

- Shen, Y., Grier, C. J., Horne, K., et al. 2023, arXiv:2305.01014. doi:10.48550/arXiv.2305.01014
- Smith, E. P. & Heckman, T. M. 1989, ApJ, 341, 658. doi:10.1086/167524
- Tremaine, S., Gebhardt, K., Bender, R., et al. 2002, ApJ, 574, 740. doi:10.1086/341002
- van Dokkum, P. G. 2001, PASP, 113, 1420. doi:10.1086/323894
- Véron-Cetty, M.-P. & Véron, P. 2006, A&A, 455, 773. doi:10.1051/0004-6361:20065177
- Véron-Cetty, M.-P. & Véron, P. 2010, A&A, 518, A10. doi:10.1051/0004-6361/201014188
- Vika, M., Driver, S. P., Cameron, E., et al. 2012, MNRAS, 419, 2264. doi:10.1111/j.1365-2966.2011.19881.x
- Villafaña, L., Williams, P. R., Treu, T., et al. 2023, ApJ, 948, 95. doi:10.3847/1538-4357/accc84
- Virani, S. N., De Robertis, M. M., & VanDalsen, M. L. 2000, AJ, 120, 1739. doi:10.1086/301586
- Wang, J.-M., Du, P., Hu, C., et al. 2014, ApJ, 793, 108. doi:10.1088/0004-637X/793/2/108
- Wang, J.-M., Songsheng, Y.-Y., Li, Y.-R., et al. 2020, Nature Astronomy, 4, 517. doi:10.1038/s41550-019-0979-5
- Willett, K. W., Lintott, C. J., Bamford, S. P., et al. 2013, MNRAS, 435, 2835. doi:10.1093/mnras/stt1458
- Woo, J.-H., Schulze, A., Park, D., et al. 2013, ApJ, 772, 49. doi:10.1088/0004-637X/772/1/49
- Woo, J.-H., Yoon, Y., Park, S., et al. 2015, ApJ, 801, 38. doi:10.1088/0004-637X/801/1/38
- Yu, L.-M., Bian, W.-H., Wang, C., et al. 2019, MNRAS, 488, 1519. doi:10.1093/mnras/stz1766
- Yu, L.-M., Bian, W.-H., Zhang, X.-G., et al. 2020, ApJ, 901, 133. doi:10.3847/1538-4357/abb01e
- Yu, Z., Martini, P., Penton, A., et al. 2023, MNRAS, 522, 4132. doi:10.1093/mnras/stad1224
- Zhang, Z.-X., Du, P., Smith, P. S., et al. 2019, ApJ, 876, 49. doi:10.3847/1538-4357/ab1099